UNIVERSITÀ DEGLI STUDI DELL'AQUILA
DIPARTIMENTO DI SCIENZE FISICHE E CHIMICHE

Dottorato di Ricerca in Fisica

XXV ciclo

Analysis of the first data
of the GERDA experiment at LNGS

SSD: FIS/04

Dottorando: **Paolo Zavarise**

Coordinatore del corso: Prof. Michele Nardone

Relatore: Prof. Luigi Pilo

Co-relatore: Dott. Luciano Pandola

A.A.: 2011/2012

Contents

II ^{76}Ge experiments   37

3   Features of ^{76}Ge experiments   39

4   Design of the GERDA experiment   51

III   Digital Signal Processing   59

5   GERDA Digital Signal Processing   61

Introduction

The GERDA experiment is searching for Neutrinoless Double Beta Decay ($0\nu\beta\beta$) of ^{76}Ge. $0\nu\beta\beta$ is a process beyond the Standard Model of particle physics, and its observation implies that neutrinos are Majorana particles, which means that neutrino and antineutrino are the same thing.

The first goal of GERDA is a check of the Klapdor's claim: part of the Heidelberg-Moscow collaboration, led by Klapdor-Kleingrothaus, claimed observation of $0\nu\beta\beta$ decay of ^{76}Ge with an half-life of $(2.23^{+0.44}_{-0.31}) \times 10^{25}$ yr.

In this work I will describe what I have done in the GERDA collaboration during my PhD. This work is divided into four parts.

The Part I is a general introduction about $0\nu\beta\beta$. It contains two chapters. Chapter 1 describes the basics of Double Beta Decays, and the motivations to search for $0\nu\beta\beta$. Chapter 2 is a detailed analysis of the kinematics of Double Beta Decays, with a focus on phase space calculations.

The Part II is an introduction about the experiments designed to search for $0\nu\beta\beta$ of ^{76}Ge isotope. In Chapter 3, common features are presented. The most important is that they rely on Germanium detectors, enriched in the isotope of interest. For Double Beta Decays, the measured quantity is the sum of the kinetic energies of the emitted electrons. Thus, for $0\nu\beta\beta$, the expected signature is a peak at the Q-value of the decay ($Q_{\beta\beta} = 2039$ keV), because all the released energy is carried away by the two electrons. A review of the recent experiments is presented, with a focus on Heidelberg-Moscow. In Chapter 4, I will introduce the GERDA experiment. The key feature of GERDA is that Germanium detectors operate immersed in a Liquid Argon bath which is in a direct contact with them.

The Part III is about the Digital Signal Processing in GERDA. In Chapter 5 I will introduce our Digital Signal Processing software (GELATIO). I will describe our approach to the estimation of the signal parameters, with a special focus on the energy reconstruction. Chapter 6 is about an original approach which I have developed to reconstruct the impulse response function of the electronic chain from calibration data. Modelization of signal current, impulse response and FADC sampling is required. In Chapter 7, I have applied this analysis to the energy reconstruction and to the current reconstruction of the acquired signals. The obtained energy resolution and pulse shape discrimination perfor-

mances have been analyzed.

The Part IV is an analysis of the first scientific data acquired. Chapter 8 describes the database system, and its importance in the offline monitoring of the data. Chapter 9 is a description of the present status of the experiment. At the moment, a small energy window around $Q_{\beta\beta}$ is blinded: data are stored but not analyzed by the collaboration. The idea is to provide a background model before the opening of this window. One of the most controversial point in the Klapdor's work is the background model. So, I cannot provide in this work a check of the Klapdor's claim. Probably, GERDA will unblind all the data in the next months, and will present the results at the next TAUP conference, in 2013. Chapter 10 is about muons. GERDA is equipped by a muon veto system, to identify muon events which could induce a signal in the Germanium detectors. I have studied its efficiency, and estimated the background due to unidentified muon events which cause a signal in a single detector (so they are not cut by a multiplicity analysis) around $Q_{\beta\beta}$. In Chapter 11 I will focus on gamma rays. I have developed an algorithm to search for peaks in the energy spectrum, without any information in input: a fully blind approach. The GERDA concept seems good: only few photopeaks are clearly "visible". A comparation with the Heidelberg-Moscow gamma background is presented. The most intense line which appears in our energy spectrum arises from the β decay chain $^{42}\text{Ar} \rightarrow ^{42}\text{K} \rightarrow ^{42}\text{Ca}$ at 1524.7 keV. The observed intensity is higher than the prediction from the upper limits of the ^{42}Ar concentration in natural Argon in the previous literature. In Chapter 12 I will describe the most important result obtained by GERDA up to now: a new estimate of $2\nu\beta\beta$ half life of ^{76}Ge, which is compatible with the one from Heidelberg-Moscow. Both are a bit higher compared to the analysis of the data of the previous experiments. To obtain this result, a decomposition of the energy spectrum is needed.

Then, in the conclusions, I will summarize my results.

Part I

Neutrinoless Double Beta Decay

Chapter 1

Double Beta Decay

Introduction

The GERDA (GERmanium Detector Array) experiment is searching for the Neutrinoless Double Beta Decay ($0\nu\beta\beta$) of Germanium 76 at LNGS. In this chapter I will introduce the motivations, the physical problem and the possible consequences of the GERDA results.

1.1 Neutrino masses

One of the most important recent discoveries in particle physics is the observation of neutrino oscillations in solar, atmospheric, reactor and accelerator neutrino experiments. Neutrino oscillations prove that neutrinos have a non-zero rest mass. The Standard Model (SM) describes neutrinos as zero-mass particles, then it is fundamental to study how it is possible to extend the SM Lagrangian to implement neutrino masses in a natural way.

1.1.1 Dirac mass

Neutrino fields are described by the Dirac equation, because neutrinos are spin-1/2 particles. Considering, for simplicity, a single neutrino type, it is possible to write the Dirac Lagrangian [1]

$$\mathcal{L} = \overline{\psi}(i\gamma^{\mu}\partial_{\mu} - m_D)\psi$$

where ψ is a neutrino field, $\overline{\psi} = \psi^{\dagger}\gamma^0$ its adjoint, m_D is the Dirac mass of the particle. Thus the Dirac mass term is given by

$$\mathcal{L}_{\mathcal{M}} = -m_D\overline{\psi}\psi.$$

By using chirality projection operators

$$P_L = \frac{1}{2}\Big(1 - \gamma_5\Big) \qquad P_R = \frac{1}{2}\Big(1 + \gamma_5\Big)$$

and defining

$$\psi_L = P_L\psi \qquad \psi_R = P_R\psi$$

it is possible to write

$$\mathcal{L}_{\mathcal{M}} = -m_D(\overline{\psi}_L\psi_R + \overline{\psi}_R\psi_L).$$

Then, the Dirac mass originates from a coupling of a neutrino left-handed spinor and a neutrino right-handed spinor. According to the Standard Model, neutrinos are only left-handed. It means that either the Dirac mass is zero or there is a right-handed neutrino state, which is not covered within the SM that gives mass to the neutrino.

1.1.2   Majorana mass

It is possible to rewrite the Dirac Lagrangian using the two chiral components

$$\mathcal{L} = (\overline{\psi_L} + \overline{\psi_R})(i\slashed{\partial} - m_D)(\psi_L + \psi_R)$$

$$= \overline{\psi_L}(i\slashed{\partial}\psi_L - m_D\psi_R) + \overline{\psi_R}(i\slashed{\partial}\psi_R - m_D\psi_L).$$

Using Eulero-Lagrange equations it is possible to obtain two equations

$$i\slashed{\partial}\psi_L = m_D\psi_R$$

$$i\slashed{\partial}\psi_R = m_D\psi_L$$

which are coupled by the mass constant. If neutrinos were massless, the equations decouple, and the second equation becomes less important, because a right-handed neutrino has not been observed.

Majorana tried to describe massive neutrinos by using only a left-handed field. The idea is that the right-handed field should be a function of the left-handed field. From the second equation it is possible to obtain

$$i\slashed{\partial}C\overline{\psi_R}^T = m_D C\overline{\psi}_L^T.$$

This equation is identical to the starting one if we require (Majorana condition)

$$\psi_R = C\overline{\psi_L}^T = \psi_L^C.$$

Then, the Majorana field becomes

$$\psi = \psi_L + \psi_R = \psi_L + C\overline{\psi_L}^T = \psi_L + \psi_L^C.$$

The charge conjugate is

$$\psi^C = (\psi_L + \psi_L^C)^C = \psi_L^C + \psi_L = \psi.$$

Then a Majorana field is real! There is no difference between a Majorana neutrino and a Majorana anti-neutrino.

Now that we are able to describe the field as a function of only the left-handed (or right-handed) component, it is possible to add to the Lagrangian mass terms for left and right neutrino chiral states, and write the most general Lagrangian mass term as

$$\mathcal{L}_{\mathcal{M}} = -\frac{1}{2} \left(\overline{\psi_L^C} \; \overline{\psi_R} \right) M \begin{pmatrix} \psi_L \\ \psi_R^C \end{pmatrix} + h.c.$$

where the mass matrix M is

$$M = \begin{pmatrix} m_L & m_D \\ m_D & m_R \end{pmatrix}.$$

1.1.3   Seesaw mechanism

Now I will introduce a model which is able to explain why the left-handed neutrino is a so light particle. From the mass matrix, it is possible to obtain the mass eigenvalues

$$\det[M - mI] = 0 \implies m = \frac{1}{2}\left((m_L + m_R) \pm \sqrt{(m_L - m_R)^2 + 4m_D^2} \right).$$

Choosing $m_L = 0$ and $m_R >> m_D$ (type 1 Seesaw) it is possible to obtain

$$m_1 \simeq \frac{m_D^2}{m_R} \qquad m_2 \simeq m_R\left(1 + \frac{m_D^2}{m_R^2}\right) \simeq m_R.$$

It is possible to find the mass eigenstates

$$\psi_1 \sim (\psi_L + \psi_L^C) - \frac{m_D}{m_R^2}(\psi_R + \psi_R^C) \qquad \psi_2 \sim (\psi_R + \psi_R^C) - \frac{m_D}{m_R^2}(\psi_L + \psi_L^C).$$

That is, ψ_1 is mostly out familiar left-handed light Majorana neutrino, and ψ_2 is mostly the heavy sterile right-handed partner.

This is the famous Seesaw mechanism, and it provides an explanation for the question of why the neutrino has a mass so much smaller than the other charged leptons. The assumption $m_L = 0$ is natural, since a Majorana mass term for the left-handed chiral field ν_L brokes the symmetries and the renormalizability of the SM (it can, however, be generated by new physics beyond the SM) [1].

1.1.4   The mass scale

It is important to emphatize that neutrino oscillations do not provide information about the absolute mass scale. The Cosmic Microwave Background data of the WMAP experiment, combined with supernovae data and data on galaxy clustering, can be used to obtain an upper limit on the sum of neutrino masses. Depending on the model complexity and on the input data one obtains

$$\sum_i m_i \leq (0.3 - 1.3) \text{ eV}, \; 95\% \text{ C.L.}$$

If the Dirac mass of the neutrino is 1 MeV and the mass of the heavy partner is 10^{15} eV, it is possible to obtain from the Seesaw model a mass of the light neutrino in the meV range, which is compatible with the cosmological upper limit.

1.2   Neutrino oscillations

Neutrino oscillations is a quantum-mechanical consequence of the neutrino mixing relation

$$\nu_l[x] = \sum_j U_{ij} \nu_i[x].$$

Here $\nu_i[x]$ is a neutrino field with definite mass m_i, U is the unitary mixing matrix, $\nu_l[x]$ is a neutrino field with definite flavour. Note that I am using the notation of Mathematica [2]: round brackets only for algebra, squared bracket for functional dependences.

In the case of n neutrino flavours and n massive neutrinos, the $n \times n$ unitary neutrino mixing matrix U can be parametrized by $n(n-1)/2$ Euler angles and $n(n+1)/2$ phases. If massive neutrinos are Dirac particles, only $(n-1)(n-2)/2$ phases are physical and can be responsible for CP violation in the lepton sector. If massive neutrinos are Majorana fermions, the neutrino mixing matrix contains $n(n-1)/2$ CP violation phases.

1.2.1   The PMNS Mixing Matrix

All existing data on neutrino oscillations can be described by assuming 3-flavour neutrino mixing. Thus, the 3×3 unitary neutrino mixing matrix can be parametrized by 3 angles, and, depending on the neutrino nature, by 1 or 3 CP violation phases. It is named Pontecorvo-Maki-Nakagawa-Sakata (PMNS) matrix.

In the parametrization suggested by the Particle Data Group [3]

$$
U = \begin{bmatrix} 1 & 0 & 0 \\ 0 & c_{23} & s_{23} \\ 0 & -s_{23} & c_{23} \end{bmatrix} \begin{bmatrix} c_{13} & 0 & s_{13}e^{-i\delta} \\ 0 & 1 & 0 \\ -s_{13}e^{i\delta} & 0 & c_{13} \end{bmatrix} \begin{bmatrix} c_{12} & s_{12} & 0 \\ -s_{12} & c_{12} & 0 \\ 0 & 0 & 1 \end{bmatrix} \begin{bmatrix} 1 & 0 & 0 \\ 0 & e^{i\alpha_{21}/2} & 0 \\ 0 & 0 & e^{i\alpha_{31}/2} \end{bmatrix}
$$

$$
= \begin{bmatrix} c_{12}c_{13} & s_{12}c_{13} & s_{13}e^{-i\delta} \\ -s_{12}c_{23} - c_{12}s_{23}s_{13}e^{i\delta} & c_{12}c_{23} - s_{12}s_{23}s_{13}e^{i\delta} & s_{23}c_{13} \\ s_{12}s_{23} - c_{12}c_{23}s_{13}e^{i\delta} & -c_{12}s_{23} - s_{12}c_{23}s_{13}e^{i\delta} & c_{23}c_{13} \end{bmatrix} \begin{bmatrix} 1 & 0 & 0 \\ 0 & e^{i\alpha_{21}/2} & 0 \\ 0 & 0 & e^{i\alpha_{31}/2} \end{bmatrix}
$$

where $c_{ij} = \cos[\theta_{ij}]$, $s_{ij} = \sin[\theta_{ij}]$, the angle $\theta_{ij} = [0, \pi/2]$, $\delta = [0, 2\pi]$ is the Dirac CP violation phase and α_{21}, α_{31} are two Majorana CP violation phases.

1.2.2   The mass hierarchy

Neutrino oscillations depend on the differences of the squared masses of neutrino mass eigenstates. In the case of 3-neutrino mixing there are only two independent mass squared

differences. According to the Particle Data Group conventions, $|\Delta m^2_{21}|$ is the smallest one. It is related to the solar neutrino oscillations. By fixing $m_1 < m_2$, so that $\Delta m^2_{\odot} \equiv \Delta m^2_{21}$ is positive, there are two possible mass spectra: the so called normal spectrum (NS)

$$m_1 < m_2 < m_3$$

and the inverted spectrum (IS)

$$m_3 < m_1 < m_2.$$

The largest mass square difference ($\Delta m^2_A \equiv m^2_3 - m^2_1 > 0$ in the normal spectrum and $\Delta m^2_A \equiv m^2_3 - m^2_2 < 0$ in the inverted one) is related to atmospheric neutrino oscillations. The effect of $\Delta m^2_{\odot}$ on the atmospheric neutrino oscillations and of Δm^2_A on the solar neutrino oscillations is subdominant. Recent values are [3]

$$\Delta m^2_{\odot} = (7.58^{+0.22}_{-0.26}) \times 10^{-5} \text{ eV}^2$$

$$|\Delta m^2_A| = (2.35^{+0.12}_{-0.09}) \times 10^{-3} \text{ eV}^2.$$

1.3 Double Beta Decay

The neutrino mass nature (Dirac or Majorana), the type of neutrino hierarchy and the absolute scale of neutrino masses are open problems.
New information can be obtained by searching for the Neutrinoless Double Beta Decay. In a nuclear Double Beta Decay, two neutrons decay into two protons and two electrons as a single process. It is a second-order weak process.
According to the SM, this process is only possible with the emission of two anti-neutrinos, to preserve the lepton number

$$2n \rightarrow 2p + 2e^- + 2\overline{\nu}_e.$$

In this work, I have considered only the emission of β^- particles (electrons). A similar process is the double β^+ decay: two protons are converted into neutrons with the emission of two positrons. $\beta^-\beta^-$ candidates are different than $\beta^+\beta^+$ candidates. The GERDA experiment is studying $\beta^-\beta^-$ decay of ^{76}Ge, then, from now, I will focus only on this double beta mode.

1.3.1 Mass configuration of Double Beta Decay candidates

Whether a nucleus is stable or undergoes weak decay has to do with the dependence of the atomic mass M_A of the isotope (Z, A) on the nuclear charge Z (A is the mass
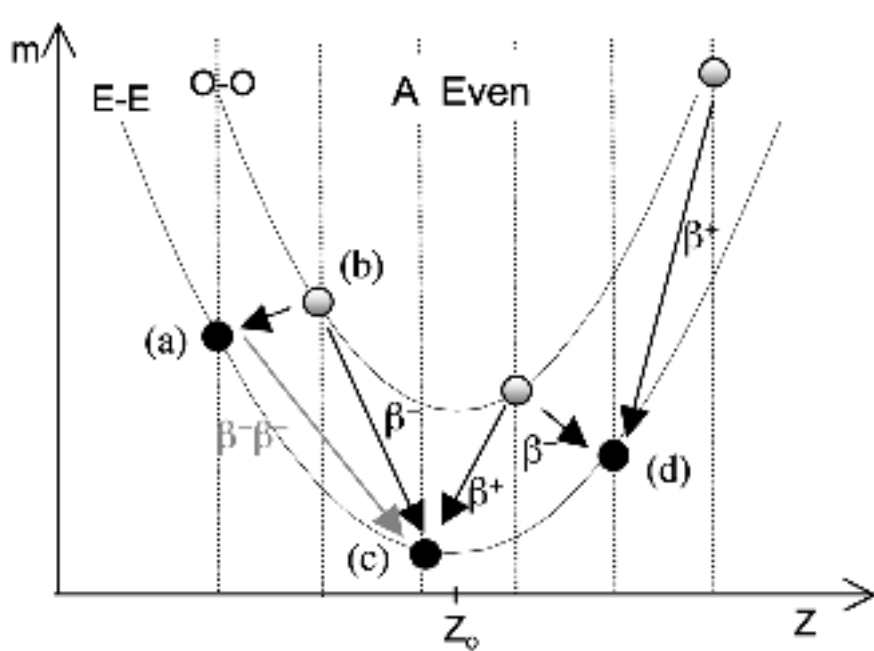
Figure 1.1: Ground state mass parabola for isobaric nuclei, showing the necessary configuration for double beta decay. Only the one (a) on the even-even (E-E) shell, whose β-decay is blocked (b) is allowed to do double beta decay (c). The shift of the parabola of the odd-odd (O-O) nuclei is due to the nuclear pairing energy.

number). The mass of an atomic nucleus is approximatively given by the semi-empirical mass-formula (Bethe-Weizsacker)

$$m = Zm_p + Nm_n - \frac{E_B}{c^2}$$

where m_p is the proton mass, m_n the neutron mass and E_B is the binding energy

$$E_B = a_V A - a_S A^{2/3} - a_C \frac{Z^2}{A^{1/3}} - a_A \frac{(A - 2Z)^2}{A} + a_P \frac{1}{A^{1/2}}.$$

The five terms are respectively the volume term, the surface term, the Coulomb term, the asymmetry term and the pairing term. According to Rohlf [4], good values for these parameters are $a_V = 15.75$ MeV, $a_S = 17.8$ MeV, $a_C = 0.711$ MeV, $a_A = 23.7$ MeV, $a_P = \pm 11.18$ MeV for odd N, odd Z or even N, even Z, respectively, while $a_P = 0$ for odd A. Thus, for odd A nuclei, typically only one isotope is stable; nuclei with charge Z smaller than the stable nucleus decay by electron emission, while those with larger Z decay by electron capture or positron emission or by both these modes simultaneously. For even A the situation is different. Due to the pairing term, the even-even nuclei form a parabola while the odd-odd nuclei form another one, at larger mass, as show in Fig. (1.1).

Consequently, in a typical case there exist two even-even nuclei for a given A which are stable against both electron and positron (or EC) decays. As these two nuclei usually do not have the same mass, the heavier may decay into the lighter through a second-order weak process in which the nuclear charge changes by two units: this is a Double Beta Decay.

Thus, it is convenient (but not necessary! [5]) to investigate Double Beta Decay between two even-even nuclei, in the cases when the single Beta Decay of the parent is forbidden. In nature, this configuration have been found 35 times. All ground states of even-even nuclei have spin and parity 0^+ and thus transitions $0^+ \to 0^+$ are expected in all cases. Occasionally, population of the low-lying excited states of the daughter nucleus is energetically possible, giving rise to $0^+ \to 2^+$ transitions.

The mass difference between the initial and the final nucleus minus two times the electron mass is the available kinetic energy for the particles (neglecting neutrino masses and the nuclear recoil), which is called $Q_{\beta\beta}$

$$Q_{\beta\beta} = E_I - E_F - 2m_e c^2.$$

1.3.2   Double Beta Decay modes

The Standard Model predicts the two-neutrinos Double Beta Decay ($2\nu\beta\beta$)

$$(Z, A) \to (Z + 2, A) + 2e^- + 2\overline{\nu_e}$$

which has been observed in a few isotopes. In Fig. 1.2, on the left, the Feynman diagram for the process is drawn.

```
Isotope |       Qbb |    T_{1/2}^{2vbb}
        |       keV |                 y
   48Ca |   4272.26 | (4.4+-0.6)*10^(19)
   76Ge |   2039.06 | (1.5+-0.1)*10^(21)
   82Se |   2995.12 | (9.2+-0.7)*10^(19)
   96Zr |   3350.37 | (2.3+-0.2)*10^(19)
  100Mo |   3034.40 | (7.1+-0.4)*10^(18)
  116Cd |   2813.50 | (2.8+-0.2)*10^(19)
  128Te |    865.87 | (1.9+-0.4)*10^(24)
  130Te |   2526.97 | (6.8+-1.2)*10^(20)
  136Xe |   2457.83 | (2.1+-0.2)*10^(21)
  150Nd |   3371.38 | (8.2+-0.9)*10^(18)
  238U  |   1144.98 | (2.0+-0.6)*10^(21)
```

Table 1.1: $2\nu\beta\beta$: observed decays, $Q_{\beta\beta}$ and half life [6].

Another kind of Double Beta Decay is the Neutrinoless Double Beta Decay

$$(Z, A) \to (Z + 2, A) + 2e^-.$$

$$2\nu\beta\beta \qquad\qquad\qquad\qquad 0\nu\beta\beta$$
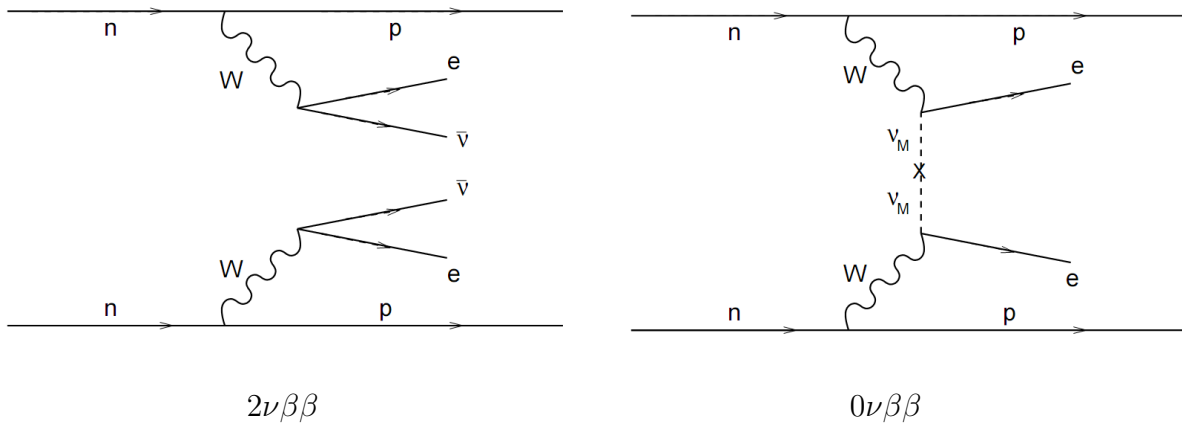
Figure 1.2: Double Beta Decays. On the left, Double Beta Decay with the emission of two antineutrinos. Lepton number is preserved. On the right, the Neutrinoless Double Beta Decay. Lepton number is not preserved.

This decay is not predicted by the Standard Model. In this decay there is a violation of the leptonic number by two units. There is only a claim for the observation of this decay, and it comes from part of the Heidelberg-Moscow collaboration [7]. The first goal of the GERDA experiment is to check this claim.

Other Double Beta Decay models have been proposed, e.g. with the emission of one or more Majorons (light bosons with coupling to neutrinos)

$$(Z, A) \rightarrow (Z + 2, A) + 2e^- + J \qquad\qquad 0\nu\beta\beta_J$$
$$(Z, A) \rightarrow (Z + 2, A) + 2e^- + 2J \qquad\qquad 0\nu\beta\beta_{JJ}.$$

The important point is that, independently on the mechanism, according to the Schechter-Valle theorem [8], a Double Beta Decay without emission of neutrinos implies that the neutrino is a Majorana particle. An intuitive way to focus this idea is to think $0\nu\beta\beta$ as a two-steps process (Racah sequence)

$$(Z, A) \rightarrow (Z + 1, A) + e^- + \overline{\nu}_e$$
$$= (Z + 1, A) + e^- + \nu_e$$
$$(Z + 1, A) + e^- + \nu_e \rightarrow (Z + 2, A) + 2e^-.$$

The first and the last lines are standard weak processes (lepton numbers are conserved), the central line is meaningful only if neutrino and the antineutrino are the same particle. In the full sequence, the family lepton number is violated by two units. In Fig. 1.2, on the right, the Feynman diagram for the simplest Neutrinoless Double Beta Decay model: the process is mediated by an exchange of a virtual Majorana neutrino.

1.3.3   Decay rates

As I will describe in the next chapter, approximations are possible to decouple the kinematic part (function of the output particle moments) from the nuclear part in the expressions for the $2\nu\beta\beta$ and $0\nu\beta\beta$ decay rates, and write

$$\frac{1}{T_{1/2}^{2\nu\beta\beta}} = G_{2\nu}|M_{2\nu}|^2$$

$$\frac{1}{T_{1/2}^{0\nu\beta\beta}} = G_{0\nu}|M_{0\nu}|^2 \Big(\frac{m_{\beta\beta}}{m_e}\Big)^2.$$

$T_{1/2}$ are the half lives of the processes, G the phase space volumes and M the nuclear matrix elements. In the expression of $T_{1/2}^{0\nu\beta\beta}$ a fundamental quantity appears, divided by the electron mass: the effective Majorana mass. It is a complex quantity defined by

$$m_{\beta\beta} = \sum_{k=1}^{3} U_{ek}^2 m_k$$

where U is the PMNS mixing matrix and m_k are the mass eigenvalues. Searching for the neutrinoless double beta decay is important to understand the neutrino nature, and to estimate the effective Majorana mass. The measured quantity is the half life of the decay. Phase spaces are computable (and I will compute them in the next chapter), nuclear matrix elements are a bit dependent on the nuclear model. Then it is possible to estimate the module of the effective Majorana mass.

1.4   Effective mass and neutrino hierarchy

To conclude, I will relate the effective Majorana mass to the parameters in the PMNS matrix. From the definition

$$|m_{\beta\beta}| = |m_1 U_{e1}^2 + m_2 U_{e2}^2 + m_3 U_{e3}^2| = |(m_1 c_{12}^2 + m_2 s_{12}^2 + e^{i\alpha_{21}})c_{13}^2 + m_3 s_{13}^2 e^{i(\alpha_{31}-2\delta)}|.$$

The three neutrino masses can be expressed in terms of the two measured Δm_{jk}^2 and, e.g., $\min[m_j]$. Thus, $|m_{\beta\beta}|$ is a function of the lightest neutrino mass, the Majorana and Dirac CP violation phases and of the type of the neutrino mass spectrum.
In the case of normal spectrum we have [3]

$$|m_{\beta\beta}| \simeq |\sqrt{\Delta m_{21}^2} s_{12}^2 c_{13}^2 + \sqrt{\Delta m_{31}^2} s_{13}^2 e^{i(\alpha_{31}-\alpha_{21}-2\delta)}|.$$

In the case of inverted spectrum

$$|m_{\beta\beta}| \simeq \sqrt{\Delta m_{23}^2 + m_3^2} \Big(1 - \sin^2[2\theta_{12}] \sin^2\Big[\frac{\alpha_{21}}{2}\Big]\Big)^{1/2}.$$
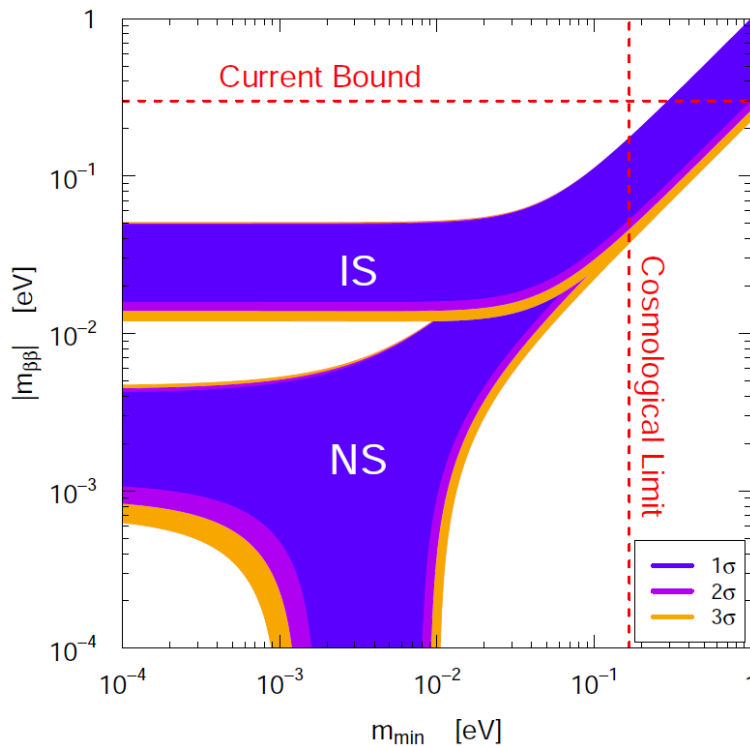
Figure 1.3: Value of the effective Majorana mass $|m_{\beta\beta}|$ as a function of the lightest neutrino mass in the normal (NS, with $m_{min} = m_1$) and inverted (IS, with $m_{min} = m_3$) neutrino mass spectra after the Daya Bay [9] measurement of θ_{13} [10] [11].

The predicted $0\nu\beta\beta$ effective Majorana mass as a function of the lightest neutrino mass is presented in Fig. 1.3 From the figure, it is clear that an "overlap" of both situations is possible: it is the "quasi degenerate" spectrum

$$m_1 \simeq m_2 \simeq m_3.$$

1.5   Summary

To summarize, the significance of studying $0\nu\beta\beta$ decay lies in the fact that it directly addresses the following questions related to physics beyond the Standard Model, namely

1. origin of neutrino mass (Dirac vs. Majorana)

2. absolute scale of neutrino mass

3. type of hierarchy

4. CP violation in the lepton sector.

The possibility of the existence of heavy neutrinos also gave rise to another intriguing idea called leptogenesis. The idea is that these very heavy neutrinos, which are Majorana particles, decayed as the universe cooled into lighter left-handed neutrinos or right-handed antineutrinos, along with Higgs bosons, which themselves decayed to quarks. If the probability of one of these heavy neutrinos to decay to a left-handed neutrino was slightly different than the probability to decay to a right-handed anti-neutrino, then there would be a greater probability to create quarks than anti-quarks. This could hense explain the fact that the Universe has an excess of matter with respect to anti-matter.

Bibliography

[1] Carlo Giunti and Chung W. Kim, *Fundamentals of Neutrino Physics and Astrophysics*, 2007.

[2] Wolfram Research, *Mathematica*, available at `http://www.wolfram.com/mathematica`.

[3] J. Beringer et al., *Review of Particle Physics (RPP)*, Phys.Rev. **D86** (2012), 010001.

[4] J.W. Rohlf, *Modern physics from alpha to Z0*, 1994.

[5] V.I. Tretyak, F.A. Danevich, S.S. Nagorny, and Yu.G. Zdesenko, *On the possibility to search for 2 β decay of initially unstable (α/β radioactive) nuclei*, Europhys.Lett. **69** (2005), 41-47, available at `arXiv:nucl-ex/0404016`.

[6] J. Kotila and F. Iachello, *Phase space factors for double-β decay*, Phys.Rev. **C85** (2012), 034316, available at `arXiv:1209.5722[nucl-th]`.

[7] H.V. Klapdor-Kleingrothaus and I.V. Krivosheina, *The evidence for the observation of $0\nu\beta\beta$ decay: The identification of $0\nu\beta\beta$ events from the full spectra*, Mod.Phys.Lett. **A21** (2006), 1547-1566.

[8] J. Schechter and J.W.F. Valle, *Neutrinoless Double beta Decay in $SU(2) \times U(1)$ Theories*, Phys.Rev. **D25** (1982), 2951.

[9] F.P. An et al., *Observation of electron-antineutrino disappearance at Daya Bay*, Phys.Rev.Lett. **108** (2012), 171803, available at `arXiv:1203.1669[hep-ex]`.

[10] S.M. Bilenky and Carlo Giunti, *Neutrinoless double-beta decay: A brief review*, Mod.Phys.Lett. **A27** (2012), 1230015, available at `arXiv:1203.5250[hep-ph]`.

[11] Alessandro Strumia and Francesco Vissani, *Neutrino masses and mixings and...* (2006), available at `arXiv:hep-ph/0606054`.

Chapter 2

Phase space calculations

Introduction

I am going to discuss $2\nu\beta\beta$ and $0\nu\beta\beta$ from a kinematics point of view. A discussion of the nuclear physics part (the matrix elements) is by far outside the scope of this work, and it is important especially in a second step of the analysis: after the possible measurement of $0\nu\beta\beta$ half life. Understanding the kinematics is very important in the context of Monte Carlo simulations. To simulate a decay, the event generator has to sample energy and momentum of the particles according to the appropriate distribution. Then, to understand the response of the detector, the decaying nucleus is placed in a GEANT4 [1] model of the experiment so that it is possible to simulate the interactions of the decay products with matter.

2.1 $2\nu\beta\beta$

I will start discussing the $2\nu\beta\beta$ decay. Fermi-type transition contributes only through mixing of high-lying 0^+ isobaric analogue states, so that it is generally very small; it is sufficient to retain Gamow-Teller matrix elements. The intermediate states are, therefore, limited to 1^+. The final state can be 0^+, 1^+, 2^+. The decay rate formula for 1^+ and 2^+ final states includes a factor $(K_N - L_N)^2$

$$K_N = \frac{\frac{1}{2}(E_I - E_F) + E_N - E_I}{\epsilon_1 + \epsilon_{\nu 1} + E_N - E_I} + \frac{\frac{1}{2}(E_I - E_F) + E_N - E_I}{\epsilon_2 + \epsilon_{\nu 2} + E_N - E_I} \tag{2.1}$$

$$L_N = \frac{\frac{1}{2}(E_I - E_F) + E_N - E_I}{\epsilon_1 + \epsilon_{\nu 2} + E_N - E_I} + \frac{\frac{1}{2}(E_I - E_F) + E_N - E_I}{\epsilon_2 + \epsilon_{\nu 1} + E_N - E_I} \tag{2.2}$$

(where E_I, E_F are the nuclear initial and final energy, E_N is the nuclear energy in a possible virtual intermediate state, ϵ_1, ϵ_2 are the electron energies, $\epsilon_{\nu 1}, \epsilon_{\nu_2}$ the neutrino energies) which strongly suppresses the process (typically $<< 1/100$), because in a first

approximation, as we will see later, $K_N \simeq L_N$ [12].

Then we can focus only to $0^+ \to 0^+$ transitions between ground states. Note that a transition to a 0^+ excited final states is possible, but, according to [2], its phase space is really small compared to a transition between ground states. Then, for the case that concerns us, the differential rate for $0_{gs}^+ \to 0_{gs}^+$ $2\nu\beta\beta$ decay is given by [2]

$$d\Gamma_{2\nu} = \sum_N (a_0 + a_1 \cos[\theta_{12}]) g_A^4 \frac{(G_W \cos[\theta_W])^4}{64\pi^7\hbar} \epsilon_{\nu1}^2 \epsilon_{\nu2}^2 (p_1 c)(p_2 c) \epsilon_1 \epsilon_2 d\epsilon_{\nu1} d\epsilon_1 d\epsilon_2 d(\cos[\theta_{12}])$$

$$\epsilon_{\nu2} = Q_{\beta\beta} + 2m_e c^2 - \epsilon_1 - \epsilon_2 - \epsilon_{\nu1}$$

$$G_W \equiv \frac{G_F}{(\hbar c)^3} = 1.166364 \times 10^{-5} \ \text{GeV}^{-2}$$

where p_1, p_2 are the electron momenta and θ_{12} the angle between the two emitted electrons. G_W is the Fermi coupling constant, θ_W is weak mixing angle, g_A is the axial-vector weak coupling constant.

The quantities a^0 and a^1 describe the intermediate state in the nuclear model. Clearly, one needs to sum over all the possible intermediate states. Integrating over θ_{12}, a_1 disappears and the result is

$$\Gamma_{2\nu} = \sum_N \int 2a_0 g_A^4 \frac{(G_W \cos[\theta_W])^4}{64\pi^7\hbar} \epsilon_{\nu1}^2 \epsilon_{\nu2}^2 (p_1 c)(p_2 c) \epsilon_1 \epsilon_2 d\epsilon_{\nu1} d\epsilon_1 d\epsilon_2$$

$$a_0 = \frac{1}{4} F[\epsilon_1, \epsilon_2] |M_{2\nu,N}^0|^2 \left((K_N + L_N)^2 + \frac{1}{3}(K_N - L_N)^2 \right)$$

$$= \frac{1}{3} F[\epsilon_1, \epsilon_2] |M_{2\nu,N}^0|^2 (K_N^2 + L_N^2 + K_N L_N).$$

$F[\epsilon_1, \epsilon_2]$ describes the Coulomb interaction of the escaping electrons with the nucleus, which I will discuss in the next section. $|M_{2\nu,N}^0|$ is the matrix element

$$|M_{2\nu,N}^0| = \ <0_F^+||\tau^+\vec{\sigma}||1_N^+> <1_N^+||\tau^+\vec{\sigma}||0_I^+>$$

where τ^+ is the isospin raising operator which changes a neutron to a proton and $\vec{\sigma}$ are the spin matrices to alter the total angular momentum. Putting all together

$$\Gamma_{2\nu} = \sum_N \int F[\epsilon_1, \epsilon_2] g_A^4 |M_{2\nu,N}^0|^2 (m_e c^2)^2 \frac{K_N^2 + L_N^2 + K_N L_N}{12} \times$$

$$\times \frac{4}{15} \frac{(G_W \cos[\theta_W])^4 (m_e c^2)^9}{64\pi^7\hbar} 30 \frac{\epsilon_{\nu1}^2 \epsilon_{\nu2}^2 d\epsilon_1 (p_1 c)(p_2 c) \epsilon_1 \epsilon_2 d\epsilon_{\nu1} d\epsilon_2}{(m_e c^2)^{11}}$$

where I have rearranged the numerical coefficients in a convenient way. Thus the expression for the half life of the process is

$$\left(T_{1/2}^{2\nu\beta\beta} \right)^{-1} = \sum_N \int F[\epsilon_1, \epsilon_2] g_A^4 |M_{2\nu,N}^0|^2 (m_e c^2)^2 \frac{K_N^2 + L_N^2 + K_N L_N}{12} \times$$

$$\times \frac{4}{15} \frac{(G_W \cos[\theta_W])^4 (m_e c^2)^9}{64\pi^7\hbar \ln[2]} 30 \frac{\epsilon_{\nu1}^2 \epsilon_{\nu2}^2 d\epsilon_{\nu1} (p_1 c)(p_2 c) \epsilon_1 \epsilon_2 d\epsilon_1 d\epsilon_2}{(m_e c^2)^{11}}. \tag{2.3}$$

It is important to note that in the last equation the nuclear part is not decoupled by the kinematic part. Additional approximations are needed to do that, and I will describe the solutions proposed by Suhonen [3] and by Iachello [2].

2.1.1   The Coulomb correction

The phase space is affected by the Coulomb attraction which the positive nucleus puts on the electrons. The net effect is to alter the energy distribution of the electrons. The standard way to approach the problem is to include into the phase factor integrals the Fermi correction function [4]. For a single electron which is escaping the nucleus

$$F[\epsilon] = \frac{2(1+S)}{(\Gamma[2S+1])^2}\left(2\frac{p\rho}{\hbar}\right)^{2S-2}\exp[\pi\eta]|\Gamma[S+i\eta]|^2 \qquad (2.4)$$

where the coefficients S and η are defined as

$$S = \sqrt{1-\alpha^2 Z_f^2} \qquad \eta = \frac{\epsilon}{pc}\alpha Z_f = \frac{c}{v}\alpha Z_f \qquad \rho = 1.2 \cdot A^{1/3} \cdot 10^{-15} \text{ m}$$

ρ is the nuclear radius, (Z_i, Z_f) are the atomic number of the (initial, final) nucleus $Z_f = Z_i + 2$, ϵ and p are the total energy and the momentum of the electron.

The Fermi correction function is a function of energy only, then the global correction is a product of the contributions of each electron. The number of free electrons is two then

$$F[\epsilon_1, \epsilon_2] = F[\epsilon_1]F[\epsilon_2].$$

For small nuclei $\alpha Z_f << 1$ then $S \simeq 1$ and (2.4) can be approximated as

$$F[\epsilon] \simeq \frac{4}{(\Gamma[2S+1])^2}\left(2\frac{p\rho}{\hbar}\right)^{2S-2}\exp[\pi\eta]|\Gamma[S+i\eta]|^2. \qquad (2.5)$$

Note that the energy dependence is not changed. This expression is quoted in [3].

There is a wide set of approximations for the Fermi correction function, because to compute the complex Γ is not a really trivial task. Now, dedicated algorithms exist, e.g. the complex Lanczos method described in [5] and implemented in [6].

For $S \simeq 1$ it is possible to going further. According to Mott and Massey [7] [8]:

$$F[\epsilon] \simeq \frac{2\pi\eta}{1-\exp[-2\pi\eta]}.$$

With this multiplying factor the electron distribution is found to be proportional to p rather than to p^2 for energies in the range $2\pi\eta \gg 1$ [8].

From the previous expression it is easy to obtain a non-relativistic approximation for $S \simeq 1$: when $\eta \to \infty$, which means $p \to 0$, it is possible to write

$$F[\epsilon] \simeq 2\pi\eta \propto \frac{\epsilon}{p}. \qquad (2.6)$$

This expression (Primakoff-Rosen approximation) allows to solve a few integrals in an analytical way. Despite these approximations could be useful, there is not a deep reason to use them in a numerical computation. In the event generator of choice in the GERDA collaboration (Decay0 [9]), the expression for the Fermi function is the most accurate (2.4).

2.1.2   Nuclear and kinematics decoupling

Now I will discuss how it is possible to decouple the nuclear physics part (nuclear matrix element) from the kinematic part (phase factor) in the expression (2.3). I will discuss two approaches, the approach of Suhonen [3] and the approach of Iachello [2].

In the first approach, the coefficients K_N and L_N are constant. It is clear that $\epsilon_1 + \epsilon_{\nu_1} + \epsilon_2 + \epsilon_{\nu_2} = E_I - E_F$, then, in an average sense

$$\epsilon_1 + \epsilon_{\nu_1} \simeq \epsilon_2 + \epsilon_{\nu_2} \simeq \frac{1}{2}(E_I - E_F) \implies K_N \simeq 2$$

$$\epsilon_1 + \epsilon_{\nu_2} \simeq \epsilon_2 + \epsilon_{\nu_1} \simeq \frac{1}{2}(E_I - E_F) \implies L_N \simeq 2$$

Now it is possible to integrate over the free neutrino energy to obtain

$$\left(T_{1/2}^{2\nu\beta\beta}\right)^{-1} = \int \sum_N F[\epsilon_1, \epsilon_2] g_A^4 |M_{2\nu,N}^0|^2 \frac{(G_W \cos[\theta_W])^4 (m_e c^2)^9}{240\pi^7 \hbar \ln[2]} \frac{(Q_{\beta\beta} + 2m_e c^2 - \epsilon_1 - \epsilon_2)^5 (p_1 c)(p_2 c)\epsilon_1 \epsilon_2 d\epsilon_1 d\epsilon_2}{(m_e c^2)^{11}}$$

Defining

$$G_{2\nu}^0 \equiv \int F[\epsilon_1, \epsilon_2] \frac{(Q_{\beta\beta} + 2m_e c^2 - e_1 - e_2)^5 (p_1 c)(p_2 c)\epsilon_1 \epsilon_2 d\epsilon_1 d\epsilon_2}{(m_e c^2)^{11}} \tag{2.7}$$

$$G_{2\nu}^S \equiv \frac{(G_W \cos[\theta_W])^4 (m_e c^2)^9}{240\pi^7 \hbar \ln[2]} G_{2\nu}^0 = \frac{3.8 \times 10^{-24}}{\text{yr}} G_{2\nu}^0 \tag{2.8}$$

$$|M_{2\nu}|^2 \equiv \sum_N g_A^4 |(m_e c^2) M_{2\nu,N}^0|^2 \tag{2.9}$$

it is possible to write

$$\left(T_{1/2}^{2\nu\beta\beta}\right)^{-1} = G_{2\nu}^S |M_{2\nu}|^2$$

where nuclear physics and kinematics are decoupled.

The second approach relies on a "closure approximation". The idea is to average the energy of the intermediate state

$$E_N \to < E_N >$$

in the expressions of K_N (2.1) and L_N (2.2). In this approximation these coefficients are not dependent on a specific nuclear intermediate state $K_N \simeq K, L_N \simeq L$, but preserve the dependence on the energy of the particles. Thus

$$G_{2\nu}^I = \int F[\epsilon_1, \epsilon_2] \frac{K_N^2 + L_N^2 + K_N L_N}{12} \frac{4}{15} \frac{(G_W \cos[\theta_W])^4 (m_e c^2)^9}{64\pi^7 \hbar \ln[2]} 30 \frac{\epsilon_{\nu1}^2 \epsilon_{\nu2}^2 d\epsilon_{\nu1}(p_1 c)(p_2 c)\epsilon_1 \epsilon_2 d\epsilon_1 d\epsilon_2}{(m_e c^2)^{11}}$$

$$= \frac{2}{3\ln[2]} \int F[\epsilon_1, \epsilon_2](K_N^2 + L_N^2 + K_N L_N) \frac{(G_W \cos[\theta_W])^4 (m_e c^2)^9}{64\pi^7 \hbar} \frac{\epsilon_{\nu1}^2 \epsilon_{\nu2}^2 d\epsilon_{\nu1}(p_1 c)(p_2 c)\epsilon_1 \epsilon_2 d\epsilon_1 d\epsilon_2}{(m_e c^2)^{11}}$$

$$= \frac{(G_W \cos[\theta_W])^4 (m_e c^2)^9}{240\pi^7 \hbar \ln[2]} \int F[\epsilon_1, \epsilon_2] \frac{K_N^2 + L_N^2 + K_N L_N}{12} 30 \frac{\epsilon_{\nu1}^2 \epsilon_{\nu2}^2 d\epsilon_{\nu1}(p_1 c)(p_2 c)\epsilon_1 \epsilon_2 d\epsilon_1 d\epsilon_2}{(m_e c^2)^{11}}.$$

The second important difference between the two approaches stays in the Coulomb correction. In the first approach, $F[\epsilon_1, \epsilon_2] = F[\epsilon_1]F[\epsilon_2]$ with the expression (2.5) for the Fermi correction function. In the second approach a more refined analysis has been done, which keeps into account of the interaction between the two electrons, then the global correction cannot be factorized.

2.1.3   Events generation

For an event generator, it is important only the energy-momentum dependence in the phase space density. A multiplicative factor dependent only on (Z, A) is not important. Then, from the point of view of the event generator, in the case of $2\nu\beta\beta$ decay

$$p[\epsilon_1, \epsilon_2] \propto F[\epsilon_1]p_1\epsilon_1 F[\epsilon_2]p_2\epsilon_2(Q_{\beta\beta} + 2m_e c^2 - \epsilon_1 - \epsilon_2)^5 \qquad (2.10)$$

$$F[\epsilon] \propto p^{2S-2} \exp[\pi\eta]|\Gamma[S + i\eta]|^2$$

is enough. A non obvious point is: what is the best way to sample ϵ_1, ϵ_2 from the above probability distribution? In the Decay0 approach, it is a two steps process. In the first one, ϵ_1 is sampled from

$$p[\epsilon_1] = \int p[\epsilon_1, \epsilon_2]d\epsilon_2 \propto \int F[\epsilon_1]p_1\epsilon_1 F[\epsilon_2]p_2\epsilon_2(Q_{\beta\beta} + 2m_e c^2 - \epsilon_1 - \epsilon_2)^5 d\epsilon_2.$$

In the second one, ϵ_2 is sampled from

$$p[\epsilon_2|\epsilon_1] = \frac{p[\epsilon_1, \epsilon_2]}{p[\epsilon_1]} \propto F[\epsilon_2]p_2\epsilon_2(Q_{\beta\beta} + 2m_e c^2 - \epsilon_1 - \epsilon_2)^5.$$

The point is that there is not an analytical expression for $p[\epsilon_1]$, then it is necessary to construct a binned version of it, to avoid an evaluation of the integral at each sampling. On the contrary, $p[\epsilon_2]$ is given. If binning is not very fine, it is possible to note a very small difference in the generated distribution of ϵ_1 compared to the generated distribution of ϵ_2.

Despite an higher memory usage, I prefer to compute a two-dimensional fine binned version of $p[\epsilon_1, \epsilon_2]$ (2.10) in the first step, and then extract simultaneously ϵ_1 and ϵ_2 by choosing a bin according to the two-dimensional probability density.

2.1.4   Phase space calculation results

To understand if the expressions in the event generator are correct, I have implemented them in a new software that is not only able to sample $p[\epsilon_1, \epsilon_2]$ in the way that I have suggested, but also realizes a full phase space calculation, to compare a single numerical value with the present literature.

To do that, it is clear that a multiplicative factor dependent only on (Z, A) is also important (and it is important to pay attention to the different definitions of the phase space integral).

I was able to reproduce the result in [3] and [10] in a perfect way. In my work, I used updated values for $Q_{\beta\beta}$ of many nuclei, taken from the Nuclear Data Center in the Brookhaven laboratories `http://www.nndc.bnl.gov/`. Major differences compared to previous calculation are visible in ^{136}Xe (my $Q_{\beta\beta}$ value is 2458 keV while in [3] is 2478 keV) and ^{128}Te, ^{130}Te. Note that a difference of few keV is clearly visible, because there is a contribution of $Q_{\beta\beta}^{11}$ in the $2\nu\beta\beta$ phase factor. When the $Q_{\beta\beta}$ estimate was nearly stable in time (e.g. ^{76}Ge, ^{150}Nd just to quote two examples with a very different mass number) there is a perfect compatibility of the results (Tab. 2.1). According to Iachello [2], the standard way to manage the Coulomb correction overestimates the phase space volumes.

```
Isotope | G_{2vbb}
        |  My-best | Iachello |  My-appr |  Suhonen |   Boehm
   48Ca | 1.59e-17 | 1.55e-17 | 1.61e-17 | 1.62e-17 | 1.60e-17
   76Ge | 5.11e-20 | 4.82e-20 | 5.28e-20 | 5.26e-20 | 5.28e-20
   82Se | 1.70e-18 | 1.60e-18 | 1.76e-18 | 1.74e-18 | 1.76e-18
   96Zr | 7.41e-18 | 6.82e-18 | 7.78e-18 | 7.28e-18 | 7.79e-18
  100Mo | 3.62e-18 | 3.31e-18 | 3.82e-18 | 3.60e-18 | 3.82e-18
  116Cd | 3.09e-18 | 2.76e-18 | 3.31e-18 | 2.99e-18 | 3.24e-18
  128Te | 3.05e-22 | 2.69e-22 | 3.31e-22 | 3.44e-22 | 3.43e-22
  130Te | 1.74e-18 | 1.53e-18 | 1.89e-18 | 1.94e-18 | 1.94e-18
  136Xe | 1.64e-18 | 1.43e-18 | 1.79e-18 | 1.98e-18 | 1.95e-18
  150Nd | 4.31e-17 | 3.64e-17 | 4.82e-17 | 4.85e-17 | 4.81e-17
  238U  | 2.16e-19 | 1.46e-20 | 2.90e-19 |          |
```

Table 2.1: $2\nu\beta\beta$ results of my phase space calculation compared to the published results in [2], [3], [10]. In "My-best" I have used the expression (2.4) for the Fermi correction function, while in "My-appr" I have used the expression (2.5). To obtain the values in the paper of Suhonen, multiply by g_A^4. To obtain the values in the book of Boehm, multiply by g_A^4, then take the inverse.

2.1.5   Effective nuclear matrix element

From the phase space volume and the experimental half life, it is interesting to estimate the "effective" nuclear matrix element (i.e. experimental $|M_{2\nu}|$ value extracted from the
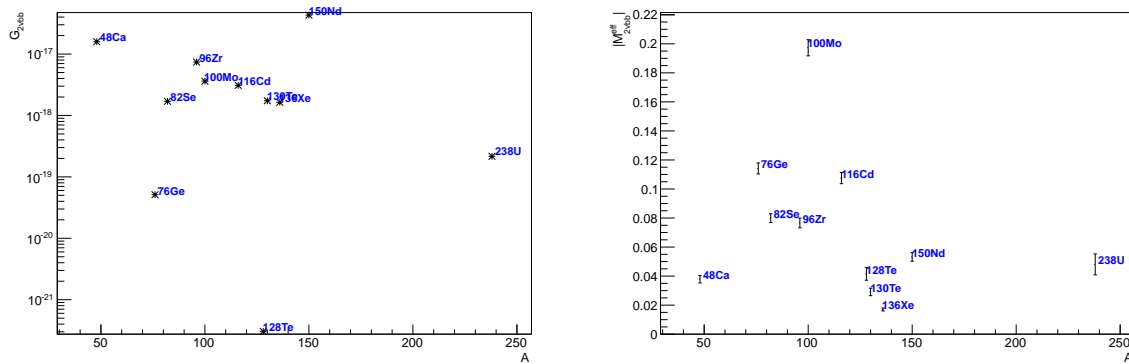
Figure 2.1: $2\nu\beta\beta$: on the left: the phase space volume; on the right: effective nuclear matrix element.

measured $T_{1/2}^{2\nu\beta\beta}$ and calculated phase space factor). In principle, all the nuclear models / algorithms to estimate the nuclear matrix elements, should provide these results in the $2\nu\beta\beta$ case. You can see my results in Tab. 2.2, and a visual plot in Fig. 2.1. Note that despite the different approximations in the phase space volume, concerning the nuclear matrix elements the results are very similar.

```
Isotope |    |M_{2vbb}|
        |       My-best |      Iachello
   48Ca | 0.038+-0.003 | 0.038+-0.003
   76Ge | 0.114+-0.004 | 0.118+-0.004
   82Se | 0.080+-0.003 | 0.083+-0.003
   96Zr | 0.077+-0.003 | 0.080+-0.003
  100Mo | 0.197+-0.006 | 0.206+-0.006
  116Cd | 0.108+-0.004 | 0.114+-0.004
  128Te | 0.042+-0.004 | 0.044+-0.005
  130Te | 0.029+-0.003 | 0.031+-0.003
  136Xe | 0.017+-0.001 | 0.018+-0.001
  150Nd | 0.053+-0.003 | 0.058+-0.003
  238U  | 0.048+-0.007 | 0.185+-0.028
```

Table 2.2: $2\nu\beta\beta$: results of my effective nuclear matrix element estimates compared to the published results in [2].

2.1.6   Kinetic energy distributions of the electrons

In many experiments, including GERDA, the measured quantity in a double beta decay is the sum of the kinetic energy of the electrons. Then, it is important to study this distribution. In the Primakoff-Rosen approximation of the Fermi correction function, it is possible to arrange the phase space integral to obtain an analytical expression.

Starting from (2.8), we can write

$$G = \int \frac{F[\epsilon_1]p_1\epsilon_1 F[\epsilon_2]p_2\epsilon_2(Q_{\beta\beta} + 2m_ec^2 - \epsilon_1 - \epsilon_2)^5 d\epsilon_1 d\epsilon_2}{(m_ec^2)^{11}}.$$

In the Primakoff-Rosen approximation (2.6)

$$G \propto \int \frac{\epsilon_1^2\epsilon_2^2(Q_{\beta\beta} + 2m_ec^2 - \epsilon_1 - \epsilon_2)^5 d\epsilon_1 d\epsilon_2}{(m_ec^2)^{11}}.$$

We can work in units of m_ec^2 and write

$$G \propto \int \epsilon_1^2\epsilon_2^2(Q_{\beta\beta} + 2 - \epsilon_1 - \epsilon_2)^5 d\epsilon_1 d\epsilon_2.$$

Moving to the kinetic energies

$$e_{k1} = \epsilon_1 - 1 \qquad e_{k2} = \epsilon_2 - 1$$

we can write

$$G \propto \int (e_{k1} + 1)^2(e_{k2} + 1)^2(Q_{\beta\beta} - e_{k1} - e_{k2})^5 de_{k1} de_{k2}. \qquad (2.11)$$

Single electron spectrum

By integrating the previous expression (2.11) in $0 < e_{k2} < Q_{\beta\beta} - e_{k1}$ it is possible to obtain the single electron spectrum

$$\frac{dG}{de_{k1}} \propto (e_{k1} + 1)^2(Q_{\beta\beta} - e_{k1})^6\Big((Q_{\beta\beta} - e_{k1})^2 + 8(Q_{\beta\beta} - e_{k1}) + 28\Big)$$

in perfect agreement with Boehm [10].

Sum electron spectrum

Changing the variables in the expression (2.11)

$$e_{ksum} = e_{k1} + e_{k2} \qquad e_{kdiff} = e_{k1} - e_{k2}$$

so that

$$e_{k1} = \frac{1}{2}(e_{ksum} + e_{kdiff}) \qquad e_{k2} = \frac{1}{2}(e_{ksum} - e_{kdiff})$$

to obtain

$$G \propto \int \left(\frac{1}{2}(e_{ksum} + e_{kdiff}) + 1\right)^2 \left(\frac{1}{2}(e_{ksum} - e_{kdiff}) + 1\right)^2 (Q_{\beta\beta} - e_{ksum})^5 de_{ksum} de_{kdiff}.$$

By integrating the previous expresion in $0 < e_{kdiff} < e_{ksum}$ it is possible to obtain the sum electrum spectrum

$$G \propto \int e_{ksum}(Q_{\beta\beta} - e_{ksum})^5 \Big(e_{ksum}^4 + 10e_{ksum}^3 + 40e_{ksum}^2 + 60e_{ksum} + 30\Big) de_{ksum}. \qquad (2.12)$$

Note that, doing the integral

$$G \propto \left(Q_{\beta\beta}^{11} + 22Q_{\beta\beta}^{10} + 220Q_{\beta\beta}^9 + 990Q_{\beta\beta}^8 + 1980Q_{\beta\beta}^7 \right)$$

the final distribution is

$$\frac{dG}{de_{ksum}} \propto e_{ksum}(Q_{\beta\beta} - e_{ksum})^5 \left(e_{ksum}^4 + 10e_{ksum}^3 + 40e_{ksum}^2 + 60e_{ksum} + 30 \right) \qquad (2.13)$$

again, in perfect agreement with Boehm [10]. Note that, in this approximation, the shape of the distribution is independent by A and Z!

Sum electron spectrum results

I have fitted the precise sum of electron kinetic energies distribution for ^{76}Ge $2\nu\beta\beta$ decay using a parametrization of a form similar to the non relativistic version (2.13)

$$\frac{dG'}{de_{ksum}} \propto e_{ksum}(Q_{\beta\beta} - e_{ksum})^5 (e_{ksum}^4 + c_3 e_{ksum}^3 + c_2 e_{ksum}^2 + c_1 e_{ksum} + c_0).$$

It is a 4-parameter formula. I have done a maximum likelihood binned fit, using 16384 bins for axis (total memory usage: 2 Gb) and simulating 10^9 events. In Tab. 2.3, my coefficients compared to the non-relativistic approximation. In Fig. 2.2, on the left, it is possible to find the plot of the original distribution (in blue) and of my fit (in green). Both the non-relativistic (NR) approximation and my fit locate the maximum at 672.3 keV.

```
         NR |  This work
c3 =     10 |     7.731 +- 2.090
c2 =     40 |    38.305 +- 5.602
c1 =     60 |    47.511 +- 8.417
c0 =     30 |    21.145 +- 3.302
```

Table 2.3: ^{76}Ge $2\nu\beta\beta$: sum electron spectrum. Best fit using a 4-parameters model. $Q_{\beta\beta}$ and e_{ksum} are adimensional, in units of $m_e c^2$. Errors from the fit algorithm.
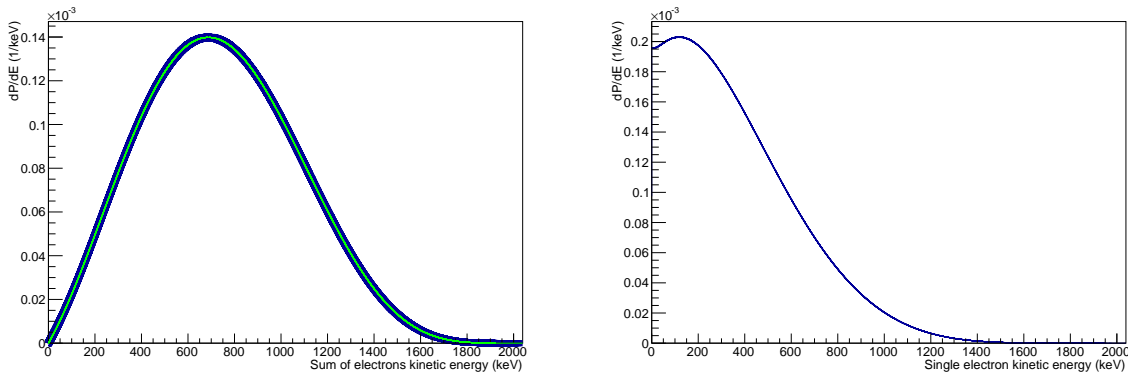
Figure 2.2: ^{76}Ge $2\nu\beta\beta$: on the left, sum of the kinetic energies of the electrons (in blue: Monte Carlo simulations, the marker has been enlarged; in green: best fit); on the right: kinetic energy distribution for a single electron.

2.2 $0\nu\beta\beta$

The most important point to discuss is the relation between the $0\nu\beta\beta$ and the neutrino nature. It is possible to show [11] that the virtual neutrino propagator is proportional to the effective mass of the electron neutrino, which is a complex scalar quantity defined by

$$m_{\beta\beta} \equiv \sum_{k=1}^{3} U_{ek}^2 m_k$$

where U is the PMNS mixing matrix and m_k are the mass eigenvalues. The propagator enters in the amplitude, then the decay rate is proportional to $|m_{\beta\beta}^2|$. The key idea is that, by studing this process, it is possible to measure its half life, which is related to the matrix element, and then it is possible to estimate $|m_{\beta\beta}|$.

Concerning kinematics, it is clearly more simple compared to the $2\nu\beta\beta$ case. That is because there are only two decay products: the two electrons. Moreover, a closure approximation is commonly used to evaluate the matrix element. For $0\nu\beta\beta$ decay this is supposed to be a good approximation because the neutrino energy in the virtual state is much greater than the typical energy of the relevant nuclear levels [12]. Thus, the differential rate for the $0_{gs}^+ \to 0_{gs}^+$ $0\nu\beta\beta$ decay is given by [2]

$$d\Gamma_{0\nu} = (a_0 + a_1 \cos[\theta_{12}]) g_A^4 \frac{(G_W \cos[\theta_W])^4 (m_e c^2)^9}{16\pi^5 \hbar} \frac{(p_1 c)(p_2 c)\epsilon_1 \epsilon_2 d\epsilon_1}{(m_e c^2)^5} d(\cos[\theta_{12}])$$

where

$$\epsilon_2 = Q_{\beta\beta} + 2m_e c^2 - \epsilon_1.$$

Then the integral rate is

$$\Gamma_{0\nu} = \int 2a_0 g_A^4 2 \frac{(G_W \cos[\theta_W])^4 (m_e c^2)^9}{32\pi^5 \hbar} \frac{(p_1 c)(p_2 c)\epsilon_1 \epsilon_2 d\epsilon_1}{(m_e c^2)^5}$$

$$a_0 = F[e_1, e_2] \left| \frac{m_{\beta\beta}}{m_e} \right|^2 \frac{|M^0_{0\nu}|^2}{(m_e c^2)^2}.$$

An expression of the nuclear matrix element is given in [12].

Merging everything

$$\Gamma_{0\nu} = \int 2F[e_1, e_2] \left| \frac{m_{\beta\beta}}{m_e} \right|^2 g_A^4 \frac{|M^0_{0\nu}|^2}{(m_e c^2)^2} \left(\frac{m_e c R}{\hbar} \right)^2 \left(\frac{\hbar}{m_e c R} \right)^2 \times$$
$$\times 2 \frac{(G_W \cos[\theta_W])^4 (m_e c^2)^9}{32\pi^5 \hbar} \frac{(p_1 c)(p_2 c)\epsilon_1 \epsilon_2 d\epsilon_1}{(m_e c^2)^5}.$$

Defining

$$G^0_{0\nu} = \int F[e_1, e_2] \frac{(p_1 c)(p_2 c)\epsilon_1 \epsilon_2 d\epsilon_1}{(m_e c^2)^5}$$
$$G_{0\nu} = \left(\frac{\hbar}{m_e c R} \right)^2 \frac{(G_W \cos[\theta_W])^4 (m_e c^2)^9}{32\pi^5 \hbar \ln[2]} G^0_{0\nu} = \left(\frac{\hbar}{m_e c R} \right)^2 \frac{2.8 \times 10^{-22}}{\text{yr}} G^0_{0\nu}$$
$$|M_{0\nu}|^2 = 4 g_A^4 \frac{|M^0_{0\nu}|^2}{(m_e c^2)^2} \left(\frac{m_e c R}{\hbar} \right)^2$$

it is possible to write for the half life

$$\left(T^{0\nu\beta\beta}_{1/2} \right)^{-1} = G_{0\nu} \left| \frac{m_{\beta\beta}}{m_e} \right|^2 |M_{0\nu}|^2.$$

2.2.1   Phase space calculation results

As I have done for the $2\nu\beta\beta$ decay, I use my software for the estimation of the phase space volume (Fig. 2.3), and I have compared my results with [2], [3], [10] (Tab. 2.4). Results agree in a perfect way. Note that the differences due to a different value of $Q_{\beta\beta}$ are minor, due to the fact that $2\nu\beta\beta$ is sensitive to $Q^{11}_{\beta\beta}$, while $0\nu\beta\beta$ only to $Q^5_{\beta\beta}$. The effect of the improved correction in the Iachello approach is more visible for $0\nu\beta\beta$ than for $2\nu\beta\beta$, e.g.

$$\frac{G_{2\nu\beta\beta,my}}{G_{2\nu\beta\beta,I}}[150Nd] = 1.184 \qquad \frac{G_{0\nu\beta\beta,my}}{G_{0\nu\beta\beta,I}}[150Nd] = 1.254.$$
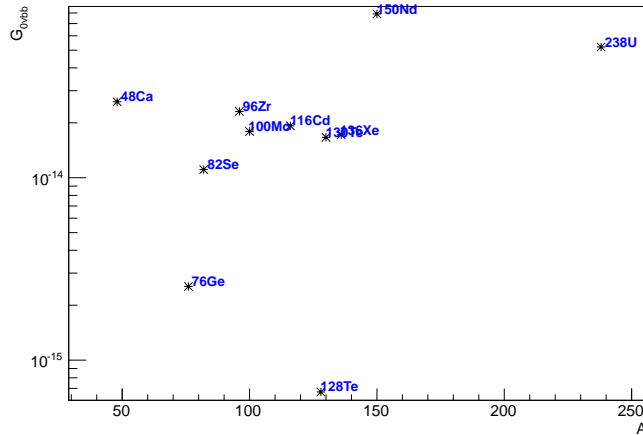
Figure 2.3: $0\nu\beta\beta$: the phase space volume.

```
        | My-best | Iachello | Suhonen |  My-appr |   Boehm
  48Ca  | 2.61e-14 | 2.48e-14 | 2.60e-14 | 2.64e-14 | 2.58e-14
  76Ge  | 2.53e-15 | 2.36e-15 | 2.55e-15 | 2.62e-15 | 2.58e-15
  82Se  | 1.11e-14 | 1.02e-14 | 1.10e-14 | 1.15e-14 | 1.14e-14
  96Zr  | 2.31e-14 | 2.06e-14 | 2.31e-14 | 2.42e-14 | 2.37e-14
 100Mo  | 1.79e-14 | 1.59e-14 | 1.85e-14 | 1.89e-14 | 1.85e-14
 116Cd  | 1.93e-14 | 1.67e-14 | 1.89e-14 | 2.07e-14 | 2.00e-14
 128Te  | 6.69e-16 | 5.88e-16 | 6.71e-16 | 7.27e-16 | 7.38e-16
 130Te  | 1.66e-14 | 1.42e-14 | 1.67e-14 | 1.81e-14 | 1.79e-14
 136Xe  | 1.72e-14 | 1.46e-14 | 1.77e-14 | 1.88e-14 | 1.91e-14
 150Nd  | 7.90e-14 | 6.30e-14 | 7.85e-14 | 8.83e-14 | 8.45e-14
 238U   | 5.21e-14 | 3.36e-14 |          | 6.98e-14 |
```

Table 2.4: $0\nu\beta\beta$: results of my phase space calculation compared to the published results in [2], [3], [10]. In "My-best" I have used the expression (2.4) for the Fermi correction function, while in "My-appr" I have used the expression (2.5). To obtain the values in the paper of Suhonen, multiply by g_A^4. To obtain the values in the book of Boehm, multiply by g_A^4, then take the inverse. It seems that Suhonen used the expression (2.5) for the Fermi Correction function to evaluate $2\nu\beta\beta$ phase spaces and the expression (2.4) in the $0\nu\beta\beta$ case.

2.2.2   Single electron spectrum

In the same way as I did for $2\nu\beta\beta$, it is possible to obtain the energy spectrum for a single electron

$$G_{0\nu} \propto \int F[\epsilon_1]p_1\epsilon_1 F[\epsilon_2]p_2\epsilon_2 d\epsilon_1.$$
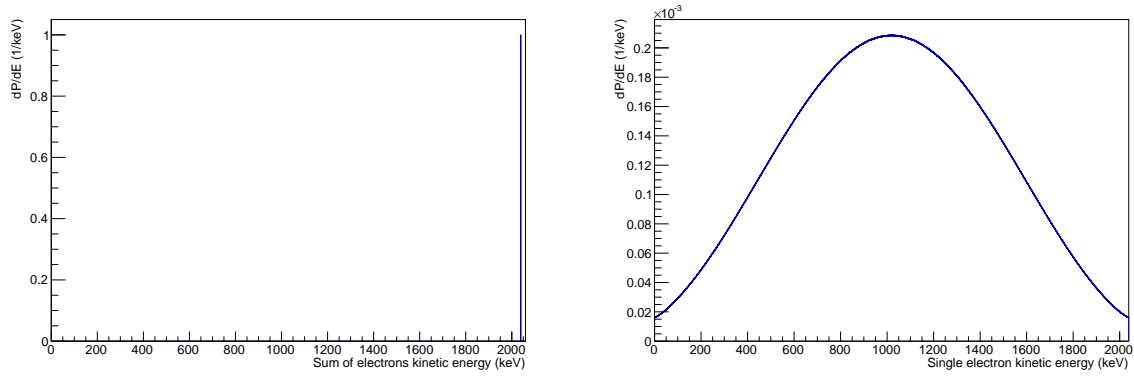
Figure 2.4: ^{76}Ge $0\nu\beta\beta$: on the left, sum of the kinetic energies of the electrons, which is equal to $Q_{\beta\beta}$; on the right: kinetic energy distribution for a single electron.

In the Primakoff-Rosen approximation

$$G_{0\nu} \propto \int \epsilon_1^2 \epsilon_2^2 d\epsilon_1.$$

Moving to normalized units and kinetic energies

$$G_{0\nu} \propto \int (e_{1k} + 1)^2 (e_{2k} + 1)^2 de_{1k}$$

$$\propto \int (e_{1k} + 1)^2 (Q_{\beta\beta} - e_{1k} + 1)^2 de_{1k}.$$

Note that, doing the integral [12]

$$G_{0\nu} \propto \left(Q_{\beta\beta}^5 + 10Q_{\beta\beta}^4 + 40Q_{\beta\beta}^3 + 60Q_{\beta\beta}^2 + 30Q_{\beta\beta} \right).$$

For the single electron spectrum I have obtained [10]

$$\frac{dG_{0\nu}}{de_{1k}} = (e_{1k} + 1)^2 (Q_{\beta\beta} - e_{1k} + 1)^2.$$

A plot of this distribution is presented in Fig. 2.4.

2.2.3   Sum electron spectrum

In the $0\nu\beta\beta$ only two electrons are emitted. Then, because of the energy conservation

$$e_{k1} + e_{k2} = Q_{\beta\beta}.$$

This is the key signature of the $0\nu\beta\beta$. If the detector is able to measure the energy of the electrons, the signature of $0\nu\beta\beta$ is very peculiar: a peak at the expected $Q_{\beta\beta}$ energy.

2.3   Summary

A study of the nuclear phase factors involved in $2\nu\beta\beta$ and $0\nu\beta\beta$ decays have been done. My results are in agreement with [2] [3] [10].

Bibliography

[1]   John Allison et al., *Geant4 developments and applications*, IEEE Trans.Nucl.Sci. **53** (2006), 270.

[2]   J. Kotila and F. Iachello, *Phase space factors for double-β decay*, Phys.Rev. **C85** (2012), 034316, available at `arXiv:1209.5722[nucl-th]`.

[3]   J. Suhonen and O. Civitarese, *Weak-interaction and nuclear-structure aspects of nuclear double beta decay*, Phys.Rept. **300** (1998), 123-214.

[4]   E. Fermi, *Trends to a Theory of beta Radiation. (In Italian)*, Nuovo Cim. **11** (1934), 1-19.

[5]   W.H. Press, S.A. Teukolsky, W.T. Vetterling, and B.P. Flannery, *Numerical Recipes: the Art of Scientific Computing*, 3rd, 2007.

[6]   M. Galassi, *GNU Scientific Library Reference Manual*, 3rd, 2009.

[7]   N.F. Mott and H.S.W. Massey, *The theory of Atomic Collisions*, 1933.

[8]   P. Venkataramaiah, K. Gopala, A. Basavaraju, S.S. Suryanarayana, and H. Sanjeeviah, *A simple relation for the Fermi function* (1984).

[9]   O.A. Ponkratenko, V.I. Tretyak, and Yu.G. Zdesenko, *The Event generator DECAY4 for simulation of double beta processes and decay of radioactive nuclei*, Phys.Atom.Nucl. **63** (2000), 1282-1287, available at `arXiv:nucl-ex/0104018`.

[10] F. Boehm and P. Vogel, *Physics of massive neutrinos*, 1992.

[11] Carlo Giunti and Chung W. Kim, *Fundamentals of Neutrino Physics and Astrophysics*, 2007.

[12] M. Fukugita and T. Yanagida, *Physics of neutrinos and applications to astrophysics*, 2003.

Part II

^{76}Ge experiments

Chapter 3

Features of ^{76}Ge experiments

Introduction

In this chapter I will discuss the experiments to the search for the Neutrinoless Double Beta Decay of ^{76}Ge. They present common features. The most important is that they rely on the technology of Germanium semiconductor detectors, thus an introduction about the physics of these objects is needed. Then a quick summary of the recent previous experiments, with a special focus to the claim for the observation by a part of the Heidelberg-Moscow collaboration.

3.1 Physics of Germanium detectors

Germanium detectors are semiconductor diodes having a p-i-n structure. A p-i-n diode is a diode with a wide, lightly doped "near" intrinsic semiconductor region between heavily doped p-type and n-type semiconductor regions. Under the action of an appropriate reverse bias voltage, free (mobile) charges in the conduction band are drifted to the electrodes. A part of the detector is said to be "depleted" when all mobile charges are swept out from it, thus leaving a net electric charge from the valence band.

When a particle interacts with the material within the depleted volume of a detector, charge carriers (holes and electrons) are produced and are swept by the electric field to the p^+ and n^+ electrodes. During the motion of the carriers, a charge is induced at the contacts. This charge, which is proportional to the energy deposited in the detector by the interacting particle, is converted into a voltage signal by a charge sensitive preamplifier. The size of the depleted region is proportional to the high voltage applied, then it is important to be sure that the detector is fully depleted to have optimal charge collection performances.

Because germanium has relatively low band gap (2.96 eV at 77 K, Tab. 3.1), these

detectors must be cooled in order to reduce the thermal generation of charge carriers (thus reverse leakage current) to an acceptable level. Otherwise, the leakage current could worse the energy resolution of the detectors.

Electron mobility	$3.6 \times 10^4 \ \frac{\text{cm}^2}{\text{V} \cdot \text{s}}$
Hole mobility	$4.2 \times 10^4 \ \frac{\text{cm}^2}{\text{V} \cdot \text{s}}$
Energy per electron-hole pair	2.96 eV
Fano factor	0.12

Table 3.1: Germanium properties at 77 K.

3.1.1 Particles interactions

Interaction of electrons and positrons

Electrons can lose kinetic energy by collisional effects (ionization and excitation) and bremsstrahlung. Collisional effects are described by the Bethe formula

$$-\frac{dE}{dx} = \frac{4\pi}{m_e c^2} \frac{nz^2}{\beta^2} \left(\frac{e^2}{4\pi\epsilon_0}\right)^2 \ln\left[\frac{2m_e c^2 \beta^2}{I(1-\beta^2)} - \beta^2\right] \tag{3.1}$$

where v is the velocity of the particle, $\beta = v/c$, z is the charge of the particle, x is the distance travelled by the particle, n is the electron density of the material, I is the mean excitation potential. Collisional losses are the dominant mechanism for energies below 10 MeV, as shown in Fig. 3.1.
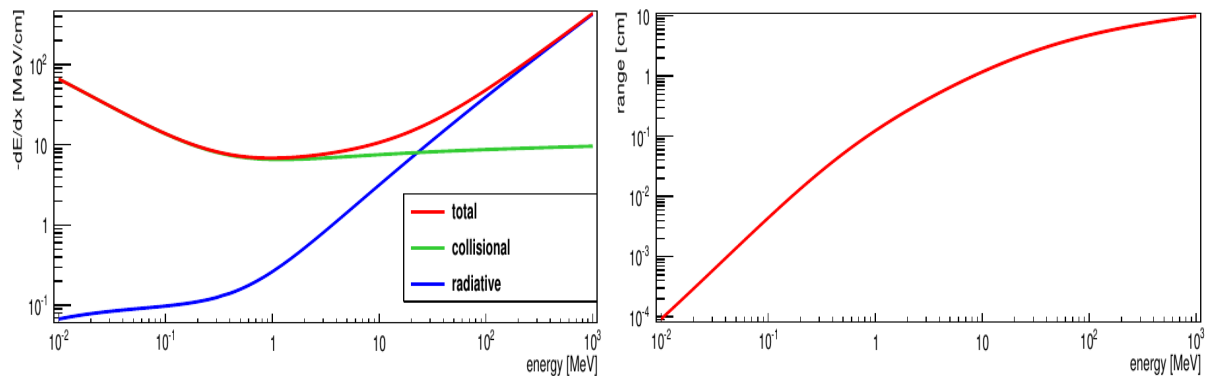
Figure 3.1: Electrons in germanium: on the left the contribution of different mechanism to the energy loss, as a function of the electron kinetic energy; on the right: the range as a function of the kinetic energy. Data from [1].

Interaction of gamma rays

When a gamma ray enters the detector, there are three interaction mechanisms which are dominant: photoelectric absorption, Compton scattering and pair production.

The photoelectric absorbtion is an interaction in which the incident gamma-ray disappears. In its place, a photoelectron is produced from one of the electron shells of the absorber atom with a kinetic energy given by the incident photon energy $h\nu$ minus the binding energy of the electron in its original shell E_b. Then the electron energy is

$$E_{e^-} = h\nu - E_b.$$

The result of a Compton scattering interaction is the creation of a recoil electron and scattered gamma-ray photon, with the splitting of energy between the two. In the approximation that electrons are initially unbound and at rest, the energy of the scattered gamma ray is

$$h\nu' = \frac{h\nu}{1 + (h\nu/m_e c^2)(1 - \cos[\theta])}$$

and then the kinetic energy of the electron is

$$E_{e^-} = h\nu - h\nu' = h\nu\Big(\frac{(h\nu/(m_e c^2))(1 - \cos[\theta])}{(1 + ((h\nu/(m_e c^2))(1 - \cos[\theta])))}\Big).$$

It is interesting to study the two limiting cases

$$\theta \simeq 0 \to E_{e^-} \simeq 0$$

$$\theta \simeq \pi \to E_{e^-} \simeq h\nu\Big(\frac{2h\nu/(m_e c^2)}{(1 + 2h\nu/(m_e c^2))}\Big).$$

Thus, the electron energy has a maximum below $h\nu$.

The last mechanism is the pair production. The process occurs in the intense electric field near the nuclei and corresponds to the creation of an electron-positron pair at the point of complete disappearance of the incident gamma-ray. Because an energy of $2m_e c^2$ is required to create the electron-positron pair, a minimum gamma-ray energy of 1.02 MeV is required to make the process energetically possible. If the incident gamma-ray energy exceeds this value, the excess energy appears in the form of kinetic energy shared by the electron-positron pair.

After a few millimeters, the positron annihilates with an electron of the medium, and the process releases two 511 keV photons, which may escape the detector. Thus, for a given photon energy, the energy response of the detector could present the so-called single and double escape peaks, as it is possible to see in Fig. 3.2.

The contribution to the total cross section of the different mechanisms for different gamma energies is shown in Fig. 3.3.

$$h\nu \gg 2m_0 c^2$$
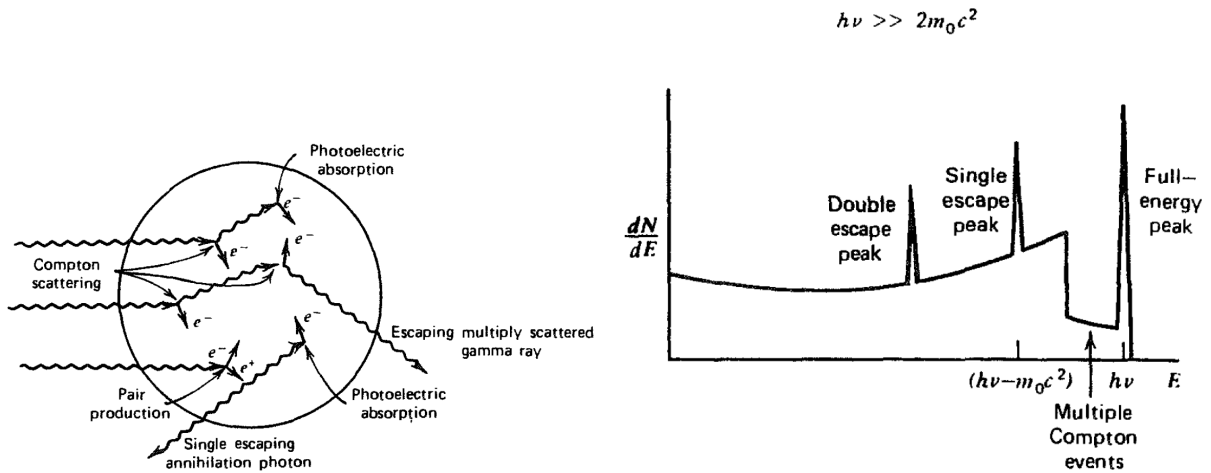
Figure 3.2: On the left: example of gamma ray interactions in the detector. On the right: detector response spectrum for a gamma ray of fixed energy [2].
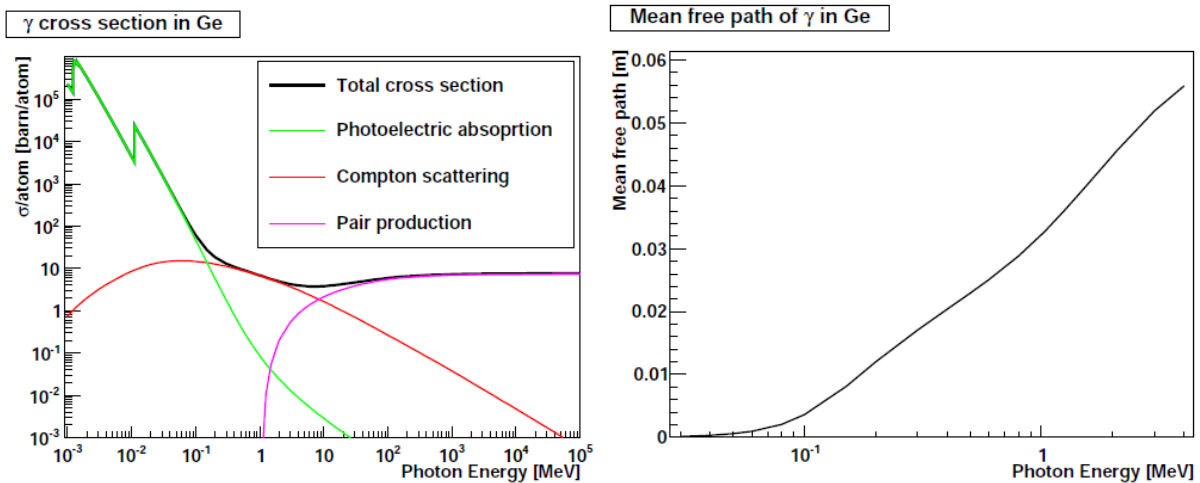
Figure 3.3: Gamma in Germanium: on the left the contribution of different mechanism to the total cross section, as a function of the gamma energy; on the right: the mean free path as a function of the energy. The mean free path is given by $l = \frac{1}{\sigma n}$ where σ is the effective cross sectional area for a nucleus and n is the number density per unit volume. Data from [3].

Interaction of alpha particles

An α particle is a nucleus of Helium $^4\text{He}^{2+}$ which consists of two neutrons and two protons. Heavy charged particles lose energy in an adsorber according to the Bethe formula (3.1). The range of α particles in Germanium is very short, of the order of millimeters, as shown in Fig. 3.4.
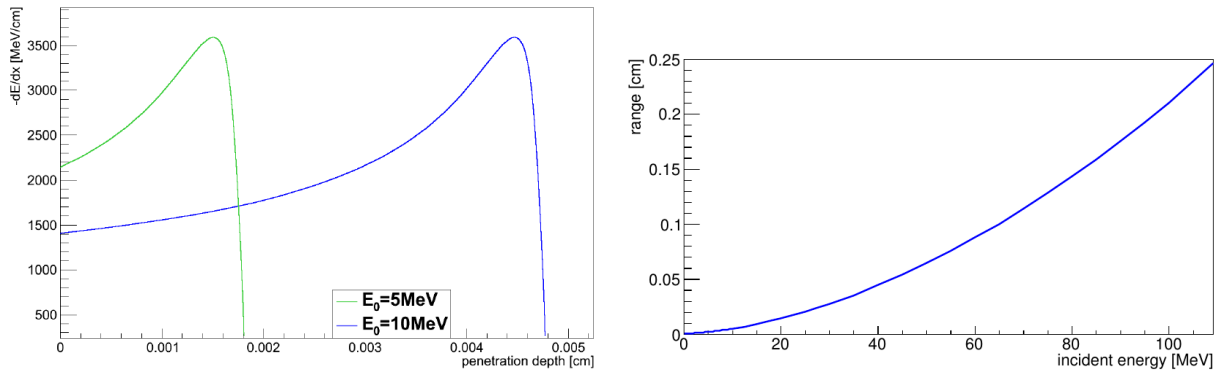
Figure 3.4: On the left: specific energy loss of an α particle with an incident energy of 5 and 10 MeV versus the penetration depth in Ge. This special shape of energy loss in an adsorber is called Bragg curve. On the right: range of an α particle versus incident energy in Ge. It is clear that α penetrations are surface events. Data from [1].

3.1.2 Pulse shape discrimination

A fundamental topic in this kind of experiments, is to understand if a signal in the $Q_{\beta\beta}$ window is produced by a neutrinoless double beta decay or if it is a background.

The basic filter is to check if there is a simultaneous signal coming from another detector or from the muon veto. In this case, the event is likely not a neutrinoless double beta decay. This is called anticoincidence cut.

For energies of the order of 1 MeV, both the electron and positron travel a few millimeters at most before losing all their kinetic energy to the absorbing medium. A double beta decay is then a single site event, because the two electrons lose the kinetic energy in a very small region compared to the dimensions of the detectors. A gamma ray instead may travel centimeters without interacting, and in an interaction it could release only part of its energy, then it could interact many times in distant points of the detector. Thus, a gamma ray could generate a multi-site event. According to Monte Carlo simulation, when a gamma ray between 1 and 3 MeV is fully absorbed, the event is probably multi-site, as it is possible to see in Fig. 3.5.

The signal shapes of single and multi-site events are quite different, and it is important, but quite complex, to find methods to distinguish between the two cases.

3.1.3 Dead layer

To a first approximation, the active volume of a germanium detector is simply the region between the n^+ and p^+ contacts. However, these contacts may have appreciable thickness and can represent a dead layer on the surface of the crystal. The surface dead layer on germanium detectors may vary slowly over periods of time because of the formation of
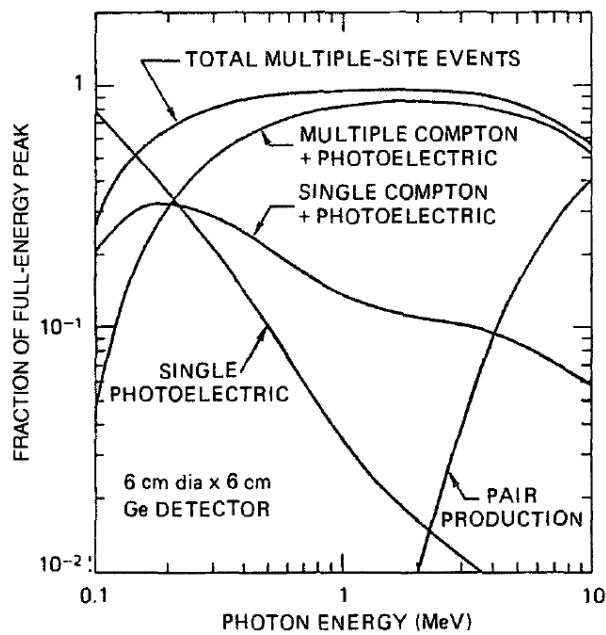
Figure 3.5: Fractions of the full-energy peak contributed by different energy loss mechanisms in a 6 cm x 6 cm coaxial HPGe detector, as predicted by Monte Carlo simulations [4]. The simulated detector has a size comparable to ANG1 (which is 5.85 cm x 6.8 cm). The other coaxial detectors which operate in GERDA are bigger, then it is reasonable to expect an higher fraction of multi-site events.

so-called surface channel in which the electric field and charge collection efficiency are reduced. The dead layer could reach a depth of many millimeters. Then it is important to have a precise estimate of the dead volume: the measured energy for a neutrinoless double beta decay in that volume is expected to be lower than $Q_{\beta\beta}$ because of incomplete charge collection.

3.2 ^{76}Ge experiments

The idea of ^{76}Ge experiments is quite simple: to build Germanium detectors of material enriched in the isotope of interest. Then, place the detectors in a ultralow-background environment and... wait!

The enrichment is needed. ^{76}Ge abundance in natural germanium is only 7.8%. It is more convenient to create enriched detectors instead of having many natural detectors, because most backgrounds scale proportionally to the total mass.

Semiconductor detectors work well especially as calorimeters, in the sense that they offer a superior energy resolution. Moreover, in this kind of experiments, the source is equal to the detector, then there is a coverage of the full solid angle, and a very good detection

efficiency.

The main drawback is that, compared to other kind of Neutrinoless Double Beta Decay experiment, a study of the event topology, which can be done only by a pulse shape analysis, is on the contrary quite complex. Moreover, the $Q_{\beta\beta}$ value is lower compared to other isotopes, and is lower than the energy of many gamma lines typical of natural radioactivity. Then, there is a contribution of the Compton background for all these lines in the region of interest.

3.2.1 Statistics

The number of signal and background counts are Poisson distributed.

The expected number of signal counts is given by

$$\overline{N}_{signal,obs} = M\frac{N_A}{A} \cdot a \cdot e\frac{\ln[2]}{T_{1/2}}t \tag{3.2}$$

where M is the total mass, t is the time of measurements, a is the mass fraction of the $0\nu\beta\beta$ isotope, e is the efficiency, $T_{1/2}$ is the $0\nu\beta\beta$ half file, N_A is the Avogadro constant and A is the molar weight of the isotope of interest. The expected number of background counts is given by

$$\overline{N}_{bkg,obs} = MtB\Delta E$$

where ΔE is the resolution at $Q_{\beta\beta}$ and B is the background index in the signal energy window around $Q_{\beta\beta}$.

It is possible to obtain analytical expressions for the experimental sensitivity in the two limiting case: zero background and very high background counts.

In the first case, from the first equation, the sensitivity is defined as the needed time to obtain one count

$$1 = M\frac{N_A}{A} \cdot a \cdot e\frac{\ln[2]}{T_{1/2}}t \implies T_{1/2} = M\frac{N_A}{A} \cdot a \cdot e\ln[2]t.$$

If the number of background counts is high, it is possible to approximate the Poisson statistics with a Gaussian statistics. The sensitivity limit is set by the following equation

$$n_\sigma\sqrt{MtB\Delta E} = M\frac{N_A}{A} \cdot a \cdot e\frac{\ln[2]}{T_{1/2}}t$$

where n_σ is the deviation from the mean in units of σ.

Then to fix the ideas

$$T_{1/2}[n_\sigma C.L] = \frac{\ln[2]}{n_\sigma}\frac{N_A}{A}a \cdot e\sqrt{\frac{Mt}{B \cdot \Delta E}}$$

e.g., to have a 90% confidence level $n_\sigma = 1.64$.

To summarize, in the zero background count limit, the sensitivity is proportional to the exposure Mt. In the high background count limit, the sensitivity is proportional to $(Mt)^{1/2}$. For an improved analysis, a numerical approach is needed.

3.3   Recent previous ^{76}Ge experiments

3.3.1   The Heidelberg-Moscow experiment

The only claim of observation of $0\nu\beta\beta$ comes from a part of the Heidelberg-Moscow (HdM) collaboration. H.V. Klapdor-Kleingrothaus, after an advanced pulse shape analysis, estimated the ^{76}Ge half life as [5]

$$T_{1/2}^{0\nu\beta\beta} = (2.23^{+0.44}_{-0.31}) \times 10^{25} \text{ yr.}$$

The HdM experiment runs since 1990 to 2003 at Laboratori Nazionali del Gran Sasso, LNGS, Italy. Five HPGe detector were used, namely ANG1, ANG2, ANG3, ANG4, ANG5, in total 10.96 kg enriched in ^{76}Ge at ~ 86 %. The total exposure collected is 71.7 kg·yr, but only the period between November 1995 and March 2003 has been considered in the final analysis, which corresponds to an exposure of 56.66 kg·yr. The background index was (Fig. 3.6)

$$B_{HM} = (0.113 \pm 0.007) \ \frac{\text{counts}}{\text{keV} \cdot \text{kg} \cdot \text{yr}}.$$

Klapdor's results depend strongly on pulse shape discrimination. Two approaches have been used.

The first one is a neuronal-network, which means that pulse shape cuts have been tuned learning from the data, especially trying to preserve the ^{208}Tl double escape peak at 1592 keV, which, according to Monte Carlo simulations, is an enriched sample of single-site events. Note that ANG1 (the smallest detector) has been dropped from this analysis, thus the total exposure has been reduced to 51.39 kg·yr. The pulse-shape selected spectrum and the full one are in Fig. 3.7.

The second approach is a comparison of the physical pulses against a library of simulated signals which have been produced by modeling the electric field inside the detectors, and testing different $0\nu\beta\beta$ decay positions.

A zoom of selected events in the range 2000-2050 keV by the two pulse shape discrimination approaches is shown in Fig. 3.8. In Fig 3.9 the final fit, which consider both pulse shape discrimination approaches, has been shown.

After the pulse shape discrimination, the background index has been reduced, the quoted value is ~ 0.005 counts/(keV·kg·yr).

The Klapdor's analysis is not universally accepted. Most important criticism are about the pulse shape discrimination approach, the background model and the detectors efficiency [6] [7].

The first goal of GERDA is to check the Klapdor's claim.
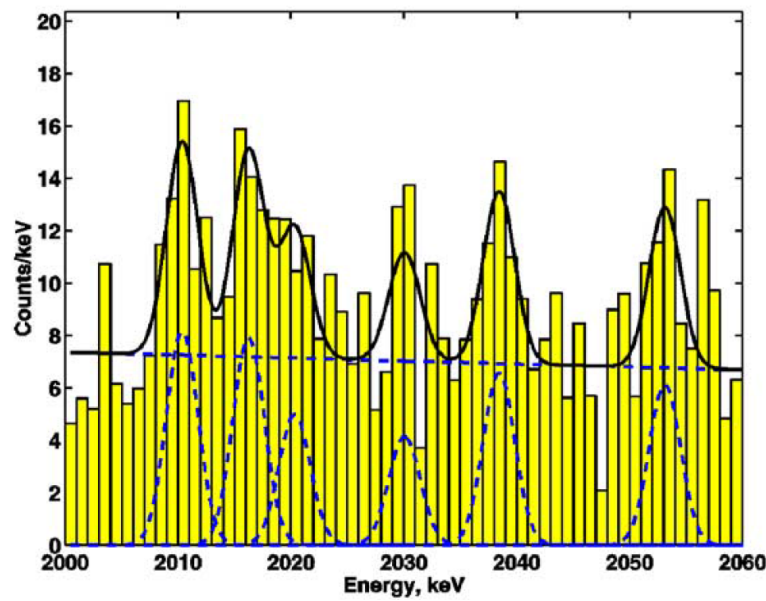
Figure 3.6: HdM: The total sum spectrum of all five detectors in the range 2000-2060 keV from November 1995 to May 2003. The collected exposure is 56.66 kg·yr, and the background index is 0.113 ± 0.007 counts/(keV·kg·yr) [8].
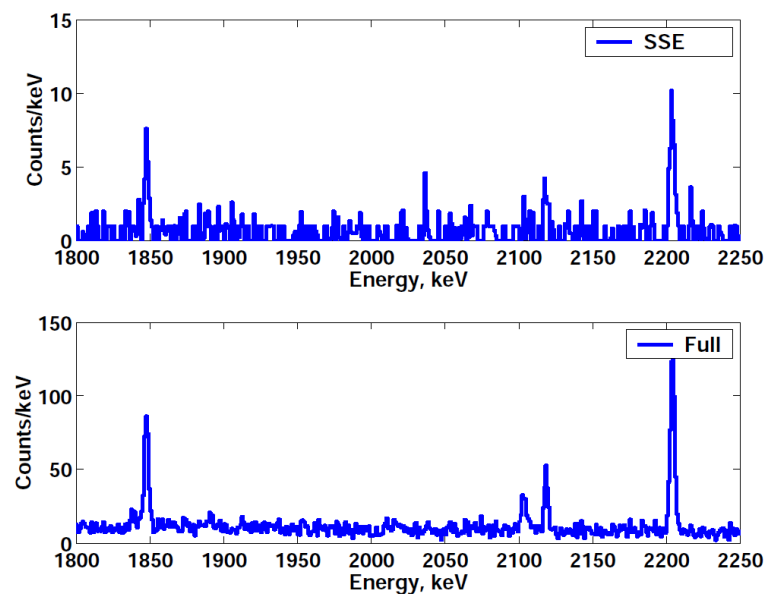
Figure 3.7: HdM - Top: the pulse shape selected spectrum (selected by neuronal network) with detectors ANG2, ANG3, ANG4, ANG5 from November 1995 to May 2003 in the energy interval 1800-2250 keV. Bottom: the full spectrum in the same energy range [8].
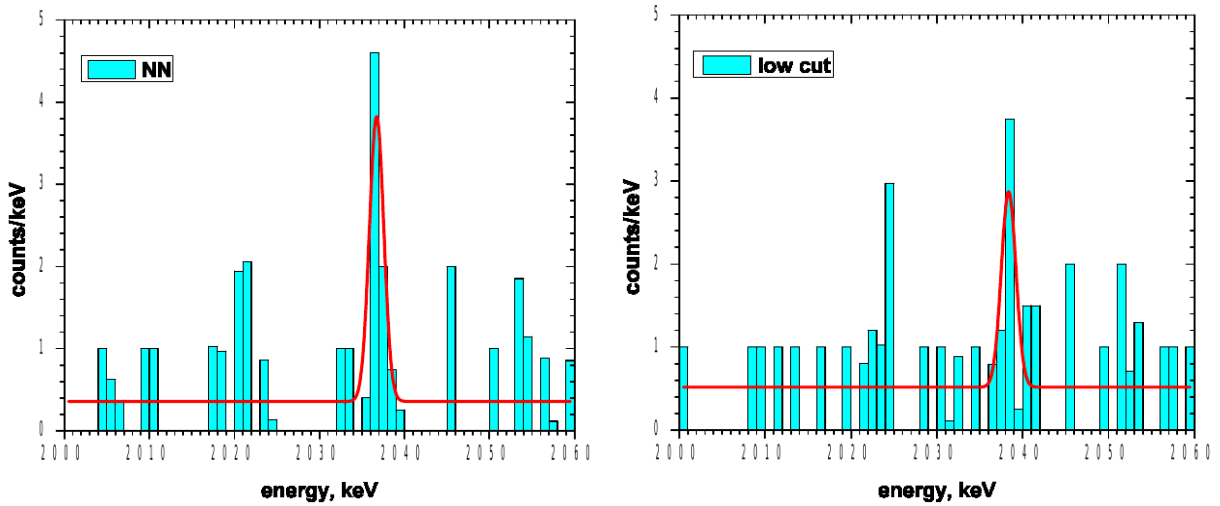
Figure 3.8: On the left: the pulse shape selected spectrum (selected by neuronal network) with detectors ANG2, ANG3, ANG4, ANG5 in the energy range 2000-2060 keV. The signal near $Q_{\beta\beta}$ is found on a 6.6σ confidence level: 7.39 ± 1.12 events. On the right: the pulse shape selected spectrum (selected by the zero range library after a low χ^2 cut) for the same detectors and in the same energy range. The signal near $Q_{\beta\beta}$ is found on a 4.0σ confidence level: 5.03 ± 1.25 events [5].
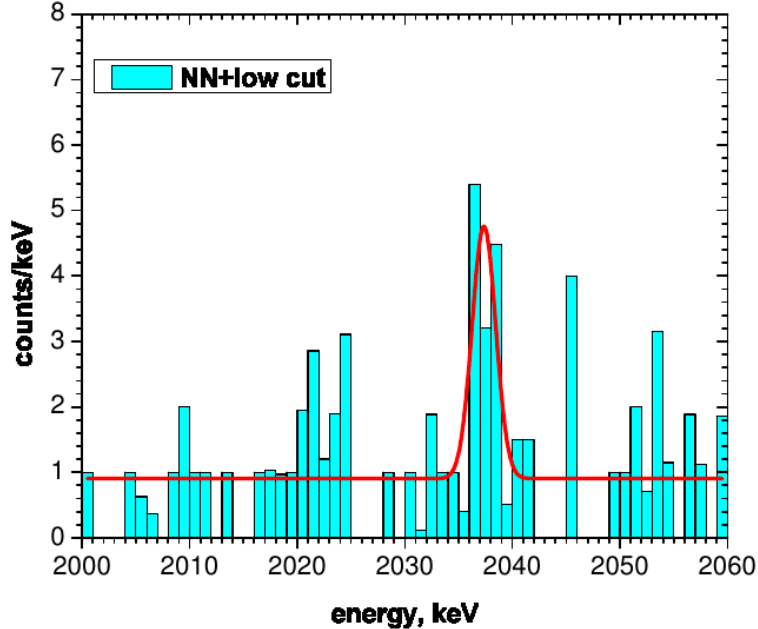
Figure 3.9: HdM - The sum of the neuronally network selected (NN) pulses and of the spectrum selected by the zero range library (cut on low-χ^2 fits), measured with detectors ANG2, ANG3, ANG4, ANG5 from 1995 to 2003 in the energy range of (2000-2060) keV. Shown are events observed in the full detector. The signal near $Q_{\beta\beta}$ is found on a 5.2σ confidence level: 10.64 ± 2.06 events [5].

3.3.2   IGEX

IGEX (International Germanium EXperiment) [9] run with 3 detectors, namely RG1, RG2, RG3, for a total mass of 6.3 kg. After a total exposure of 8.87 kg·yr of ^{76}Ge, they provided the lower limit

$$T_{1/2}^{0\nu\beta\beta} \geq 1.57 \cdot 10^{25} \text{ yr.}$$

Bibliography

[1] Berger M., Coursey J., Zucker M., and Chang J., *ESPAR, PSTAR, and ASTAR: Computer programs for Calculating Stopping-Power and Range Tables for Electrons, Protons, and Helium Ions* (2005).

[2] Glenn F. Knoll, *Radiation Detection and Measurement*, 4th, 2010.

[3] Berger M., *Photon Cross Section Database* (2012).

[4] J. Roth, J. H. Primbsch, and R. P. Lin (1984).

[5] H.V. Klapdor-Kleingrothaus and I.V. Krivosheina, *The evidence for the observation of $0\nu\beta\beta$ decay: The identification of $0\nu\beta\beta$ events from the full spectra*, Mod.Phys.Lett. **A21** (2006), 1547-1566.

[6] C.E. Aalseth et al., *Comment on "Evidence for neutrinoless double beta decay"*, Mod.Phys.Lett. **A17** (2002), 1475-1478, available at `arXiv:hep-ex/0202018`.

[7] Bernhard Schwingenheuer, *Status and prospects of searches for neutrinoless double beta decay* (2012), available at `arXiv:1210.7432[hep-ex]`.

[8] Klapdor-Kleingrothaus H.V., A. Dietz, I.V. Krivosheina, and O. Chkvorets, *Data acquisition and analysis of the Ge-76 double beta experiment in Gran Sasso 1990-2003*, Nucl.Instrum.Meth. **A522** (2004), 371-406, available at `arXiv:hep-ph/0403018`.

[9] C.E. Aalseth et al., *The IGEX Ge-76 neutrinoless double beta decay experiment: Prospects for next generation experiments*, Phys.Rev. **D65** (2002), 092007, available at `arXiv:hep-ex/0202026`.

Chapter 4

Design of the GERDA experiment

Introduction

In this chapter I will describe the main features of the GERDA experimental setup and the GERDA scientific plan.

4.1   GERDA concepts

The GERDA experiment is located in the hall A at the Laboratori Nazionali del Gran Sasso of INFN. After a commissioning period, the data acquisition for scientific analysis started on November 2011, and is currenly ongoing. The characteristic feature of GERDA is that detectors do not operate in a vacuum cryostat, like the previous experiments, but in a stainless-steel cryostat filled of liquid argon. There are few benefits from this:

- Liquid argon acts as cooling medium

- Liquid argon acts as passive shielding. The gamma cross section in LAr is shown in Fig. 4.1

- Liquid argon will act as an active shield, when it will instrumented by photon detectors for the Phase II of the experiment.

The first idea was a copper cryostat filled by liquid nitrogen, but for security concerns about a big copper cryostat, the stainless-steel cryostat was chosen. Then, to limit the background due to γ-emitting contamination in the cryostat, the cooling medium of the project changed from liquid nitrogen to liquid argon, because liquid argon is more dense. The cryostat is surrounded by a big tank filled by ultrapure water and equipped by photomultipliers, which acts as a muon veto. When muons traverse the tank, Cherenkov radiation is emitted and detected. Another complementary part of the muon veto is made
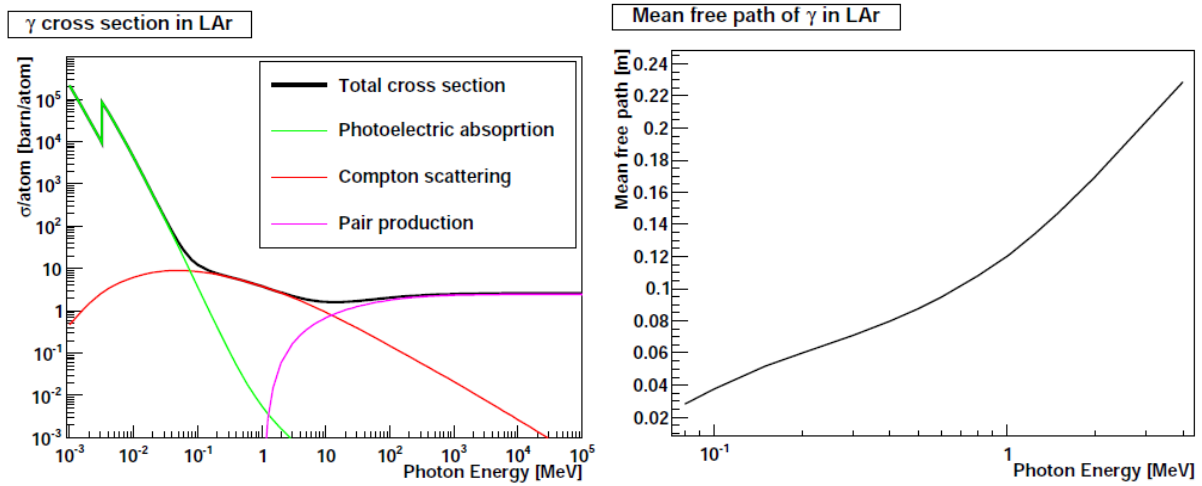
Figure 4.1: Gamma in LAr. On the left: the contribution of different mechanisms to the total cross section, as a function of the gamma energy. Compton scattering and pair production are the main mechanisms for gamma above 2 MeV. On the right: the mean free path as a function of the energy. Data from [1].

of plastic scintillators at the top of the clean room, to detect nearly vertical muons.

Basic sketches of the GERDA construction are shown in Figs 4.2 and 4.3.

Another key idea implemented in GERDA is to limit the material, and then possible sources of radioactivity, around the detectors as much as possible. Then, in the cryostat the detectors are arranged in a string structure.

The current lock-system is able to manage two chains of string. The first one is able to manage one string, the second one is able to manage three strings of detectors.

Figure 4.2: Artists view (Ge array not to scale) of the Gerda experiment as described in detail in the following sections: the germanium detector array (1), the LAr cryostat (2) with its internal copper shield (3) and the surrounding water tank (4) housing the Cherenkov muon veto, the Gerda building with the superstructure supporting the clean room (5) and the lock (6, design modified). Various laboratories behind the staircase include the water plant and a radon monitor, control rooms, cryogenic infrastructure and the electronics for the muon veto.
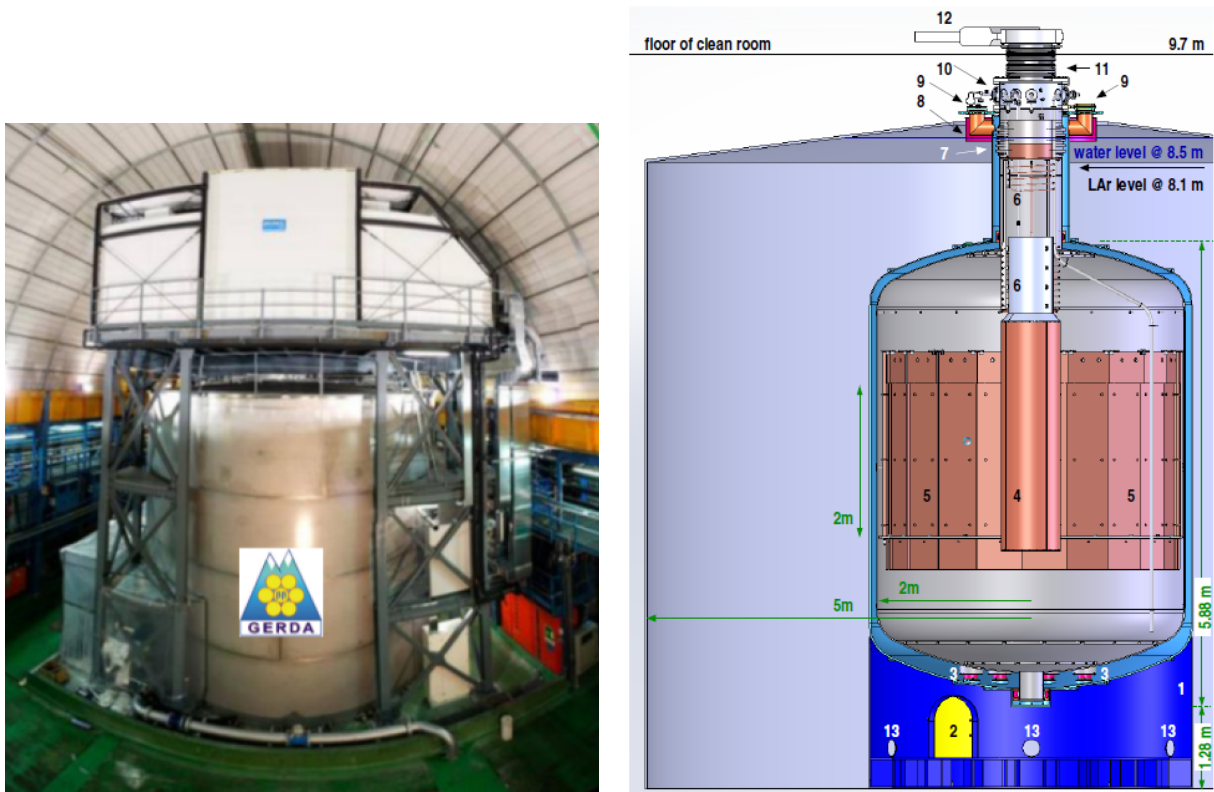
Figure 4.3: Cross section of the LAr cryostat inside the water tank (right part cut away). The following components are indicated: skirt (1), access hole (2), Torlon support pads (3), radon shroud (4), internal copper shield (5), lower and upper heat exchanger (6), bellow in neck of inner vessel (7), balcony (8), DN200 ports (9), manifold (10), bellow between cryostat and lock (11) and DN630 shutter (12). The skirt provides 6 mounts for PMTs (13).

4.2 GERDA detectors

GERDA uses the Germanium Detector which previously operate in HdM and IGEX experiments. Then, it is possible to check the Klapdor's claim [2] by using the same detectors! Specifications for these coaxial detectors are presented in Tab. 4.1. The active masses of these detectors were assessed at typically $\sim 87\%$ by comparing γ ray detection efficiency to Monte Carlo simulations of the diodes with dead layer thickness varied.

Detector	Diameter	Length	Mass	^{76}Ge abundance
	mm	mm	g	Mass fraction
ANG1	58.5	68	958	0.859(13)
ANG2	80.0	107	2833	0.866(25)
ANG3	78.0	93	2391	0.883(26)
ANG4	75.0	100	2372	0.863(13)
ANG5	78.5	105	2746	0.856(13)
RG1	77.5	84	2110	0.8551(10)
RG2	77.5	84	2166	0.8551(10)
RG3	79.0	81	2087	0.8551(10)

Table 4.1: Characteristics of enriched coaxial detectors coming from HdM and IGEX. These detectors are presently in the cryostat. The number in the last column give the $1\sigma-$uncertainties. The total mass is about 17.7 kg.

Moreover, natural detectors coming from the GENIUS-TF experiment are used to test the setup and to improve anticoincidence cuts. They are described in Tab. 4.2. A string of coaxial detectors is shown in Fig. 4.4.

Detector	Diameter	Length	Mass	^{76}Ge abundance
	mm	mm	g	Mass fraction
GTF32	89	71	2321	0.078
GTF42	85	82.5	2467	0.078
GTF44	84	84	2465	0.078
GTF45	87	75	2312	0.078
GTF110	84	105	3046	0.078
GTF112	85	100	2965	0.078

Table 4.2: Characteristics of natural detectors coming from the GENIUS-TF experiment which have been used in the commissiong phase of GERDA.

The collaboration is producing and testing a new set of enriched detectors: BEGe (Broad Energy GErmanium) detectors from Canberra Semiconductors [3]. They will constitute a small fraction of the total mass in the Phase I, but their production is ongoing, and the BEGe contribution to the total mass will be very relevant in the Phase II. BEGe have been chosen because of superior pulse shape discrimination features, as I will show in the next chapters. They are quite small compared to the coaxial detectors, as it is possible to understand from Fig. 4.5. Specifications of BEGe detectors presently in the GERDA cryostat are shown in Tab. 4.3.

Figure 4.4: Left: a string of three enrGe detectors is inserted into the mini-shroud. This work is performed in the glove box of the clean room. Right: closed detector string and 3-channel preamplier inside a copper box about 30 cm above the string. The connections between the preamplifier and detectors are made with Teflon insulated copper strips that are tightly fixed to prevent microphonics. In the background, part of the 3-string lock is visible.
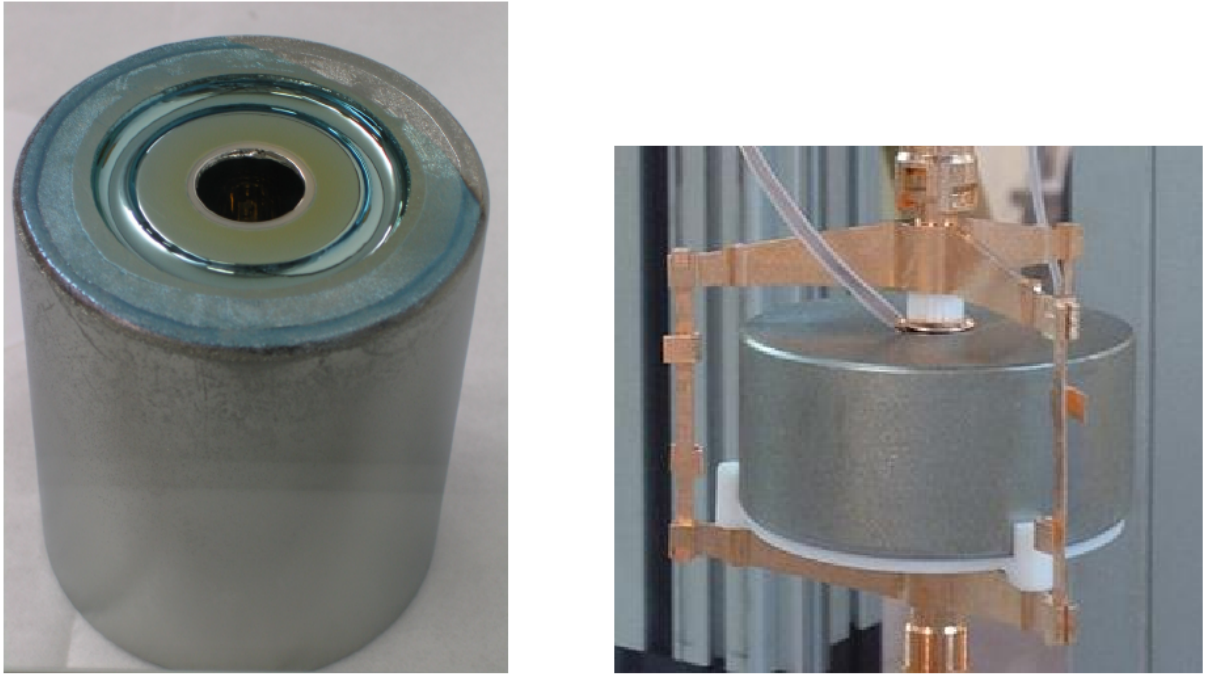
Figure 4.5: Left: a coaxial detector. Right: a BEGe detector. Figures are not in scale.

Detector	Mass
	g
GD32B	717
GD32C	743
GD32D	723
GD35B	812
GD35C	635

Table 4.3: Characteristics of the enriched BEGe detectors presently in the cryostat.

4.2.1 Calibrations

In order to calibrate the detectors within the LAr cryostat, three ^{228}Th calibration sources are brought into the vicinity of the crystals. The energy calibration of the diodes is performed by using 7 prominent lines in the spectrum: 510.8 keV, 583.2 keV, 727.3 keV, 860.6 keV, 1620.5 keV, 2103.5 keV, 2614.5 keV. To preserve disk space, energy thresholds in calibrations are higher than a normal run, and lower energy lines are not acquired.

4.3   GERDA present and future

To conclude the chapter, a quick look on the GERDA Roadmap.

Currently GERDA is in first Phase of the experiment. Phase I is characterized by the 4-strings lock. The goal of the Phase I is to check the Klapdor's claim. To reach the required sensitivity, an exposure of 20 kg·yr with a background index of 0.02 counts/(keV·kg·yr) is planned. By considering an energy window of 5 keV, the expected number of background events equal to

$$N_b[\text{Phase I}] = MtB\Delta E = 2.$$

A second Phase is in advanced state of preparation. In the Phase II, a significant lock improvement is planned, because it should be able to handle more strings of detectors.

Moreover, the liquid Argon will be instrumented to detect the scintillation light and drop events in coincidence with it, in the same way that it is doing with the signals from the muon veto.

The goal is to reach an exposure of 100 kg·yr at a BI of 0.001 counts/(keV·kg·yr), so the expected number of background events is

$$N_b[\text{Phase II}] = 0.5.$$

For pure Majorana exchange and the case that no signal is seen, this will constrain the module of the effective neutrino mass to less than about 100 meV.

Bibliography

[1] Berger M., *Photon Cross Section Database* (2012).

[2] H.V. Klapdor-Kleingrothaus and I.V. Krivosheina, *The evidence for the observation of $0\nu\beta\beta$ decay: The identification of $0\nu\beta\beta$ events from the full spectra*, Mod.Phys.Lett. **A21** (2006), 1547-1566.

[3] *Canberra Industries*, available at `http://www.canberra.com`.

Part III

Digital Signal Processing

Chapter 5

GERDA Digital Signal Processing

Introduction

In this section I will introduce the GERDA electronic chain and the present approach to the energy reconstruction of the acquired signals.

5.1   Linear systems

If the GERDA electronic chain is linear, and I will assume that, it is possible to describe the output signal as a convolution of the input current signal with a response function, which is independent from the input

$$Q[t] = \int_{-\infty}^{\infty} I[t']R_{\text{full}}[t - t']dt'.$$

This could be seen as the first-order term of a Volterra series. If the system is linear, the first-order term fully describes the system [1].

$I[t]$ is the current signal induced into the electronic chain, $Q[t]$ is the output charge signal, $R_{\text{full}}[t]$ is the impulse response of the system. For a Dirac-Delta current $I[t] = q_0\delta[t]$, the output is $q_0 R[t]$.

To preserve causality (the past is not dependent by the future), we expect a response function equal to 0 for $t - t' < 0$, and we can define the positive response function $R[t]$ by the relation

$$R_{\text{full}}[t] = R[t]H[t]$$

(where H is the Heaviside step function) and write

$$Q[t] = \int_{-\infty}^{t} I[t']R[t - t']dt'. \tag{5.1}$$

We can include in the response function the response of the FADC, so that we can write for the digitized signal

$$q[n] = Q[t[n]] \tag{5.2}$$

where n is the sample number, and $t[n]$ describes the sampling pattern in time. I will preserve this notation: capital letters for continuos quantities, lowercase letters for discrete sampled quantities.

5.1.1   Fast sampling approximation

From (5.2) we can write

$$q[n] = \int_{-\infty}^{t[n]} I[t']R[t[n] - t']dt' = \sum_{j=-\infty}^{n} \int_{t[j-1]}^{t[j]} I[t']R[t[n] - t']dt'.$$

If the sampling period is very short we can approximate the integral by the product of the mean values

$$\int_{t[j-1]}^{t[j]} I[t']R[t[n] - t']dt' \sim \Big(\frac{1}{\Delta t[j]} \int_{t[j-1]}^{t[j]} I[t']dt'\Big)\Big(\frac{1}{\Delta t[j]} \int_{t[j-1]}^{t[j]} R[t[n] - t']dt'\Big)\Delta t[j]$$

and the mean values with the values at an interval limit

$$\frac{1}{\Delta t[j]} \int_{t[j-1]}^{t[j]} I[t']dt' \sim I[t[j]] \equiv i[j]$$

$$\frac{1}{\Delta t[j]} \int_{t[j-1]}^{t[j]} R[t[n] - t']dt' \sim R[t[n] - t[j]]$$

so that we can write

$$q[n] \sim \sum_{j=-\infty}^{n} i[j]R[t[n] - t[j]]\Delta t[j]. \tag{5.3}$$

This expression is a bit dangereous. The full expression is

$$q[n] = \sum_{j=-\infty}^{n} i[j]R[t[n] - t[j]]\Delta t[j] + e[n]$$

where $e[n]$ is the unknown "error", which measures the quality of the approximation. Its standard deviation is related to the sampling period. It is a common practice to recover the vector $i[j]$ by inverting the system (5.3) ignoring the error, but it is always important to understand that this could be a limit.

Concerning the deconvolved signal, it is clear that we can write

$$q_{dec}[n] = \sum_{j=-\infty}^{n} i[j]\Delta t[j]. \tag{5.4}$$

5.1.2   Homogeneous sampling

Note that in the case of homogeneous sampling of the signal (stored values equally spaced in time) it is possible to write

$$t[n] = n\Delta t \qquad \Delta t[n] = \Delta t.$$

Then the previous expressions (5.3) and (5.4) reduce to

$$q[n] = \sum_{j=-\infty}^{n} i[j] R[(n-j)\Delta t]\Delta t \equiv \sum_{j=-\infty}^{n} i[j] r[n-j]\Delta t$$

$$q_{dec}[n] = \sum_{j=-\infty}^{n} i[j]\Delta t.$$

5.2   The GERDA electronic chain

A sketch of the GERDA electronic chain is presented in Fig. 5.1.
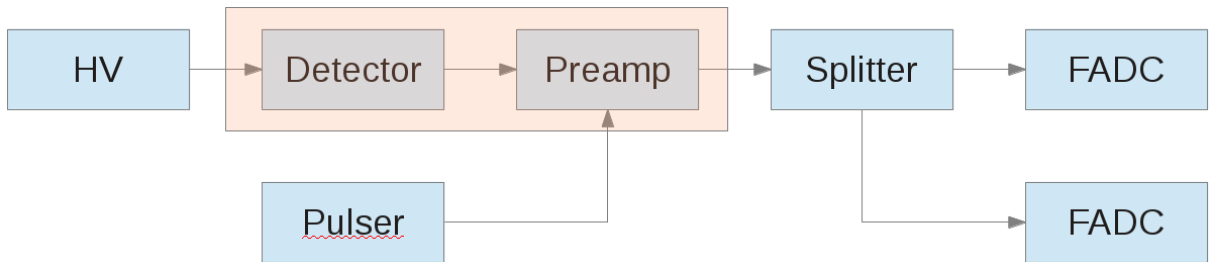
Figure 5.1: The electronic chain: detectors are feeded by High Voltage. The current from the detector is integrated in a charge sensitive preamplifier. Note that the preamplifier is located into the Argon volume (pink area). In principle, the signal could be sent to two different Flash ADC systems (FADC). Presently, we are using a single FADC system, whose sampling frequency is 100 MHz. Test pulses are sent to the preamplifier every 20 seconds.

The key component to understand the signal shape is the charge-sensitive preamplifier, sketched in Fig. 5.2. It is located in a copper box into the LAr volume, close to the detectors. The charge-sensitive preamplifier basically integrates the charge of the incoming pulse. The charge Q is stored on the capacitor C_f and then removed through the feedback resistor R_f. The output voltage is independent of the detector capacitance:

$$V_{out} \simeq -\frac{Q}{C_f}.$$

In this standard configuration, a good model for the response function is an exponential decay, characterized by the time constant of the preamplifier $\tau = C_f R_f$

$$R_1[t] = \exp\left[-\frac{t}{\tau}\right].$$

The time constant is designed to be very long compared to the pulse duration, to have a full charge collection in the capaccitor, then it is evident from (5.1) that the current signal is integrated in a charge signal. Then, the most important quantity of interest, energy, is proportional to the amplitude of the signal.
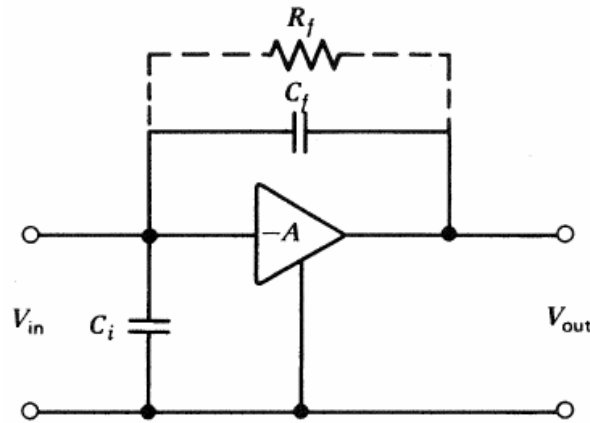
Figure 5.2: The charge sensitive preamplifier. C_f and R_f are the feedback capacitor and resistor.

5.3   The GERDA digitized signal

Fig. 5.3 gives an example of the acquired signals. Presently data are digitized by a 14 bit, 100 MHz (thus the sampling period is 10 ns) Flash ADC. During the normal acquisition, when the signal exceeds the trigger threshold in any of the channels, all channels are readout. The waveforms consist of 16384 samples, which corresponds to a length of 163.84 μs. For the channel which triggered the acquisition, the trigger position is located near the center of the digitized waveform.

During a calibration, things are a bit different. To preserve disk space, in the external parts of the waveforms samples are summed in groups of four. Then, the digitized signal is sampled at 40 ns in the baseline region, at 10 ns in the central region (400 high-frequency samples) and at 40 ns in the tail region. Then the number of samples in a calibration run is given by

$$n_s = 400 + (16384 - 400)/4 = 4396$$

and the sampling rate of the stored waveforms is variable. Moreover, only the triggered channels are stored.

Presently, a calibration run consists in $\sim$ 1-2 millions of events, and it takes $\sim$ 1 hour. During a normal run, most of the events are the test pulse signals which are sent every 20s. Then we have $\sim$ 4320 test pulses/day. Physical events in the full energy spectrum are about the half. Then, it is easy to understand that calibrations largely dominate the disk space needed for the data.
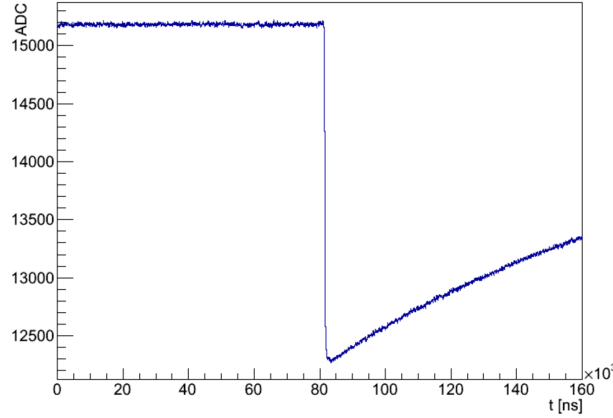
Figure 5.3: A raw GERDA signal from a coaxial detector: the signal is inverted (zero current = maximum). It is possible to divide the waveform into three parts: the baseline (before the start of the current), the rising part (the central part of the waveform) and the decaying part.

5.3.1   Energy reconstruction resampling

To keep everything simple and consistent between a normal run and a calibration run, the first step of the energy reconstruction chain is to resample the waveforms with a homogeneous sampling of 40 ns. This could seem a limit in our approach, instead, as I will show in the next chapters, it does not seem so relevant. Clearly, our approach to the pulse shape discrimination is different, and for pulse shape discrimination it is important to keep the full resolution provided by the FADC.

5.4   Deconvolution of the signal

A common approach, for a charge sensitive preamplifier response with a homogeneous sampling rate, is to start the digital signal processing with the Moving Window Deconvolution filter (MWD):

$$q_{mwd,m}[n] = q[n] - q[n-m] + \left(1 - \exp\left[-\frac{\Delta t}{\tau}\right]\right) \sum_{j=n-m}^{n-1} q[j]$$

where m is the size of the window in samples. Usually $m\Delta t$ is equal to the shaping time used in the next steps of the signal processing chain.

Note that for $\tau \to \infty$ (long time constant approximation) this expression reduces to

$$q_{mwd,m}[n] \sim q[n] - q[n-m]$$

which is the difference operator. Instead of constructing it, I will show how the filter works. For a charge injection

$$i[n]\Delta t = q_0 \delta_{n,0}$$

the output is

$$q[n] = \begin{cases} 0 & n < 0 \\ q_0 \exp\left[-\frac{n\Delta t}{\tau}\right] & n \geq 0 \end{cases}$$

and the deconvolved signal is

$$q_{dec}[n] = \begin{cases} 0 & n < 0 \\ q_0 & n \geq 0 \end{cases} .$$

We can study the filter response to the charge injection in the range $n = [0, m-1]$. It is clear than $q_{dec,m}[0] = q_0$. Then we can write for $n > 0$

$$q_{mwd,m}[n] = q_0 \exp\left[-\frac{n\Delta t}{\tau}\right] + \left(1 - \exp\left[-\frac{\Delta t}{\tau}\right]\right) \sum_{j=0}^{n-1} q_0 \exp\left[-\frac{j\Delta t}{\tau}\right]$$

$$= q_0 \exp\left[-\frac{n\Delta t}{\tau}\right] + \left(1 - \exp\left[-\frac{\Delta t}{\tau}\right]\right) \left(\frac{\exp\left[-\frac{(n-1)\Delta t}{\tau}\right]\left(\exp\left[\frac{n\Delta t}{\tau}\right] - 1\right) q_0}{\exp\left[\frac{\Delta t}{\tau}\right] - 1}\right)$$

$$= q_0 \exp\left[-\frac{n\Delta t}{\tau}\right] + q_0 - q_0 \exp\left[-\frac{n\Delta t}{\tau}\right] = q_0 = q_{dec}[n].$$

Ok, this filter acts as a deconvolution for an exponential response. After the pulse, one has a flat region, as you can expect from a deconvolution algorithm.

We can also study the long time constant approximation. Again $q_{dec,m}[0] = q_0$. Then we have

$$q_{mwd,m}[n] = q_0 \exp\left[-\frac{n\Delta t}{\tau}\right].$$

At the end of the window we have

$$q_{mwd,m}[m-1] = q_0 \exp\left[-\frac{(m-1)\Delta t}{\tau}\right]$$

then

$$\frac{q_{mwd,m}[m-1]}{q_{dec,m}[0]} = \exp\left[-\frac{(m-1)\Delta t}{\tau}\right].$$

The region is not flat any longer.

5.5 The energy reconstruction

The default energy reconstruction is characterized by a sequence of linear transforms of the acquired signal, which are sketched in Fig. 5.4. After an inversion and a baseline restoration (before the pulse the charge is 0 if there is not a tail from a previous event), the Moving Window Deconvolution filter is applied. In GERDA, presently the long time constant approximation of the MWD is used, then the filter reduces to the difference operator. According to Jordanov [2] this is good because the time constants are way longer compared to the current length. A "squared" pulse is obtained (Fig. 5.4, the second waveform). The energy is proportional to the signal amplitude. To improve the signal to noise ratio, a standard approach is to apply a set of moving window averages to the signal. The moving window average can be described as

$$q_{mwa,m}[n] = \frac{1}{m} \sum_{j=n-m+1}^{n} q[j]$$

The shaping time $m\Delta$t, where Δt is the sampling period, is chosen to be the same of the first step, 5 μs for all channels. The final result, after many averages ($\sim$ 25 in the present energy reconstruction approach) is a signal shaped in a nearly-gaussian way. Because we did averages, the maximum amplitude is still our quantity of interest. Clearly, to obtain the physical energy value, a calibration is required.

Other approaches to the energy reconstruction have been studied, e.g. the trapezoidal filter described in Knoll (Fig. 5.5). In the mean case, the obtained results are worse: then it seems that "averaging" (noise reduction) is more important than, e.g., the correction for different risetimes.

5.6 GELATIO

The energy reconstruction algorithms are implemented in our digital signal processing software, which is named "GELATIO" [3] [4]. The key feature of GELATIO is that it is able to manage different signal sources in a common way. The GELATIO pipeline is sketched in Fig 5.6. Data coming from Germanium detectors, photomultipliers, Monte Carlo simulations are converted in a common ROOT-Based format [5]. GELATIO consists of many analysis modules for different tasks: baseline restoration, energy reconstruction, risetime estimation... An advanced Graphical User Interface (GUI) has been developed, by me, to permit a simple access to all the GELATIO features, e.g. the configuration of the parameters for each module. A few screenshots of the GUI in Fig. 5.7. The GUI is able to handle many channels, e.g. in Fig. 5.8 it is possible to see 96 waveforms at the same time, which describe a muon event in the muon veto data stream.
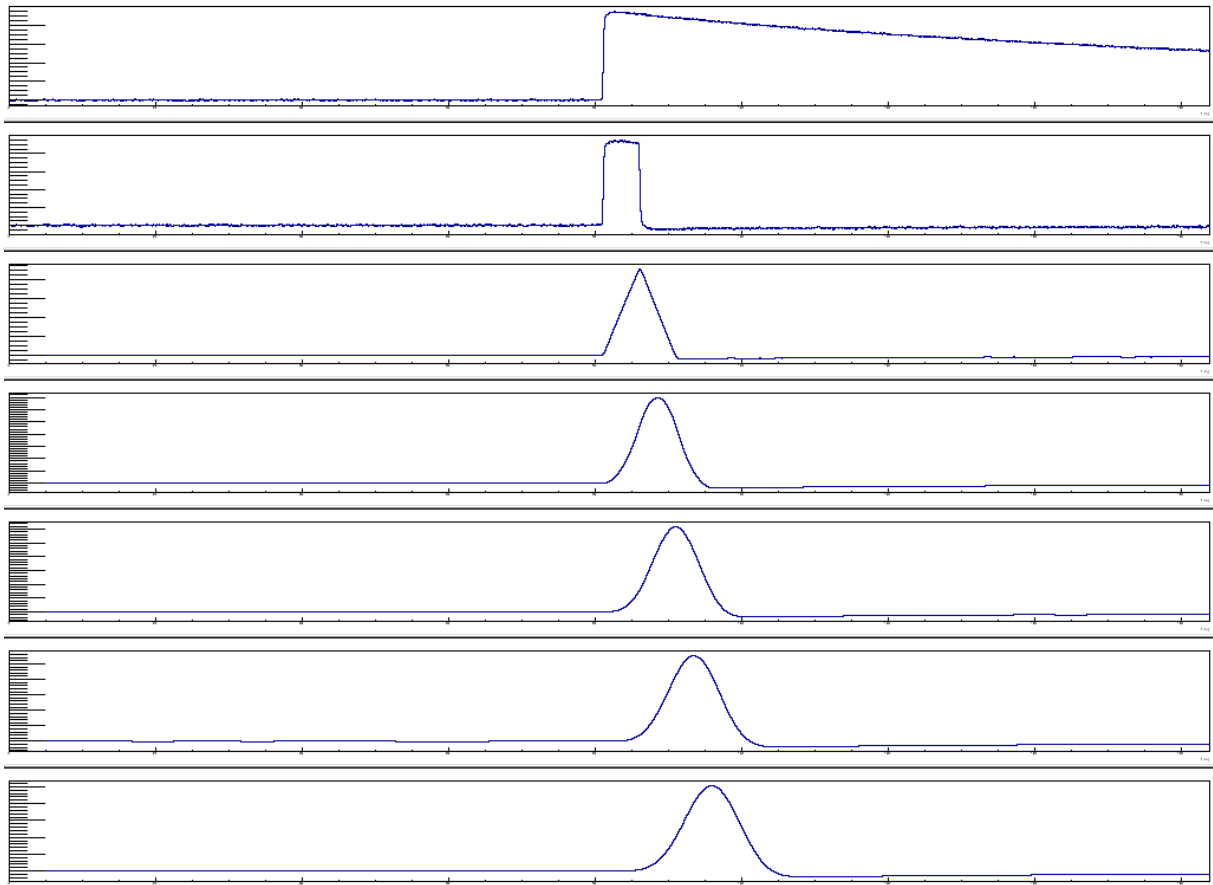
Figure 5.4: GERDA default energy reconstruction chain: after an inversion and the baseline subtraction, the obtained typical signal shape is at the top. Then, after a MVD and many moving window averages, it acquires a nearly-gaussian shape.
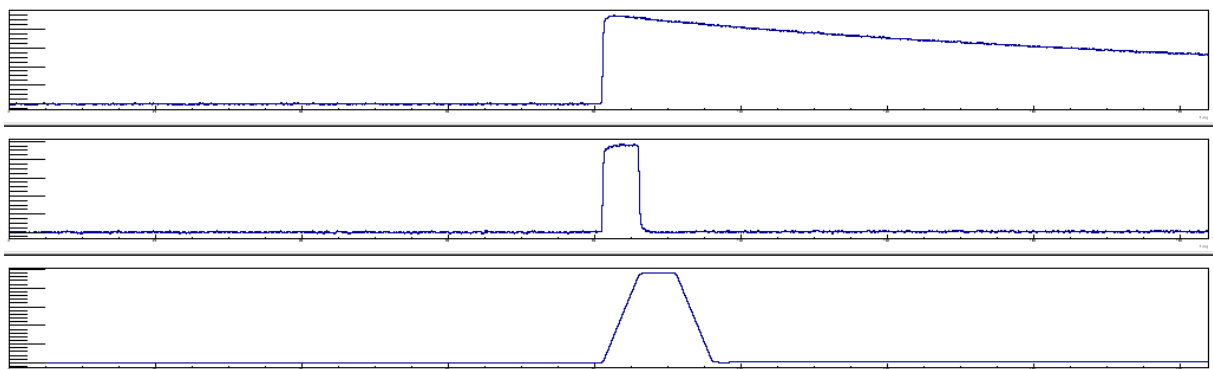
Figure 5.5: GERDA energy reconstruction alternative approach: after a Moving Window Deconvolution using a physical time constants, the signal is shaped in a trapezoidal way. According to Knoll [6], this signal shaping permits a correction of "the ballistic defects": pulses with different rise times have the same amplitude. The maximum height is proportional to the energy.
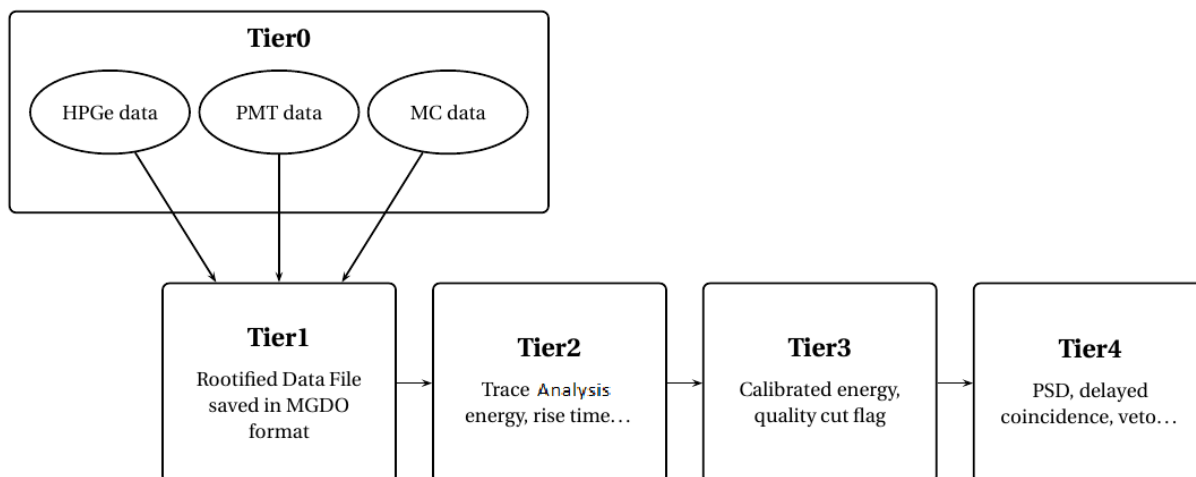
Figure 5.6: The hierarchical organization of the data in GELATIO. The framework organizes the output of each step of the analysis in a different level (Tier) starting from the raw data (Tier0) up to the condensed parameter of the final analysis. The Tier1 contains the same information of the raw data but encoded with a different format based on ROOT.

Bibliography

[1] Schetzen M., *The Volterra and Wiener Theories of Nonlinear Systems*, 1980.

[2] Valentin T. Jordanov and Glenn F. Knoll, *Digital synthesis of pulse shapes in real time for high resolution radiation spectroscopy* (1994).

[3] M. Agostini, L. Pandola, P. Zavarise, and O. Volynets, *GELATIO: A General framework for modular digital analysis of high-purity Ge detector signals*, JINST **6** (2011), P08013, available at `arXiv:1106.1780[physics.data-an]`.

[4] M. Agostini, L. Pandola, and P. Zavarise, *Off-line data processing and analysis for the GERDA experiment*, J.Phys.Conf.Ser. **368** (2012), 012047, available at `arXiv:1111.3582[physics.data-an]`.

[5] R. Brun and F. Rademakers, *ROOT: An object oriented data analysis framework*, Nucl.Instrum.Meth. **A389** (1997), 81-86.

[6] Glenn F. Knoll, *Radiation Detection and Measurement*, 4th, 2010.

(a)

(b)

(c)

(d)
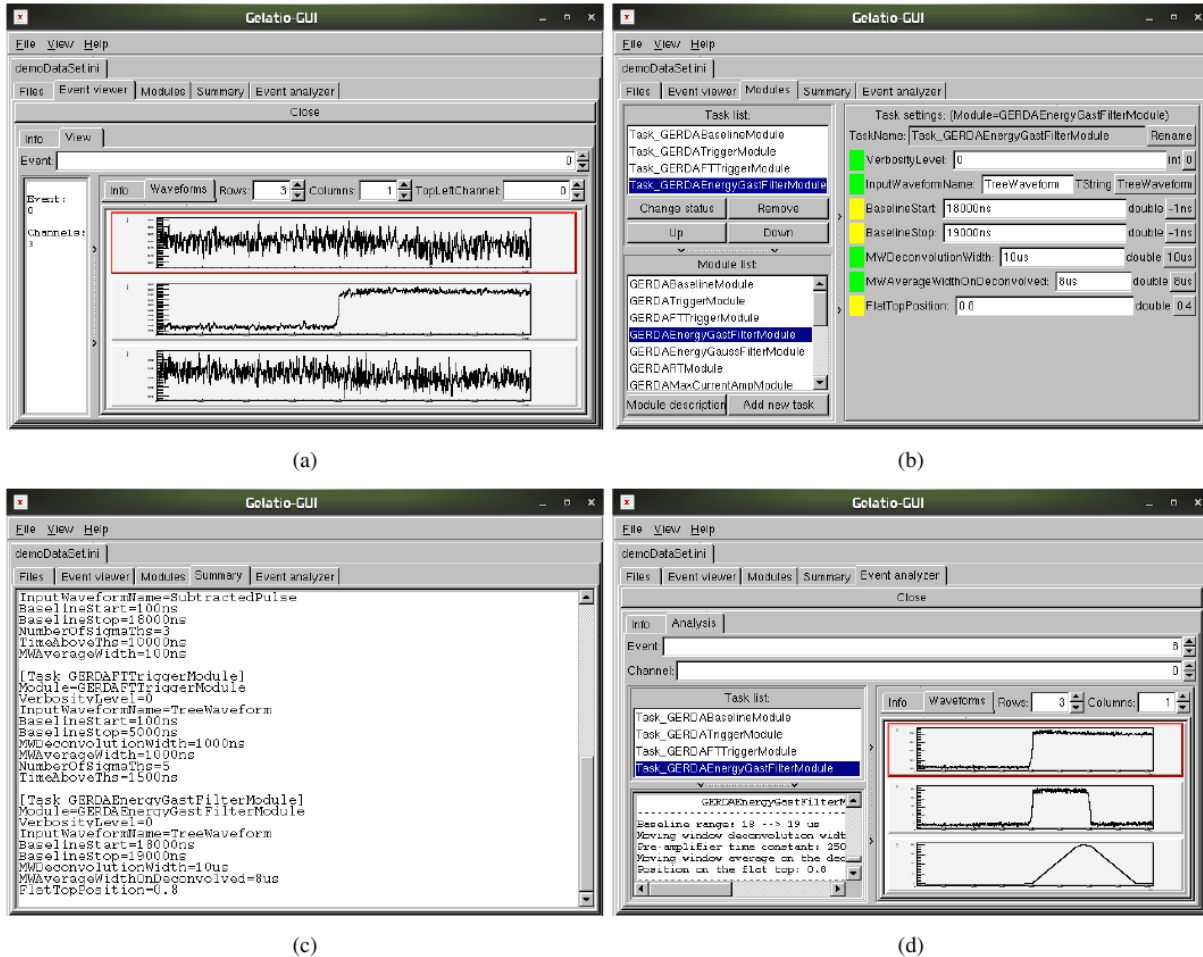
Figure 5.7: Screenshots of the GELATIO GUI. The input Tier1 file comes from a GERDA background run and contains three traces per event. The screenshots show the tools and utilities available in the GUI: (a) Event displayer. The signals from the three channels (three detectors) are displayed together. (b) INI (Initialization file) file editor. It can be used to select and customize the analysis tasks to be performed. The "Module list" contains all the analysis modules available in GELATIO. (c) INI output summary. It shows the human-readable INI file produced according to the user choice in the INI file editor. (d) Event analyzer. To apply the full analysis chain to a given trace. The screenshot shows the intermediate shaped traces calculated by the analysis modules which implements the Gast algorithm (the trapezoidal filter) for amplitude reconstruction.
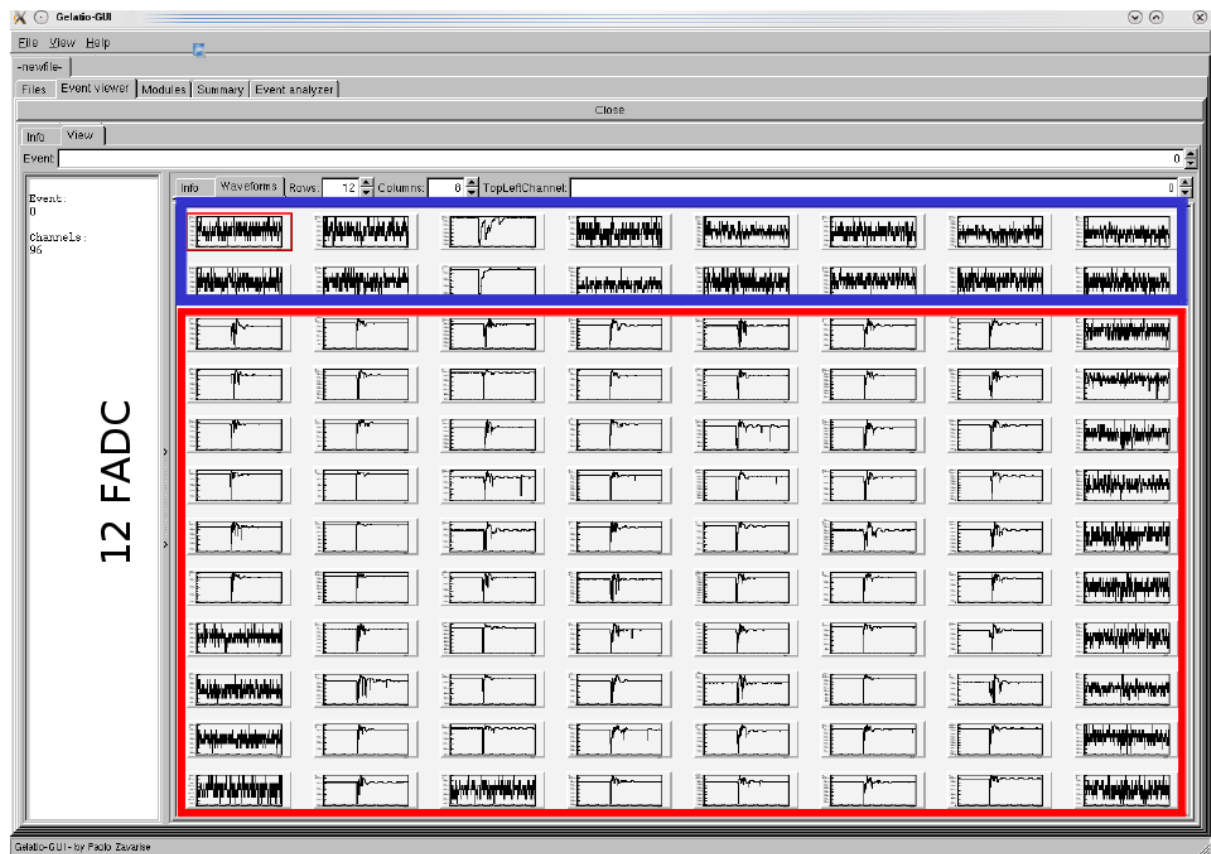
Figure 5.8: Signals from the muon veto: 12 FADC, 8 channels each one for a total of 96 channels. In the blue rectangles, signals from the plastic veto. In the red rectangles, signals from photomultipliers.

Chapter 6

Analysis of the response function

Introduction

In this section I will start to describe my approach to the signal processing, which is different compared to the official one in a few aspects. The first step of my analysis is a refined reconstruction of the response of the GERDA electronic chain.

6.1 The importance of the time constant

According to Jordanov [1], as I have explained in the previous chapter, if the input signal has a long decay constant it can be approximated as a step function. But there is an important point to discuss. Long compared to what? There are three time scales in the game:

- The sampling period (which appears in the moving window filter expression)

- The risetime (which is the physical time scale for a pulse)

- The shaping time (which is the time scale for the energy reconstruction algorithms).

The typical time scale of the pulses is like 0.5 μs. In this time, a typical exponential decaying response driven by a time constant of 150 μs, changes from 1 to

$$\exp\left[-\frac{0.5\ \mu\text{s}}{150\ \mu\text{s}}\right] \sim 0.997.$$

The shaping time that we are using in GERDA is like 5 μs. In this time, a typical response changes from 1 to

$$\exp\left[-\frac{5\ \mu\text{s}}{150\ \mu\text{s}}\right] \sim 0.967.$$

In the current default GERDA signal processing, we are working in the long time constant approximation: a step of the Digital Signal Processing (DSP) chain is a Moving Window

Deconvolution with an infinite time constant, which reduces to a difference operator.

The first goal of my analysis is to understand if, by providing a "proper" time constant, it is possible to improve the energy resolution. If the shaping time is the relevant time constant for the energy construction, I expect to obtain better results compared to the default analysis.

6.2   Analysis of the GERDA response function

The first step of my analysis chain is a study of the GERDA response function. This translates to an estimate of the time constant if the simple exponential decay model is good enough. To estimate the time constant, a fit of the tail of the pulses is probably a good solution. But in my analysis I would like to check different models for the GERDA response function. Then, something more refined is required.

My idea is to rely on calibrations data. Calibrations events are physical, and the signal path is the same of the normal runs. That is not true for test pulses, because they come from the Pulser and not from the detectors. Moreover, calibrations are part of the GERDA routine procedures, then an analysis of the response function which relies on these data could be a no-cost check for electronic non-standard behaviours.

I will proceed in the following way:

1. Create a parametric model for the current signals

2. Create a parametric model for the response function

3. Convolve the current with the response function

4. Simulate the FADC sampling (averages during the sampling period)

5. Fit the resulting function with the data for a large number of waveforms at the same time, to obtain the parameters which describe the response function.

The sampling simulation is quite important. I would like to use all the available information, then I should be able to handle the variable sampling rate in the stored calibration data. The sampling is implemented as

$$q[t] = \frac{1}{\Delta t} \int_{t-\Delta t}^{t} Q[t']dt' \tag{6.1}$$

where $q[t]$ is the sampled signal, $Q[t]$ the continuous signal and Δt the sampling period. Thus, I will work in the time domain.

Another important point is that the resulting function should be analytical, then the integrals in items 3 and 4 should be tractable.

If n_c is the number of parameters for the current signals, n_r the number of parameters for the response function, n_w the number of waveforms fitted at the same time, the number of parameters in the fit is

$$n_f = n_c \cdot n_w + n_r.$$

As I said, the number of waveforms fitted at the same time should be large enough to constrain the parameters which describe the response function in a solid way.

6.3   Simple current models

It is clear that to minimize the complexity of the optimization problem, a very simple model for the current signals is required. 3 parameters seem the minimum to me: position in time, length in time and total charge. A 2-parameters Dirac Delta current is not convincing. I found three simple possibilities which are symmetrical with respect to the central value (symmetrical shapes are simply a "maximum entropy" choice):

- Gaussian signals, truncated in time

- Flat signals

- Triangular signals.

In Fig. 6.1, the current for a start time=0, length=1 and total charge=1 (arbitrary units) for the three models. In the gaussian model one needs to fix the constant between sigma and the length. In the plot I chose sigma=1/6· length
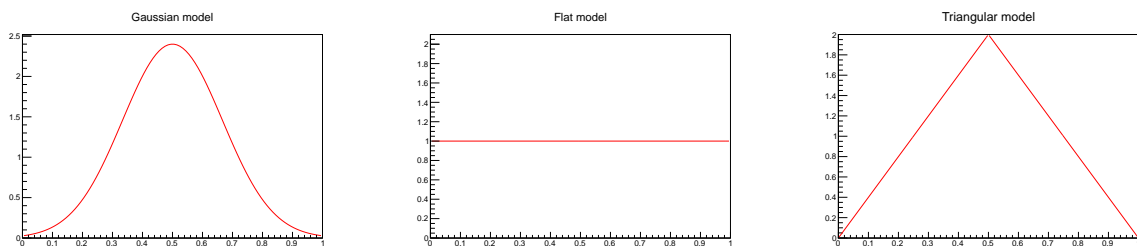
Figure 6.1: 3-Parameters models for the current.

I will test both flat and triangular models. I do not like the gaussian model because a tuning of the sigma/length relationship is required.

Note that for our purposes, which are not pulse shape analysis at the moment but the reconstruction of the response function, it is not important that the model describes the current in a perfect way. It is important to have one model especially to constrain the end point of the signal from both sides. It is clear that the information which we are looking for are contained in the tail, and that a wrong model current could alter the response in a

$< 1\mu s$ (risetime) scale. Moreover, by providing a basic model for the signal, it is possible to handle all points of all waveforms in the analysis in the same way.

6.3.1 Flat model

The current in the flat model is given by

$$I[t] = \begin{cases} i_1 & (t_s < t)\&\&(t < t_l) \\ 0 & (t < t_s)||(t_s + t_l < t) \end{cases}$$

i_1 is the intensity, t_s is the start time, t_l is the length. $\&\&$ is the logical AND, $||$ is the logical OR. The convolution of the flat model current with the simple exponential response is

$$Q[t] = \begin{cases} 0 & (t < t_s) \\ i_1\left(1 - \exp\left[-\frac{t-t_s}{\tau}\right]\right)\tau & (t_s < t)\&\&(t < t_s + t_l) \\ i_1 \exp\left[-\frac{t-t_s}{\tau}\right]\left(-1 + \exp\left[\frac{t_l}{\tau}\right]\right)\tau & (t_s + t_l < t) \end{cases}$$

and to obtain the sampled version (6.1) is needed.

6.3.2 Triangular model

The current in the triangular model is given by

$$I[t] = \begin{cases} \frac{4i_1(t-t_s)}{t_l} & (t_s < t)\&\&(t < t_s + \frac{t_l}{2}) \\ \frac{4i_1(t_s+t_l-t)}{t_l} & (t_s + \frac{t_l}{2} < t)\&\&(t < t_s + t_l) \\ 0 & (t < t_s)||(t_s + t_l < t) \end{cases}.$$

Note that

$$\int_{-\infty}^{\infty} I[t']dt' = i_1 t_l$$

thus i_1 is the mean current, t_s is the start time, t_l is the length. The convolution of the triangular model current with the simple exponential response is

$$Q[t] = \begin{cases} 0 & (t < t_s) \\ \frac{4i_1\tau\left(\left(-1+\exp\left[-\frac{-t+t_s}{\tau}\right]\right)\tau+t-t_s\right)}{t_l} & (t_s < t)\&\&(t < t_s + \frac{t_l}{2}) \\ \frac{1}{t_l}4i_1\tau\left(\tau + \exp\left[\frac{-t+t_s}{\tau}\right]\tau - 2\exp\left[\frac{t_l-2t+2t_s}{2\tau}\right]\tau + t_l - t + t_s\right) & (t_s + \frac{t_l}{2} < t)\&\&(t < t_s + t_l) \\ \frac{4\exp\left[-\frac{-t+t_s}{\tau}\right]\left(-1+\exp\left[\frac{t_l}{2\tau}\right]\right)^2 i_1\tau^2}{t_l} & (t_s + t_l < t) \end{cases}$$

and to obtain the sampled version (6.1) is needed.

6.4   Preliminary cut

It is clear that, before spending hours in the GERDA response function fits, it is important to make a quality selection of the waveforms. Very bad waveforms which are not well described by the current models, could alter the fit results.

The first cut is to reject pulser events. It is not obvious that the response from a detector current is the same that the response from a pulser signal.

Moreover, I will ignore waveforms with overflows/underflows, because the information is not complete.

6.5   Preliminary baseline scan

After that, I will filter the events according to the baseline quality. For example, two events in the same window are clearly not compatible with my big-fit model, which is made of three waveform-specific parameters (start time, end time, mean current).

A tail from a previous event is also not compatible. The correction of the baseline for a tail from a previous event is, in my opinion, one of the more difficult tasks in the DSP. Looking at the baselines there is the most evident indication that the event tail is not a pure exponential.

I would like to avoid completely the baseline problem, then my baseline cut should be strong enough. My idea is to find the maximum of the distribution of the baseline sample variance. In the hypothesis that the maximum is not altered by bad events (which I expect to have an higher baseline variance), I modeled the distribution as a χ^2, and found the effective degrees of freedom k from the relation mode=k-2. Then, I saved the 68% of the waveforms according to this distribution.

6.6   Model testing

After the waveforms selection, I decided to fit both current models to the survived waveforms. The idea is simply to choose the best model, because it is a quite long operation to fit two different models for all the selected waveforms for all the calibrations.

6.7   Preliminary quality scan

Chosen the model, I will consider only its results, and I have applied a strong quality cut on the mean squared residuals of the fit, in the same way I have done for baselines. In this case, I decided to save only 50% of the waveforms.

At the end of the cut, if the number of survived waveforms is greater than 8192, they are

sorted according to the fit quality, and only the best 8192 are selected for the big response fit. I fixed this limit to save computational time.

6.8   Global response function analysis

I would like to test the single parameter standard model

$$R_1[t] = \exp\left[-\frac{t}{\tau}\right]$$

and a "perturbation" of it. I would like to describe the perturbation by using only another parameter. My idea is to write

$$R_2[t] = \exp\left[-\frac{t}{\tau_1}\right]\left(\frac{1+\exp\left[-\frac{t}{\tau_2}\right]}{2}\right).$$

Note that this response has the same normalization for a Dirac Delta current ($R_2[0] = 1$), and that for $\tau_1 = \tau$ and a very large τ_2 it is possible to recover the basic model. It is possible to rewrite the expression as

$$R_2[t] = \frac{1}{2}\left(\exp\left[-\left(\frac{1}{\tau_1}+\frac{1}{\tau_2}\right)t\right] + \exp\left[-\frac{t}{\tau_1}\right]\right).$$

It is a linear combination of the exponentials, with the same weight. By defining

$$\tau_s = \frac{1}{\frac{1}{\tau_1}+\frac{1}{\tau_2}} < \tau_1 \qquad \tau_l \equiv \tau_1$$

we can write

$$R_2[t] = \frac{1}{2}\left(\exp\left[-\frac{t}{\tau_s}\right] + \exp\left[-\frac{t}{\tau_l}\right]\right)$$

which shows the contributions of the short and the long time constants. For $\tau_l = \tau_s = \tau$ it is possible to recover the basic response model.

Note that this complex model is not "physical", in the sense that τ_l and τ_s are not directly connected to physical quantities. It is simply a 2-parameters "extension" of the basic 1-parameter model.

To obtain the output signal, I did the convolution of the current models with the complex response function, and the the sampling integral. I chose to work in the variables τ_l, k where $\tau_s = k\tau_l$ and $0 < k < 1$ to prevent degeneration between τ_s and τ_l.

6.9   Global minimization

In my analysis $n_c = 3$, $n_w \leq 8192$, then the number of parameters is at maximum

$$n_f = 8192 \times 3 + n_r = 24576 + n_r.$$

My minimizer of choice, Minuit2 in the ROOT package, is not able to handle such a large number of parameters. The reason is that it stores in memory a lot of information for each iteration, and the memory used is proportional to the number of parameters. I am discussing with the ROOT team about a better memory use in the package.

I switched to the GNU Scientific Library minimizers [2], in particular to the BFGS2 algorithm (Broyden-Fletcher-Goldfarb-Shanno), which requires an analytical expression of the gradient in input. The gradient has been computed with Mathematica and translated in C++. Note that GSL minimization algorithms are wrapped in ROOT classes.

It is clear that the response function could be different for each detector. I will fit a single detector at time (which means one detector for CPU thread).

6.10   The dataset

I have applied my procedure to 4 calibrations taken on Sept 27th, Oct 11th, Oct 25th and Nov 11th 2012. The configuration of the detectors was the same, except for the change of the High Voltage of one of the detectors in the last calibration (Tab. 6.1).

During a calibration, each source is placed in three different positions. In these calibrations, the configuration of the positions of the calibration sources is the same (Tab. 6.2), but not the time dedicated to each configuration.

```
Detector  |    HV    |  Position
    ANG2  |  3500V   |  D2 - Middle
    ANG3  |  3500V   |  D4 - Top
    ANG4  |  3500V   |  D3 - Middle
    ANG5  |  2500V   |  D4 - Middle
     RG1  |  4500V   |  D3 - Top
     RG2  |  4000V * |  D3 - Bottom
  GTF112  |  3000V   |  D2 - Top
   GD32B  |  3500V   |  D1 - First
   GD32C  |  3500V   |  D2 - Second
   GD32D  |  3500V   |  D3 - Third
   GD35B  |  3500V   |  D4 - Fourth
   GD35C  |  3500V   |  D5 - Fifth
```

Table 6.1: Detectors, high voltages, positions. * = 3500 V starting from Nov, 8th 2012.

```
Position 1 : S1= 5500 mm S2= 5500 mm S3= 5500 mm
Position 2 : S1= 5190 mm S2= 5340 mm S3= 5340 mm
Position 3 : S1= 5070 mm S2= 5150 mm S3= 5150 mm
```

Table 6.2: Calibrations: positions of the sources S1, S2, S3 (Fig. 6.2). The numbers are the distances from their parking positions in the clean room.
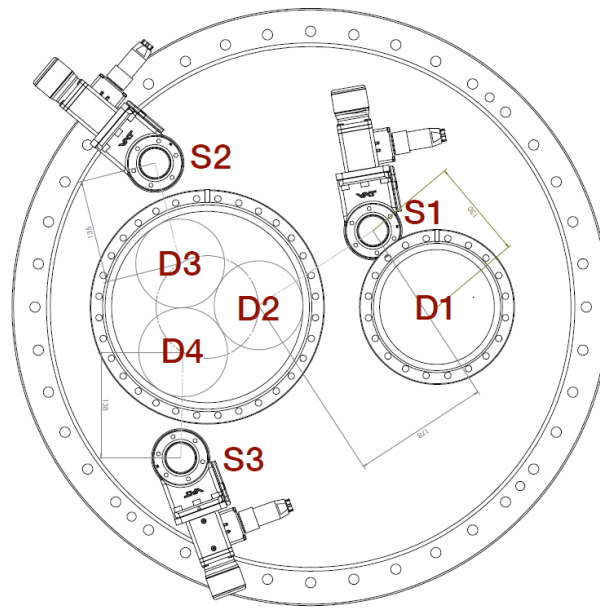
Figure 6.2: Drawing of position of detectors strings and calibration sources. Distances between S1 and D1, S1 and D2, S2 and D3, S3 and D4 are, respectively, 130mm, 308mm, 135mm, 138mm.

6.11   Preliminary baseline scan results

In the tables 6.3 and 6.4, there are the results of my baseline cuts. If the good baselines are more than 68% of the total, then I am probably saving weak pile-up events. It happens sometimes, then I suspect that my baseline cut could be improved.

It is clear that the fraction of saved events for each detector is a function of the calibration source positions. If a source stays very near to a detector more time in a calibration than in another one, the number of pile up events could be very different between calibrations for this detector.

```
20120927  |
Detector  |  Waveforms  |    No P/UO  |      Good baseline  |   Limit
    ANG2  |     148344  |     148175  |    80154    54.09%   |  1792.2
    ANG3  |     113164  |     113032  |    54996    48.66%   |  2017.2
    ANG4  |      98551  |      98419  |    58076    59.01%   |  1327.8
    ANG5  |     135124  |     134992  |    83564    61.90%   |  1849.7
     RG1  |      55796  |      55664  |    35483    63.74%   |  1275.0
     RG2  |     100141  |     100009  |    62961    62.96%   |  1487.4
  GTF112  |     109102  |     108970  |    63064    57.87%   |  1177.0
   GD32B  |      44341  |      44209  |    33287    75.29%   |   452.1
   GD32C  |      52402  |      52270  |    42094    80.53%   |   496.0
   GD32D  |      34493  |      34361  |    25173    73.26%   |   611.3
   GD35B  |      26147  |      25985  |    17159    66.03%   |   635.7
   GD35C  |      37291  |      37158  |    27357    73.62%   |   687.3

20121011  |
Detector  |  Waveforms  |    No P/UO  |      Good baseline  |   Limit
    ANG2  |     242628  |     242423  |   122341    50.47%   |  1786.8
    ANG3  |     187544  |     187352  |   107156    57.20%   |  2036.7
    ANG4  |     161307  |     161115  |    99872    61.99%   |  1338.9
    ANG5  |     221109  |     220917  |   138863    62.86%   |  1849.2
     RG1  |      91441  |      91249  |    61315    67.20%   |  1284.4
     RG2  |     150236  |     150044  |    98089    65.37%   |  1482.9
  GTF112  |     179639  |     179446  |   110650    61.66%   |  1190.6
   GD32B  |      73226  |      73034  |    58505    80.11%   |   460.0
   GD32C  |      87709  |      87517  |    70352    80.39%   |   495.7
   GD32D  |      57743  |      57551  |    41369    71.88%   |   602.6
   GD35B  |      38860  |      38635  |    25755    66.66%   |   639.6
   GD35C  |      51048  |      50856  |    40614    79.86%   |   700.6
```

Table 6.3: Baseline analysis for different calibrations. The columns are: detector, total number of waveforms, waveforms without pulser events and overflows/underflows, good waveforms after the baseline cut, fraction of good waveforms, limit on the baseline sample variance.

```
20121025  |
Detector  |   Waveforms  |   No P/UO  |      Good baseline  |   Limit
    ANG2  |      237629  |    237418  |   142188   59.89%  |   1921.5
    ANG3  |      184160  |    183955  |   112693   61.26%  |   2106.5
    ANG4  |      158906  |    158701  |   100573   63.37%  |   1357.0
    ANG5  |      213737  |    213532  |   135019   63.23%  |   1884.8
     RG1  |       89903  |     89698  |    56009   62.44%  |   1297.6
     RG2  |      153613  |    153408  |    98791   64.40%  |   1486.7
  GTF112  |      175795  |    175590  |   106389   60.59%  |   1355.6
   GD32B  |       72820  |     72615  |    58528   80.60%  |    474.6
   GD32C  |       85372  |     85167  |    66417   77.98%  |    512.2
   GD32D  |       54710  |     54505  |    44708   82.03%  |    680.8
   GD35B  |       40565  |     40336  |    23419   58.06%  |    666.7
   GD35C  |       56642  |     56437  |    45930   81.38%  |    774.9

20121114  |
Detector  |   Waveforms  |   No P/UO  |      Good baseline  |   Limit
    ANG2  |      173169  |    172994  |   101039   58.41%  |   1911.8
    ANG3  |      128871  |    128698  |    72136   56.05%  |   2012.9
    ANG4  |      124342  |    124169  |    79591   64.10%  |   1357.0
    ANG5  |      187235  |    187062  |   116745   62.41%  |   1840.3
     RG1  |       62301  |     62128  |    41022   66.03%  |   1297.6
     RG2  |      154337  |    154164  |   105507   68.44%  |   1519.6
  GTF112  |       63640  |     63467  |    44244   69.71%  |   1377.8
   GD32B  |       53444  |     53271  |    42597   79.96%  |    463.4
   GD32C  |       70914  |     70741  |    54299   76.76%  |    505.0
   GD32D  |       56010  |     55837  |    41460   74.25%  |    677.0
   GD35B  |       36275  |     36078  |    23584   65.37%  |    676.0
   GD35C  |       45643  |     45470  |    32721   71.96%  |    781.4
```

Table 6.4: Baseline analysis for different calibrations. The columns are: detector, total number of waveforms, waveforms without pulser events and overflows/underflows, good waveforms after the baseline cut, fraction of good waveforms, limit on the baseline sample variance.

6.12   Model testing results

In the tables 6.6 and 6.7, there are the results of my model testing. Results are very interesting! The ratio of waveforms which are better described by a triangular current model compared to a flat current model is quite constant between calibrations, and very different between the detectors. It is of special interest to compare RG1 and RG2 which have a very similar geometry, but a very different "triangle ratio". The events which are better described by the simple triangular model seems not to have a specific energy, as it is possible to see from Fig. 6.3. In table 6.5, a summary of the results, and the mean "triangle ratio" between calibrations. The triangular model wins against the flat model. These current models are characterized by the same number of parameters, and the triangular model performs better.

```
Detector |                        Triangle % |  Mean
    ANG2 |  49.38%  49.10%  49.65%  50.11% |  49.56% +-   0.43%
    ANG3 |  95.02%  95.24%  95.29%  95.39% |  95.23% +-   0.16%
    ANG4 |  82.41%  82.32%  82.29%  82.43% |  82.36% +-   0.07%
    ANG5 |  88.93%  88.92%  89.13%  89.04% |  89.00% +-   0.10%
     RG1 |  83.98%  85.71%  83.74%  83.85% |  84.32% +-   0.93%
     RG2 |  59.10%  59.12%  59.21%  58.36% |  58.95% +-   0.39%
  GTF112 |  57.05%  56.96%  57.76%  57.59% |  57.34% +-   0.40%
   GD32B |  75.99%  78.34%  77.35%  78.79% |  77.62% +-   1.24%
   GD32C |  75.93%  75.89%  76.62%  79.26% |  76.92% +-   1.59%
   GD32D |  66.56%  66.73%  66.91%  67.38% |  66.90% +-   0.35%
   GD35B |  87.99%  87.83%  87.55%  87.91% |  87.82% +-   0.19%
   GD35C |  74.06%  72.97%  73.32%  75.83% |  74.04% +-   1.27%
```

Table 6.5: Triangular model summary. The columns are: detector, percentage of triangular current fits with a best χ^2 compared to the flat current fits for each calibration, mean between the values.

```
20120927  |           |         Best model        |
Detector  | Waveforms |     Flat      Triangle     | Triangle %
    ANG2  |     80154 |    40571         39583     |    49.38%
    ANG3  |     54996 |     2741         52255     |    95.02%
    ANG4  |     58076 |    10216         47860     |    82.41%
    ANG5  |     83564 |     9249         74315     |    88.93%
     RG1  |     35483 |     5684         29799     |    83.98%
     RG2  |     62961 |    25751         37210     |    59.10%
  GTF112  |     63064 |    27089         35975     |    57.05%
   GD32B  |     33287 |     7992         25295     |    75.99%
   GD32C  |     42094 |    10133         31961     |    75.93%
   GD32D  |     25173 |     8417         16756     |    66.56%
   GD35B  |     17159 |     2060         15099     |    87.99%
   GD35C  |     27357 |     7096         20261     |    74.06%

20121011  |           |         Best model        |
Detector  | Waveforms |     Flat      Triangle     | Triangle %
    ANG2  |    122341 |    62269         60072     |    49.10%
    ANG3  |    107156 |     5098        102058     |    95.24%
    ANG4  |     99872 |    17657         82215     |    82.32%
    ANG5  |    138863 |    15391        123472     |    88.92%
     RG1  |     61315 |     8761         52554     |    85.71%
     RG2  |     98089 |    40096         57993     |    59.12%
  GTF112  |    110650 |    47624         63026     |    56.96%
   GD32B  |     58505 |    12673         45832     |    78.34%
   GD32C  |     70352 |    16964         53388     |    75.89%
   GD32D  |     41369 |    13763         27606     |    66.73%
   GD35B  |     25755 |     3135         22620     |    87.83%
   GD35C  |     40614 |    10979         29635     |    72.97%
```

Table 6.6: Model comparison for different calibrations. The columns are: good baseline waveforms, waveforms best fitted by the flat current model, waveforms best fitted by the triangular current model, percentage of triangular best fits.

```
20121025   |               |         Best model       |
Detector   | Waveforms     |     Flat       Triangle   | Triangle %
    ANG2   |    142188     |    71591          70597   |    49.65%
    ANG3   |    112693     |     5313         107380   |    95.29%
    ANG4   |    100573     |    17810          82763   |    82.29%
    ANG5   |    135019     |    14673         120346   |    89.13%
     RG1   |     56009     |     9107          46902   |    83.74%
     RG2   |     98791     |    40301          58490   |    59.21%
  GTF112   |    106389     |    44939          61450   |    57.76%
   GD32B   |     58528     |    13258          45270   |    77.35%
   GD32C   |     66417     |    15526          50891   |    76.62%
   GD32D   |     44708     |    14793          29915   |    66.91%
   GD35B   |     23419     |     2916          20503   |    87.55%
   GD35C   |     45930     |    12255          33675   |    73.32%

20121114   |               |         Best model       |
Detector   | Waveforms     |     Flat       Triangle   | Triangle %
    ANG2   |    101039     |    50411          50628   |    50.11%
    ANG3   |     72136     |     3326          68810   |    95.39%
    ANG4   |     79591     |    13987          65604   |    82.43%
    ANG5   |    116745     |    12799         103946   |    89.04%
     RG1   |     41022     |     6625          34397   |    83.85%
     RG2   |    105507     |    43931          61576   |    58.36%
  GTF112   |     44244     |    18764          25480   |    57.59%
   GD32B   |     42597     |     9033          33564   |    78.79%
   GD32C   |     54299     |    11262          43037   |    79.26%
   GD32D   |     41460     |    13525          27935   |    67.38%
   GD35B   |     23584     |     2851          20733   |    87.91%
   GD35C   |     32721     |     7910          24811   |    75.83%
```

Table 6.7: Model comparison for different calibrations. The columns are: good baseline waveforms, waveforms best fitted by the flat current model, waveforms best fitted by the triangular current model, percentage of triangular best fits.
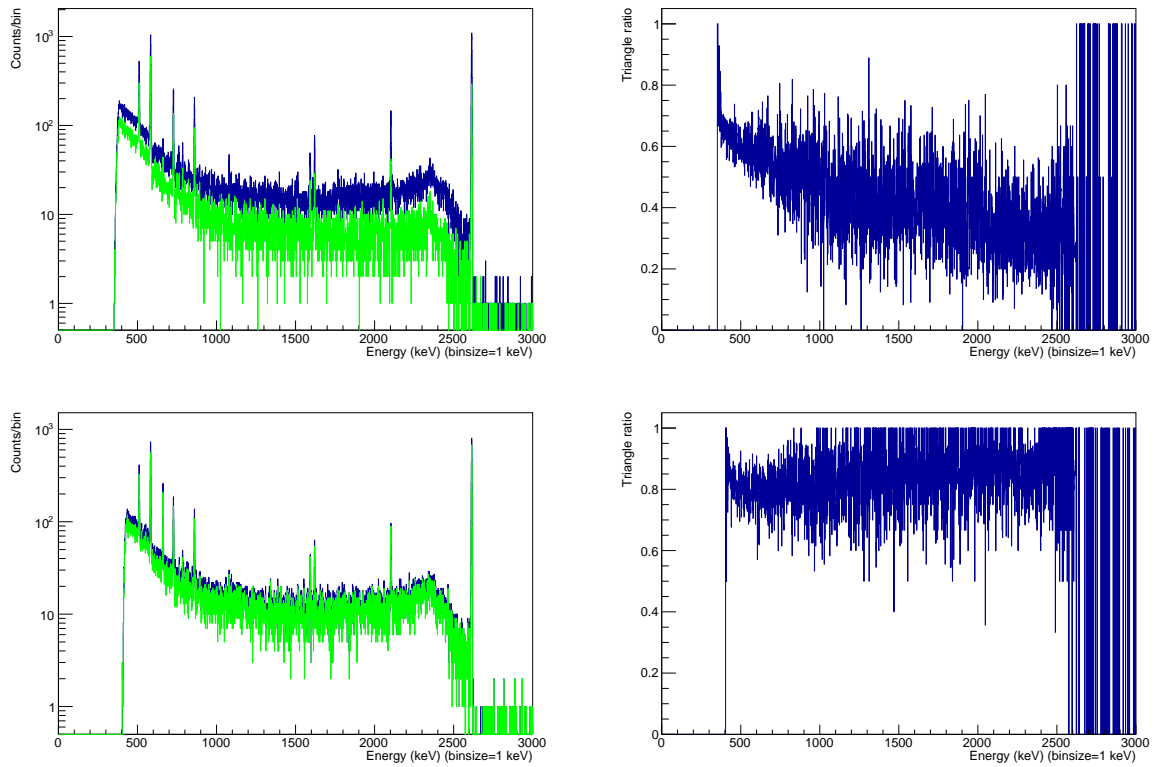
Figure 6.3: On the left: in blue: energy of selected events after the baseline cut, in green: energy of selected events best described by the triangle model after the baseline cut. On the right: ratio triangle/total. On the top: ANG2, on the bottom: ANG4. Calibration of 20120927. The behaviour of these plots is very different between the two detectors.

6.13   Preliminary quality scan results

Now I will consider the data from the triangular model fits.

In the tables 6.8 and 6.9, there are the results of my quality cuts. In this case, good waveforms are sometimes less than 50% of the total, then probably my cut is too strict. In Fig. 6.4, a few distributions are given, which result from the quality scan.
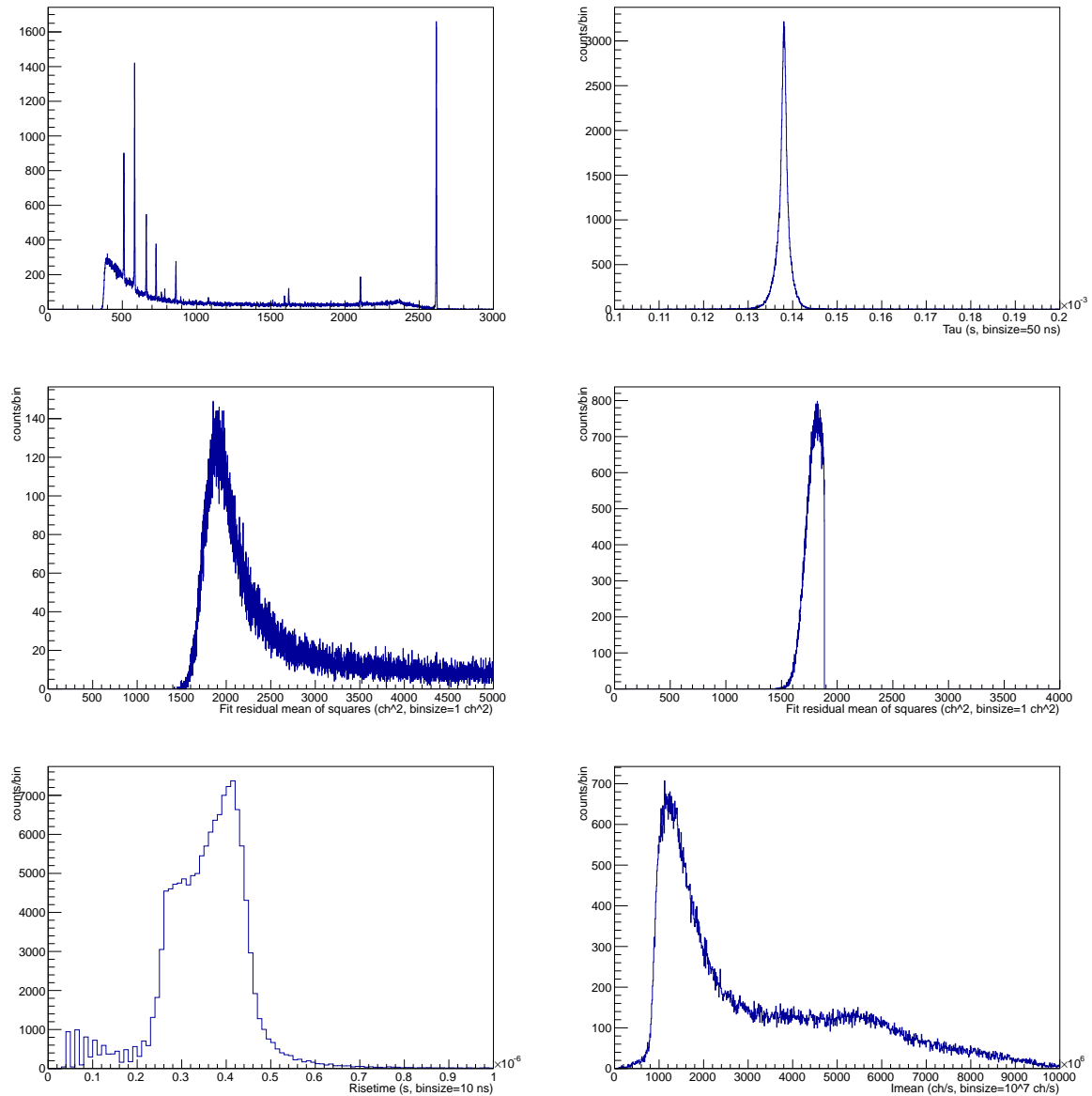
Figure 6.4: ANG4 - 20121025 - Plots from the basic quality scan: energy distribution, time constant, fit quality (sample mean of the squared residuals), baseline quality (sample variance, note the cut), risetime and mean current.

```
20120927
Detector  | Waveforms |    Valid  Fraction |    Valid        SV
    ANG2  |     80154 |    17571   21.92%  |     8192    1496.9
    ANG3  |     54996 |    13355   24.28%  |     8192    1917.4
    ANG4  |     58076 |     9818   16.91%  |     8192    1184.7
    ANG5  |     83564 |     9870   11.81%  |     8192    1717.6
     RG1  |     35483 |     7663   21.60%  |     7663    1183.5
     RG2  |     62961 |    12631   20.06%  |     8192    1224.6
  GTF112  |     63064 |    11225   17.80%  |     8192    1097.5
   GD32B  |     33287 |     4650   13.97%  |     4650     572.4
   GD32C  |     42094 |     5999   14.25%  |     5999     720.0
   GD32D  |     25173 |     5973   23.73%  |     5973     655.0
   GD35B  |     17159 |     3013   17.56%  |     3013     807.8
   GD35C  |     27357 |     3824   13.98%  |     3824     790.6

20121011
Detector  | Waveforms |    Valid  Fraction |    Valid        SV
    ANG2  |    122341 |    24306   19.87%  |     8192    1486.9
    ANG3  |    107156 |    21072   19.66%  |     8192    1865.1
    ANG4  |     99872 |    20405   20.43%  |     8192    1166.2
    ANG5  |    138863 |    21117   15.21%  |     8192    1691.0
     RG1  |     61315 |    11701   19.08%  |     8192    1152.6
     RG2  |     98089 |    18093   18.45%  |     8192    1213.6
  GTF112  |    110650 |    19538   17.66%  |     8192    1071.6
   GD32B  |     58505 |     7492   12.81%  |     7492     569.9
   GD32C  |     70352 |    11111   15.79%  |     8192     698.7
   GD32D  |     41369 |     8285   20.03%  |     8192     643.2
   GD35B  |     25755 |     2918   11.33%  |     2918     773.2
   GD35C  |     40614 |     6041   14.87%  |     6041     798.2
```

Table 6.8: Quality scan for different calibrations. The columns are: detector, good baseline waveforms, waveforms which survive the quality cut, fraction of the total, waveforms considered in the final fits, sample mean of the squared fit residuals.

```
20121025
Detector  |  Waveforms  |     Valid  Fraction |      Valid        SV
    ANG2  |    142188   |     28771    20.23% |       8192    1560.0
    ANG3  |    112693   |     18216    16.16% |       8192    1912.7
    ANG4  |    100573   |     24574    24.43% |       8192    1180.4
    ANG5  |    135019   |     21668    16.05% |       8192    1724.1
     RG1  |     56009   |     10060    17.96% |       8192    1176.4
     RG2  |     98791   |     20212    20.46% |       8192    1229.7
  GTF112  |    106389   |     18168    17.08% |       8192    1191.4
   GD32B  |     58528   |      8385    14.33% |       8192     588.0
   GD32C  |     66417   |      8295    12.49% |       8192     725.5
   GD32D  |     44708   |      7404    16.56% |       7404     689.1
   GD35B  |     23419   |      2605    11.12% |       2605     803.0
   GD35C  |     45930   |      8477    18.46% |       8192     867.0

20121114
Detector  |  Waveforms  |     Valid  Fraction |      Valid        SV
    ANG2  |    101039   |     20849    20.63% |       8192    1734.1
    ANG3  |     72136   |      8419    11.67% |       8192    1905.3
    ANG4  |     79591   |     15694    19.72% |       8192    1224.5
    ANG5  |    116745   |     18977    16.26% |       8192    1700.2
     RG1  |     41022   |      8253    20.12% |       8192    1210.9
     RG2  |    105507   |     19933    18.89% |       8192    1348.4
  GTF112  |     44244   |      7321    16.55% |       7321    1268.2
   GD32B  |     42597   |      4345    10.20% |       4345     428.3
   GD32C  |     54299   |      8739    16.09% |       8192     468.6
   GD32D  |     41460   |      8970    21.64% |       8192     619.7
   GD35B  |     23584   |      4252    18.03% |       4252     623.6
   GD35C  |     32721   |      6461    19.75% |       6461     728.6
```

Table 6.9: Quality scan for different calibrations. The columns are: detector, good baseline waveforms, waveforms which survive the quality cut, fraction of the total, waveforms considered in the final fits, sample mean of the squared fit residuals.

6.14 GERDA response reconstruction results

In the tables 6.11 and 6.12, there are the results of my big fits to estimate the parameters for the response functions for each channel.

Note that the mean of the squared samples residuals of the fit of the complex response model fit is always lower compared to the simple response model fit, and that the parameters in the complex fit are very similar between the calibrations. A summary of the results in the next table

```
             |      Simple resp    |  Complex resp
  Detector   |      tau            |  taushort              taulong
      ANG2   |  153.749 +-  0.019  |   114.020 +-  0.256  ;  219.150 +-   0.457
      ANG3   |  142.685 +-  0.047  |   104.192 +-  1.433  ;  206.408 +-   3.690
      ANG4   |  167.390 +-  0.062  |   106.854 +-  0.851  ;  303.735 +-   4.330
      ANG5   |  137.382 +-  0.051  |    80.150 +-  0.811  ;  280.948 +-   5.176
       RG1   |  149.244 +-  0.035  |    98.041 +-  0.360  ;  253.688 +-   1.727
       RG2   |  167.186 +-  0.085  |   124.391 +-  0.205  ;  238.135 +-   0.308
    GTF112   |  153.881 +-  0.012  |    94.076 +-  1.210  ;  297.241 +-   6.361
     GD32B   |  155.938 +-  0.028  |    96.665 +-  4.367  ;  295.098 +- 24.512
     GD32C   |  131.830 +-  0.055  |    75.891 +-  0.794  ;  271.776 +-   4.809
     GD32D   |  154.740 +-  0.359  |    96.771 +-  1.478  ;  287.289 +-   9.552
     GD35B   |  145.586 +-  0.208  |    81.116 +-  2.857  ;  328.670 +- 21.409
     GD35C   |  147.486 +-  0.015  |    86.767 +-  1.798  ;  302.137 +- 11.015
```

Table 6.10: Response reconstruction fit results - Summary table. The columns are: detector, tau for the simple response model, taushort and taulong for the complex response model.

What is the best model? It is possible to evaluate the AIC index [3] [4]

$$\text{AIC} = -\ln[\mathcal{L}] + 2k$$

where $\mathcal{L}$ is the likelihood, and k is the number of the parameters in the fit. The likelihood is a function of the noise variance, which is not known (but it is $\leq$ than the baseline sample variance). The best model minimizes the AIC index, then the complex response is the best one if

$$\sum_n \frac{SV_2}{\sigma^2} + 2 < \sum_n \frac{SV_1}{\sigma^2} \implies \sigma^2 < \frac{n(SV_1 - SV_2)}{2}$$

where σ^2 is the noise variance, n is the number of fitted samples, SV_1 is the sample mean of the squared residuals in the basic response fit and SV_2 is the sample mean of the squared residuals in the complex response fit.

For example, considering the ANG2 response models obtained from the calibration of 20120927, the complex response is a better description from a statistical point of view if

$$\sigma^2 < \frac{20283398(1556.8 - 1542.8)}{2} \sim 1.41 \times 10^8.$$

Note that σ^2 is expected to be lower than the baseline sample variance, which is cut at 1792.2.

6.15   Conclusions

It is important to note that I have obtained very solid results, in the sense that they are really similar between the calibrations.

The shape of the tail of GERDA waveforms is not fully described with the simple single-tau response functions. I can say this because the results from the two-parameters fit is always better, and it is compatible between different calibrations.

It is important to note that, if the complex model of the response is right, to obtain a τ for the simple response model by looking only at the final part of the tails will probably over-estimate the optimal value. I will apply my result to the energy reconstruction and to the current reconstruction for pulse shape discrimination in the next chapter.

Bibliography

[1] Valentin T. Jordanov and Glenn F. Knoll, *Digital synthesis of pulse shapes in real time for high resolution radiation spectroscopy* (1994).

[2] M. Galassi et al., *GNU Scientific Library Reference Manual - Third Edition*, 2009.

[3] Akaike H., *A new look at the statistical model identification*, IEEE Transactions on Automatic Control 19 (6): 716–723.

[4] Kenneth P. Burnham and David R. Anderson, *Model selection and multimodel inference*: *A pratical information - Theoretic approach*, 2002.

```
20120927  |       Simple resp  |   Complex resp
Detector  |     tau        SV  | taushort   taulong       SV  |    Samples    NV limit
    ANG2  | 153.750     1556.8  | 114.092   219.128   1542.8  |   20283392    1.414e+08
    ANG3  | 142.738     1949.9  | 105.847   202.147   1936.2  |   20283392    1.385e+08
    ANG4  | 167.429     1217.5  | 106.538   305.450   1178.4  |   20283392    3.964e+08
    ANG5  | 137.441     1750.1  |  79.261   286.729   1627.8  |   20283392    1.240e+09
     RG1  | 149.269     1207.6  |  97.727   254.967   1169.5  |   18973588    3.616e+08
     RG2  | 167.122     1257.3  | 124.202   238.249   1248.2  |   20283392    9.199e+07
  GTF112  | 153.892     1128.6  |  94.167   297.241   1061.2  |   20283392    6.829e+08
   GD32B  | 155.952      583.6  |  93.669   312.550    514.8  |   11513400    3.960e+08
   GD32C  | 131.792      730.6  |  75.583   272.515    592.4  |   14853524    1.026e+09
   GD32D  | 155.151      669.7  |  95.083   298.204    630.4  |   14789148    2.908e+08
   GD35B  | 145.824      854.5  |  82.358   319.417    721.0  |    7460188    4.980e+08
   GD35C  | 147.482      803.9  |  84.979   312.861    725.7  |    9468224    3.702e+08


20121011  |       Simple resp  |   Complex resp
Detector  |     tau        SV  | taushort   taulong       SV  |    Samples    NV limit
    ANG2  | 153.730     1552.3  | 114.232   218.704   1539.5  |   20283392    1.300e+08
    ANG3  | 142.648     1897.8  | 103.336   208.583   1886.1  |   20283392    1.186e+08
    ANG4  | 167.318     1198.4  | 107.818   298.811   1164.2  |   20283392    3.470e+08
    ANG5  | 137.354     1724.9  |  80.849   276.742   1611.0  |   20283392    1.156e+09
     RG1  | 149.204     1177.0  |  98.434   251.723   1146.1  |   20283392    3.140e+08
     RG2  | 167.154     1246.0  | 124.609   237.786   1238.3  |   20283392    7.800e+07
  GTF112  | 153.882     1101.7  |  92.823   303.602   1043.7  |   20283392    5.874e+08
   GD32B  | 155.906      582.5  | 101.675   267.075    529.0  |   18550192    4.960e+08
   GD32C  | 131.893      709.9  |  76.793   266.640    581.4  |   20283392    1.303e+09
   GD32D  | 154.491      657.1  |  97.835   280.460    614.3  |   20283392    4.337e+08
   GD35B  | 145.492      822.1  |  83.143   313.444    702.6  |    7224968    4.318e+08
   GD35C  | 147.502      813.1  |  88.574   290.853    736.2  |   14957516    5.754e+08
```

Table 6.11: Response reconstruction fit results for different calibrations. The columns are: detector; tau and sample mean of the squared fit residuals for the simple model response; taushort, taulong and sample mean of the squared fit residuals for the complex model response; noise variance limit. The complex model is a best fit if the "real" noise variance is lower than the noise variance limit.

```
20121025  |        Simple resp  |    Complex resp
Detector  |      tau       SV  | taushort   taulong       SV  |    Samples     NV limit
    ANG2  |  153.768   1620.2  |  113.736   219.617   1606.0  |  20283392    1.438e+08
    ANG3  |  142.669   1943.1  |  103.393   208.493   1931.8  |  20283392    1.141e+08
    ANG4  |  167.422   1210.2  |  106.205   306.945   1175.1  |  20283392    3.560e+08
    ANG5  |  137.351   1755.4  |   80.341   279.373   1639.2  |  20283392    1.179e+09
     RG1  |  149.258   1198.3  |   97.963   254.373   1165.9  |  20283392    3.279e+08
     RG2  |  167.282   1259.1  |  124.363   238.370   1250.1  |  20283392    9.207e+07
  GTF112  |  153.869   1219.4  |   95.237   290.881   1153.5  |  20283392    6.683e+08
   GD32B  |  155.956    599.8  |   94.651   305.670    532.1  |  20283392    6.874e+08
   GD32C  |  131.806    734.7  |   75.296   276.172    600.8  |  20283392    1.358e+09
   GD32D  |  154.578    702.1  |   97.395   283.203    660.4  |  18332304    3.816e+08
   GD35B  |  145.442    850.5  |   77.849   353.150    729.4  |   6449980    3.904e+08
   GD35C  |  147.473    880.4  |   86.747   302.696    797.0  |  20283392    8.459e+08

20121114  |        Simple resp  |    Complex resp
Detector  |      tau       SV  | taushort   taulong       SV  |    Samples     NV limit
    ANG2  |  153.781   1630.9  |  114.018   219.261   1616.5  |  20283392    1.459e+08
    ANG3  |  142.704   1910.0  |  103.180   209.333   1896.7  |  20283392    1.349e+08
    ANG4  |  167.368   1209.7  |  106.898   302.530   1172.6  |  20283392    3.763e+08
    ANG5  |  137.378   1722.8  |   79.876   282.384   1606.7  |  20283392    1.178e+09
     RG1  |  149.251   1206.2  |   96.492   260.408   1169.4  |  20283392    3.732e+08
     RG2  |  167.608   1262.0  |  124.979   237.860   1254.5  |  20283392    7.575e+07
  GTF112  |  153.959   1273.8  |   91.924   310.035   1194.8  |  18126796    7.160e+08
   GD32B  |  155.867    578.2  |   96.735   292.850    514.4  |  10758220    3.431e+08
   GD32C  |  131.851    747.3  |   76.153   271.692    610.7  |  20283392    1.385e+09
   GD32D  |  154.649    709.0  |   98.182   279.496    665.9  |  20283392    4.372e+08
   GD35B  |  145.607    884.8  |   81.029   329.688    750.1  |  10527952    7.092e+08
   GD35C  |  147.512    832.3  |   93.069   267.173    794.8  |  15997436    2.998e+08
```

Table 6.12: Response reconstruction fit results for different calibrations. The columns are: detector; tau and sample mean of the squared fit residuals for the simple model response; taushort, taulong and sample mean of the squared fit residuals for the complex model response; noise variance limit. The complex model is a best fit if the "real" noise variance is lower than the noise variance limit.

Chapter 7

Response function application

Introduction

In this section I will apply the results obtained in the modelization of the response function for each detector to the energy reconstruction, to evaluate resolution improvements, and to the current reconstruction, to evaluate pulse shape discrimination improvements. I will focus on the first three calibrations of the previous chapter: Sept 27th, Oct 11th and Oct 25th.

7.1   Energy reconstruction with a single τ

For the simple model of the response function I have reconstructed the energies in the default GERDA way. I have simply used my τ estimates in the analysis. So, the steps are: baseline restoration, moving window deconvolution, moving window averages.
I have considered two different approaches:

- 1: The τ estimated from the simple-response fit, which is the best one to describe the response in the range 0-80 μs (half signal window).

- 2: An effective tau estimated from the complex-response fit. In the limit for $t \to 0$, the complex response reduces to

$$R_2 = \frac{1}{2}\Big(\exp\Big[-\frac{t}{\tau_s}\Big] + \exp\Big[-\frac{t}{\tau_l}\Big]\Big) \overset{t \to 0}{\sim} 1 + \Big(-\frac{1}{2\tau_s} - \frac{1}{2\tau_l}\Big)t.$$

  Instead the simple response becomes

$$R_1 = \exp\Big[-\frac{t}{\tau}\Big] \overset{t \to 0}{\sim} 1 + \Big(-\frac{1}{\tau}\Big)t.$$

  Then, the best τ in the limit for $t \to 0$ is

$$\tau = 2\frac{\tau_s \tau_l}{\tau_s + \tau_l}.$$

According to a fast analysis, there is not a big difference between the two approaches, and then I will report only the results for the first one.

7.2   Sloped current model with a complex response

Now it is time to move to a complex model for the current. The idea is to model the current as a piecewise polynomial of order 1. The model parameters are the current values at the connection points between the pieces. So the model is a continuos function, differentiable everywhere except at the connection points.

To focus, we can start by considering a single piece, between the times t_l and t_r (left and right). It is a sloped current

$$I[t] = \begin{cases} 0 & (t < t_l) || (t > t_r) \\ \frac{(-t_r i_l + t_l i_r + (i_l - i_r)t)}{t_l - t_r} & (t_l < t) \&\& (t < t_r) \end{cases} \tag{7.1}$$

t_l is the start time, t_r is the end time, i_l is the intensity at the start time, i_r is the intensity at the end time.

Note that

$$\int_{-\infty}^{\infty} I[t']dt' = \frac{1}{2}(i_l + i_r)(t_r - t_l).$$

The convolution of the sloped model current with the complex exponential response is given by

$$Q[t] = \int_{-\infty}^{t} I[t']R[t - t']dt'$$

and to obtain the sampled version you need to use (6.1).

7.3   Current reconstruction

Now we want to reconstruct the current related to a sampled signal. We can sample the current in our favourite way. Usually, in a given time region, the current sampling rate has to be proportional to the signal sampling rate. As explained, my current model is a piecewise polynomial, and each piece is described in way like (7.1). It is possible to relate signal samples and current samples by a matrix equation

$$q = Mi.$$

To obtain the current by using a least square approach, which permits to manage a dishomogeneous sampling of the signal, as we have in calibration mode, we need to minimize

$$f = \frac{1}{2}(q - Mi)^T N^{-1}(q - Mi). \tag{7.2}$$

N^{-1} is a diagonal matrix $n_s \times n_s$, which describes the samples weight. For a sample index a, one can set $N^{-1}[a,a] = 4$ if the sample $q[a]$ relates to a period of 40 ns, and $N^{-1}[a,a] = 1$ if the sample $Q[a]$ relates to a period of 10 ns.

The solution which minimizes (7.2) is given by the linear system

$$(M^T N^{-1} M)i = (M^T N^{-1})q$$

$(M^T N^{-1} M)$ is a positive definite matrix (if the density of current samples is always lower than the density of signal samples). Then, in principle it is possible to invert the system

$$i = (M^T N^{-1} M)^{-1} M^T N^{-1} q$$

but there are fast algorithms which take advantage of a Cholesky decomposition of the matrix. I used the Cholesky solver from the GNU Scientific Library [4]. It it possible to obtain the Cholesky decomposition of $M^T N^{-1} M$ one time at all at the beginning of the analysis, then solve the linear system for each waveform. This way is fast and it provides a better numerical accuracy.

7.4   Energy reconstruction by resampling

In the second energy reconstruction test, I have obtained an high sampling density current for each waveform, and then I have resampled the signal with a homogeneous sampling of 10 ns, so that it is possible to use the standard GELATIO pipeline to evaluate the energy.

7.5   GERDA energy reconstruction results

Obtained the energy, I have applied the standard GERDA routine to evaluate the resolution (Full Width Half Maximum) at the peaks. In Tab. 7.1, the resolution at 2614 keV is presented.

According to the ROOT minimizers, the errors are about 0.02 keV on the resolutions, then all the numbers seem compatible. On the other side, the resolution obtained with a physical time constant (M1 in the table) is better or equal than the resolution obtained with the GELATIO default approach (M0 in the table) in 27/36 cases. In the hypothesis of random fluctuations of $M0$ and $M1$ around the same value, the expected ratio is 18/36. The probability to have a more extreme result ($>=28/36$ or $<=8/36$) is only 0.1%.

The resolution obtained with the resampling approach (M2 in the table) is better or equal than the M0 resolution in 23/36 cases, but improvements are usually larger than M1. The probability to have a more extreme result ($>=24/36$ or $<=12/36$) is 6%.

Moreover, bad performances of my approaches for GD35B are probably due to the low

statistics.

So, results are promising, especially because I think that there is a wide margin for improvements (for example: to change the sampling pattern of the current in the current reconstruction). For sure, the improvements are not so big, and this validates the approximations in the current default energy reconstruction.

It seems interesting that our worse-resolution detectors are ANG2 and RG2, where the simple triangular model for the current performs in a similar way of the flat model. The resolution of RG1, which is geometrically very similar to RG2, is significantly better.

```
              Detector      M0      M1      M2

                  ANG2   4.847   4.847   4.878
                  ANG3   4.826   4.816   4.766
                  ANG4   4.488   4.488   4.512
                  ANG5   4.449   4.442   4.379
                   RG1   4.708   4.707   4.660
                   RG2   5.038   5.037   5.014
                GTF112   4.472   4.468   4.474
      GD32B (Agamennone)   2.884   2.869   2.872
      GD32C (Andromeda)   2.937   2.936   2.922
         GD32D (Anubis)   3.010   3.014   3.031
       GD35B (Achilles)   3.420   3.432   3.710
    GD35C (Aristoteles)   2.974   2.973   2.961

              Detector      M0      M1      M2

                  ANG2   5.004   5.006   5.054
                  ANG3   4.786   4.782   4.709
                  ANG4   4.586   4.582   4.565
                  ANG5   4.444   4.441   4.425
                   RG1   4.690   4.679   4.643
                   RG2   5.181   5.183   5.141
                GTF112   4.568   4.569   4.573
      GD32B (Agamennone)   2.916   2.914   2.870
      GD32C (Andromeda)   2.963   2.957   2.938
         GD32D (Anubis)   3.045   3.031   3.074
       GD35B (Achilles)   3.734   3.736   3.991
    GD35C (Aristoteles)   3.124   3.103   3.096

              Detector      M0      M1      M2

                  ANG2   4.901   4.904   4.926
                  ANG3   4.822   4.818   4.740
                  ANG4   4.527   4.523   4.502
                  ANG5   4.433   4.431   4.375
                   RG1   4.716   4.709   4.643
                   RG2   5.130   5.128   5.125
                GTF112   4.533   4.537   4.515
      GD32B (Agamennone)   3.034   3.025   3.028
      GD32C (Andromeda)   2.966   2.963   2.996
         GD32D (Anubis)   3.088   3.084   3.054
       GD35B (Achilles)   2.823   2.925   3.051
    GD35C (Aristoteles)   3.066   3.060   3.083
```

Table 7.1: Resolution results (FWHM at 2614 keV) for the three calibrations (20120927, 20121011, 20121025). M0 = Gelatio defaults. M1 = Single tau response. M2 = Resampling approach.
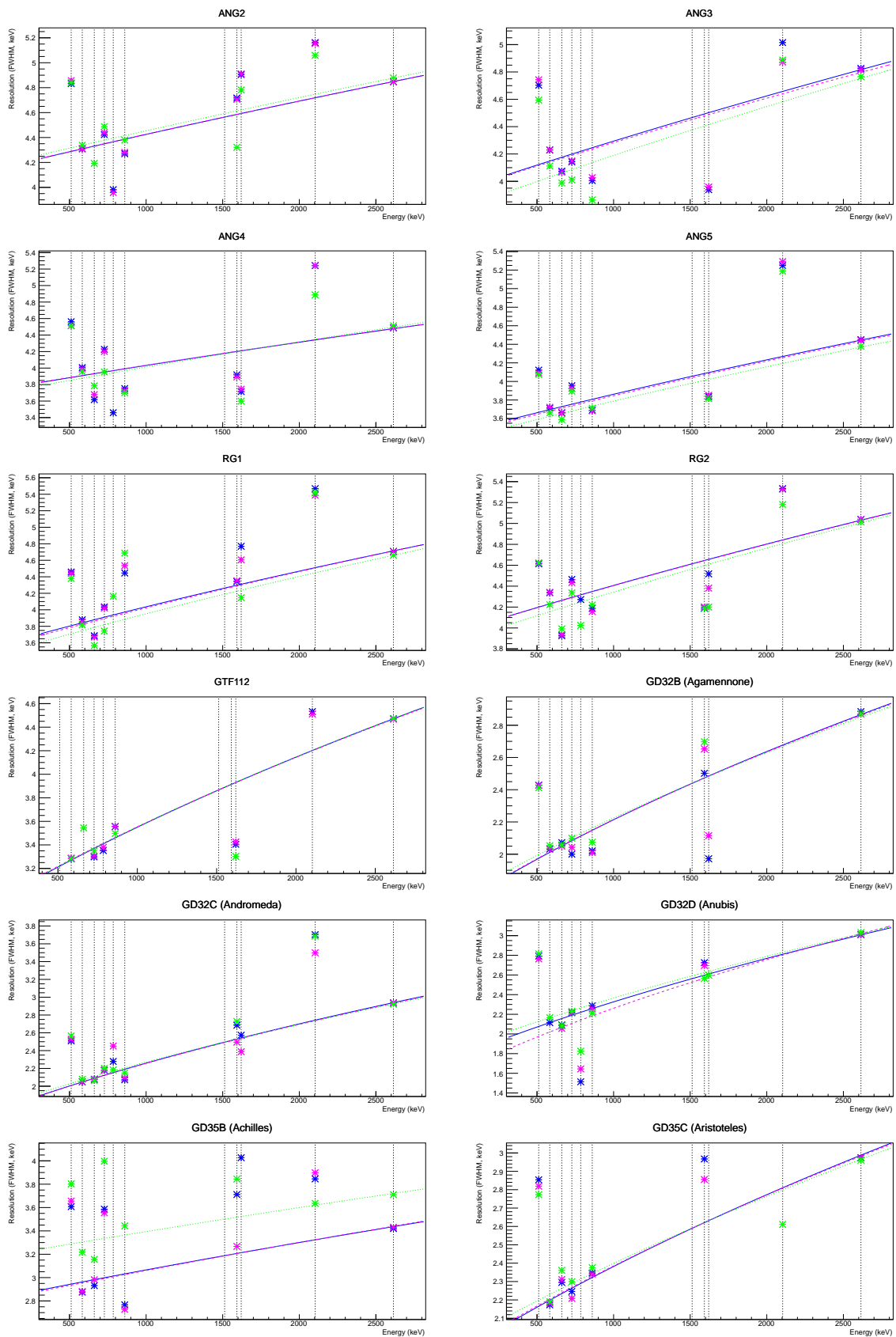
Figure 7.1: Energy resolution - 20120927 calibration. Blue line: M0; Pink line: M1; Green line: M2.
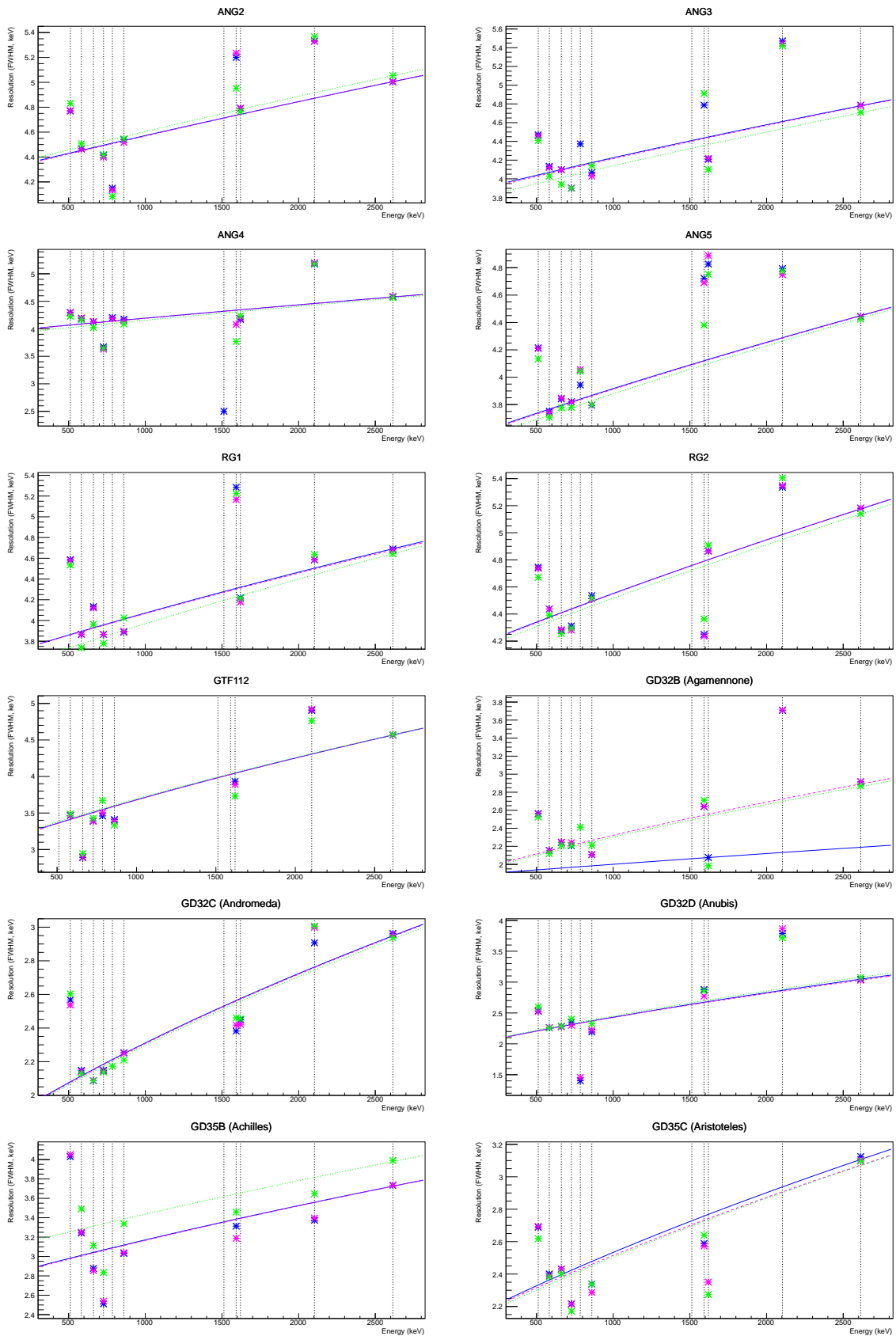
Figure 7.2: Energy resolution - 20121011 calibration. Blue line: M0; Pink line: M1; Green line: M2.
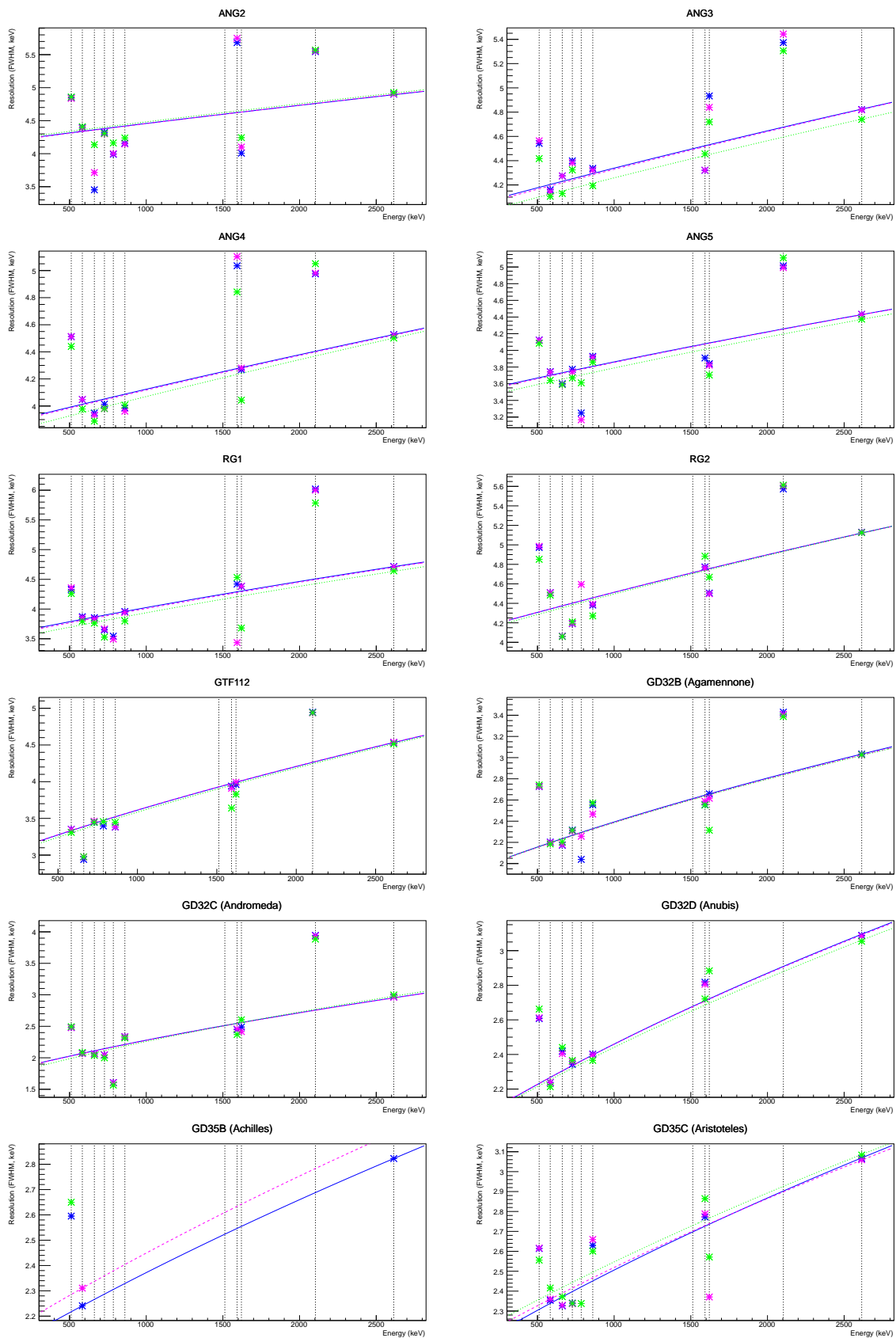
Figure 7.3: Energy resolution - 20121025 calibration. Blue line: M0; Pink line: M1; Green line: M2.

7.6   Current reconstruction for Pulse Shape Analysis

In my current reconstruction for pulse shape analysis, I tried an original approach which allows for simultaneous baseline subtraction. I have sampled the current with high rate in the high rate region of the signal, and forced the current to be zero outside this region. Then I have added the baseline to my linear system, so that I have obtained

$$q = \begin{pmatrix} M & 1 \end{pmatrix} \begin{pmatrix} I \\ b \end{pmatrix} = Kx$$

q is a vector of $n_s = 4396$ components, I a vector of n_c components, then x is a vector of $n_x = n_c + 1$ components and K is a matrix $(n_s \times n_x)$.

As before, I use a least square approach to solve the system, and the algorithms of the GNU Scientific Library [4].

7.7   Pulse shape discrimination

It has been proved that the ratio maximum amplitude (A) over energy (E) A/E is a good parameter for pulse shape discrimination in BEGe detectors [3].

In the double escape peak of the 2614 keV line, which is located at 1592 keV, most of the events are single site, then it is possible to obtain a distribution of A/E for single site events by looking at this peak. The neuronal network in the HdM analysis is a somewhat similar approach.

In the high density 10 ns signal region, I have reconstructed the current with a sampling period of 20 ns (to avoid overfitting). In my tests, I found more convenient the ratio Q_{40} (maximum charge collected in 40 ns: the maximum charge collected in a period of two samples) over Q (total charge) for a set of reasons. It is a dimensionless value; Q_{40} is somewhat the integrated version of A, and this reduced the fluctuations, using Q instead of E avoid a possible non-linearity introduced by the energy reconstruction algorithm.

In my tests I have obtained a very good resolution for Q_{40}/Q, as you can see in Tab. 7.2 and in the summary Tab. 7.3. It is comparable with the resolution on A/E.
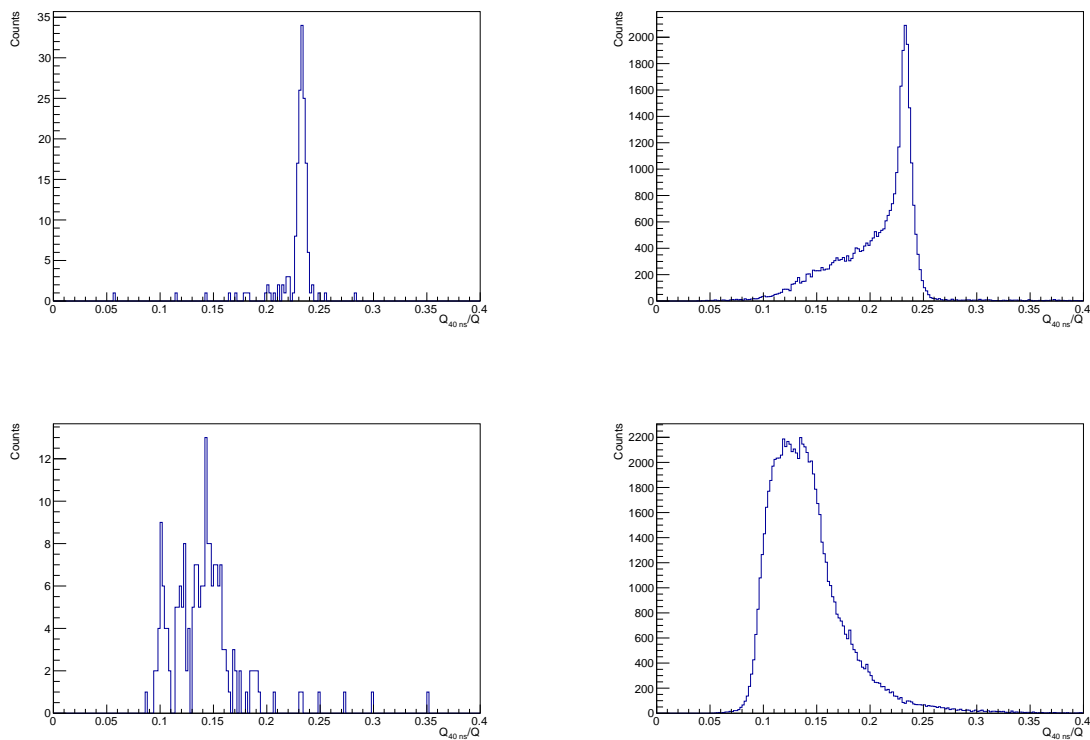
Figure 7.4: Distribution of Q_{40}/Q at the Double Escape Peak (on the left) and at the Full energy peak (on the right) for 2614 keV gammas from ^{208}Tl for GD32B (BEGe detector, first line) and ANG1 (coaxial detector, second line) in the 20120927 calibration. For BEGe detectors, the single site events in the double escape peak have a well-defined A/E or Q_{40}/Q parameter. That is not true for coaxial detectors.

```
      20120927  |                                    |   3-sigma
      Detector  |      Mean      Devst               | low limit
         GD32B  |  0.232977    0.003127  ( 1.342065%) |  0.223596
         GD32C  |  0.238548    0.003405  ( 1.427228%) |  0.228333
         GD32D  |  0.267428    0.003868  ( 1.446253%) |  0.255824
         GD35B  |  0.243049    0.004331  ( 1.781840%) |  0.230056
         GD35C  |  0.247545    0.003316  ( 1.339551%) |  0.237597

      20121011  |
      Detector  |      Mean      Devst
         GD32B  |  0.233196    0.003119  ( 1.337568%) |  0.223839
         GD32C  |  0.239087    0.003241  ( 1.355737%) |  0.229364
         GD32D  |  0.267411    0.003530  ( 1.319924%) |  0.256821
         GD35B  |  0.244394    0.003998  ( 1.635730%) |  0.232400
         GD35C  |  0.249345    0.003120  ( 1.251426%) |  0.239985

      20121025  |
      Detector  |      Mean      Devst
         GD32B  |  0.233211    0.003275  ( 1.404456%) |  0.223386
         GD32C  |  0.239407    0.003413  ( 1.425434%) |  0.229168
         GD32D  |  0.267488    0.003478  ( 1.300387%) |  0.257054
         GD35B  |  0.235861    0.006804  ( 2.884743%) |  0.215449
         GD35C  |  0.248242    0.003434  ( 1.383295%) |  0.237940
```

Table 7.2: Q_{40}/Q results in the double escape peak. The columns are: detector, distribution mean, distribution devst, devst/mean.

```
      Detector  |  20120927   20121011   20121025
         GD32B  |  0.232977   0.233196   0.233211  |  0.233128 +-  0.000131
         GD32C  |  0.238548   0.239087   0.239407  |  0.239014 +-  0.000434
         GD32D  |  0.267428   0.267411   0.267488  |  0.267442 +-  0.000040
         GD35B  |  0.243049   0.244394   0.235861  |  0.241101 +-  0.004588
         GD35C  |  0.247545   0.249345   0.248242  |  0.248377 +-  0.000907
```

Table 7.3: Q_{40}/Q summary, mean of the results of the three calibrations, to check for variabilities.

7.8 Applications

I have reconstructed the current of the signals related to events with an energy between 1839-2239 keV in the period between Sept 27th and Oct 25th. Three events from a total of 12 are located in BEGe detectors. According to my pulse shape analysis, they are multi-site with a confidence level $> 3\sigma$, as shown in Tab. 7.4.
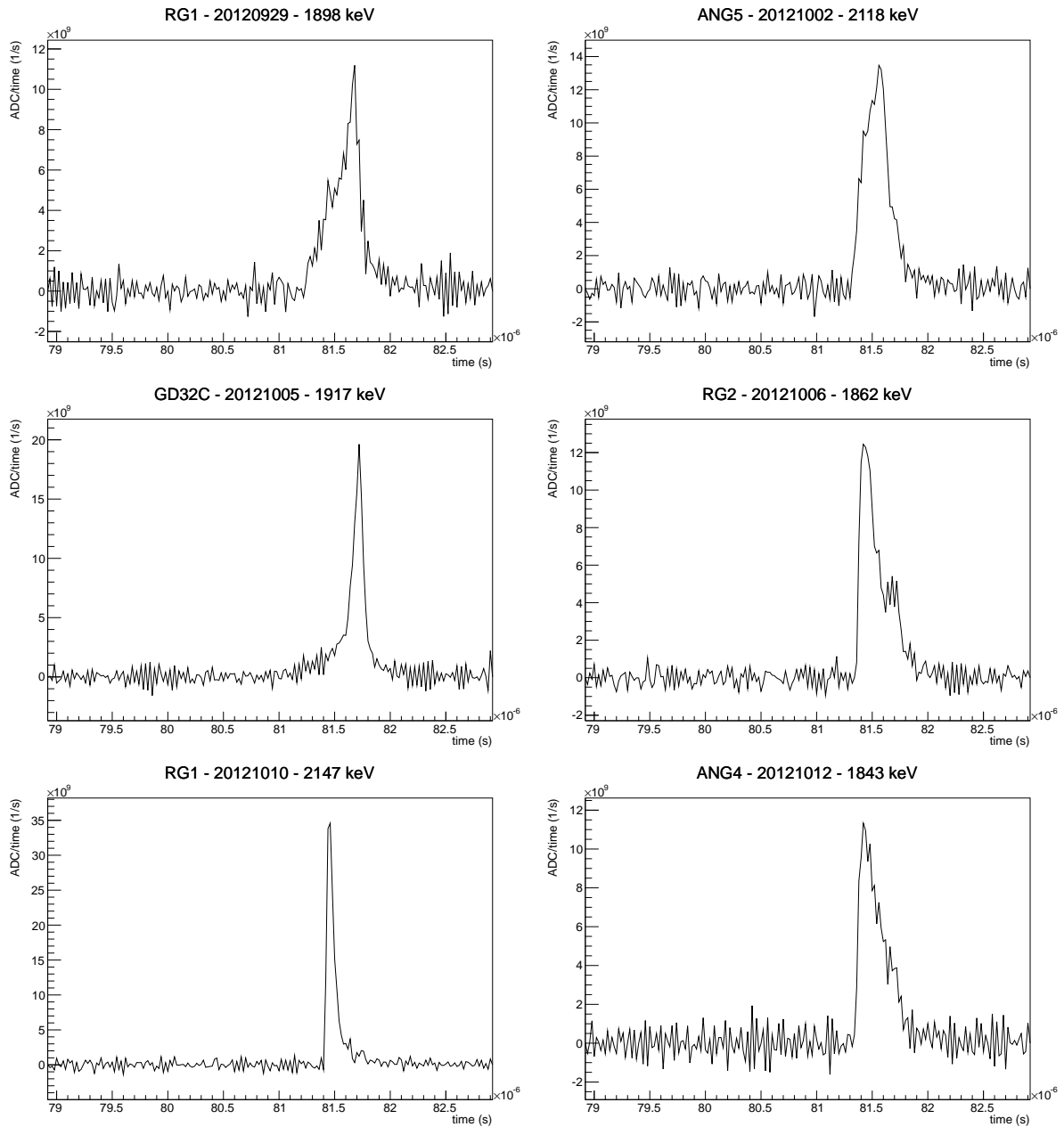
Figure 7.5: Examples of my current reconstruction for the events in the energy window $Q_{\beta\beta} \pm 200$ keV between Sept 27th and Oct 25th, 1/2.
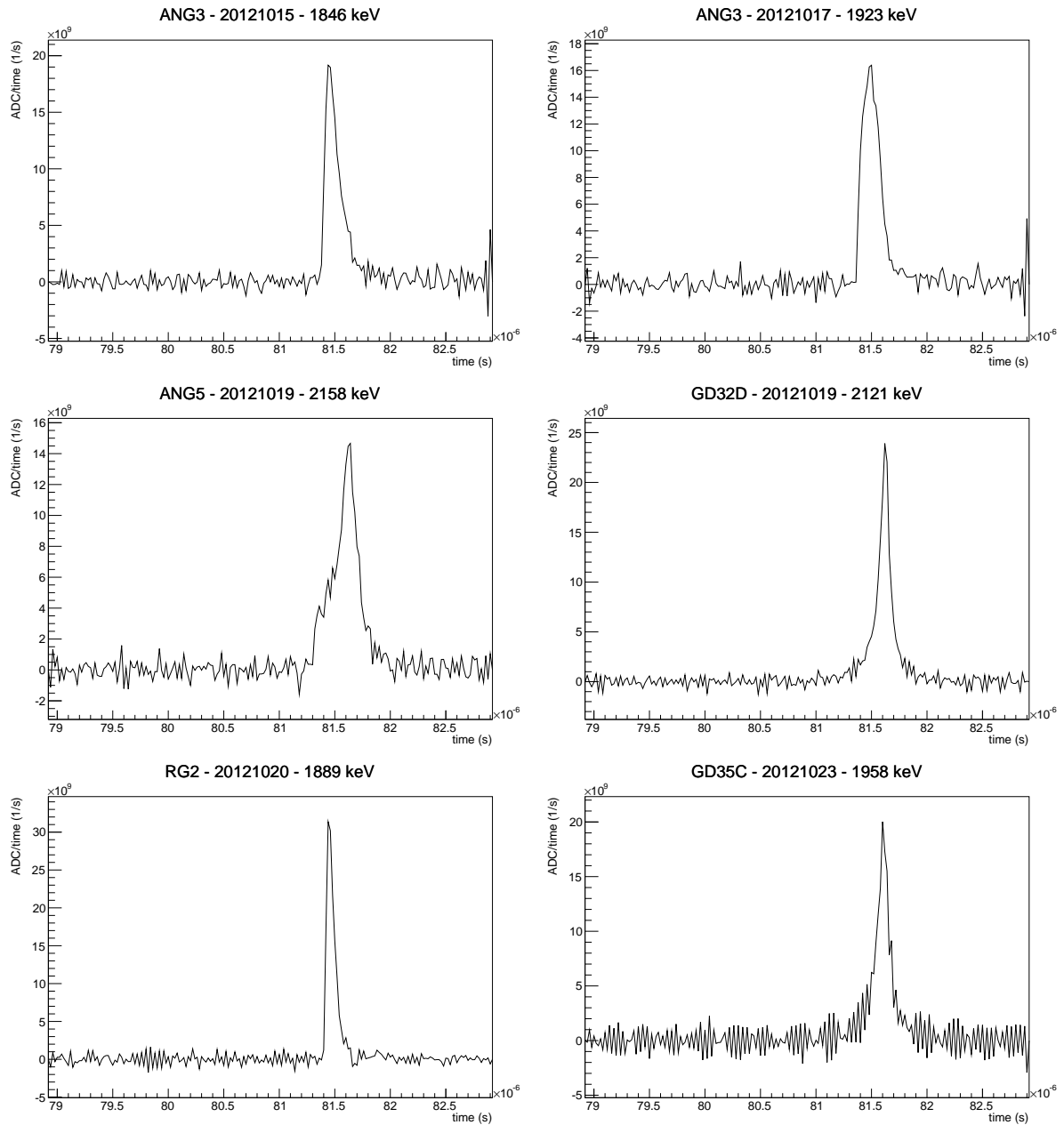
Figure 7.6: Examples of my current reconstruction for the events in the energy window $Q_{\beta\beta} \pm 200$ keV between Sept 27th and Oct 25th, 2/2.

```
    Detector  |       Date  | Energy  |      Q40/Q  | Pulse shape discrimination
         RG1  | 20120929  |   1898  |  0.131809  |
        ANG5  | 20121002  |   2118  |  0.138365  |
       GD32C  | 20121005  |   1917  |  0.218310  | < 0.228333 ---> MULTISITE
         RG2  | 20121006  |   1862  |  0.163800  |
         RG1  | 20121010  |   2147  |  0.370803  |
        ANG4  | 20121012  |   1843  |  0.147881  |
        ANG3  | 20121015  |   1846  |  0.215751  |
        ANG3  | 20121017  |   1923  |  0.179345  |
        ANG5  | 20121019  |   2158  |  0.147964  |
       GD32D  | 20121019  |   2121  |  0.241949  | < 0.256821 ---> MULTISITE
         RG2  | 20121020  |   1889  |  0.374724  |
       GD35C  | 20121023  |   1958  |  0.214606  | < 0.239985 ---> MULTISITE
```

Table 7.4: Events in the region 1839-2239 keV between the first and the last processed calibration. The columns are: detector, date, energy (keV), Q_{40}/Q, PSD.

7.9   Conclusions

Results are interesting. About the energy reconstruction, there are indications of small improvements, but for sure my results are not so different compared to the official analysis. Thus, the GERDA official reconstruction is validated. About the pulse shape discrimination, in the hypothesis that the A/E approach is valid, all the background events in BEGe detectors which I have analyzed (three events) result multi-site. For sure, there is a lot of space for the optimization/tuning (e.g. Q_{40} could be Q_{30} with a current sampled at 15ns) of my procedure. Another planned improvement is to switch from degree-one piecewise polynomial for the current model to a more general spline. It could be interesting, because, at the moment, the current maximum is clearly constrained on a connection point.

Bibliography

[1] Valentin T. Jordanov and Glenn F. Knoll, *Digital synthesis of pulse shapes in real time for high resolution radiation spectroscopy* (1994).

[2] Glenn F. Knoll, *Radiation Detection and Measurement*, 4th, 2010.

[3] Dusan Budjas, Marik Barnabe Heider, Oleg Chkvorets, Nikita Khanbekov, and Stefan Schonert, *Pulse shape discrimination studies with a Broad-Energy Germanium detector for signal identification and background suppression in the GERDA double beta decay experiment*, JINST **4** (2009), P10007, available at `arXiv:0909.4044[nucl-ex]`.

[4] M. Galassi et al., *GNU Scientific Library Reference Manual - Third Edition*, 2009.

Part IV

A look at the data

Chapter 8

Data management and off-line monitoring

Introduction

In this chapter, I will describe the database application which I have projected and developed for the GERDA experiment. It provides a powerful (support of the Structured Query Language (SQL) [1]) and easy (web interface, preconfigured reports) access to the data. Reports are daily checked to ensure that everything is running in the proper way: the application allows an easy off-line monitoring of the data quality.

8.1   Data blinding

Before the start of the Phase I, the rawfiles produced by the Data Acquisition System (DAQ) of Ge detectors were available to the entire collaboration. In the Phase I, a blinding procedure is applied to the data: in the GELATIO [2] processing of the DAQ raw data files, events with an energy in the window $Q_{\beta\beta} \pm 20$ keV, according to the DAQ reconstruction (the algorithm stored in the DAQ board is the same of the GELATIO one) are not included in the output Tier1 files (Fig. 5.6). Only these files are available to the collaboration. So, at the moment, the collaboration is blinding itself. Rawfiles are stored, but no one can access them. No one can look at the events in the blinding window. The idea is to be able to provide a background model before the opening of the window, to avoid to be biased in the future. Unblinding of the data is planned for the next months.
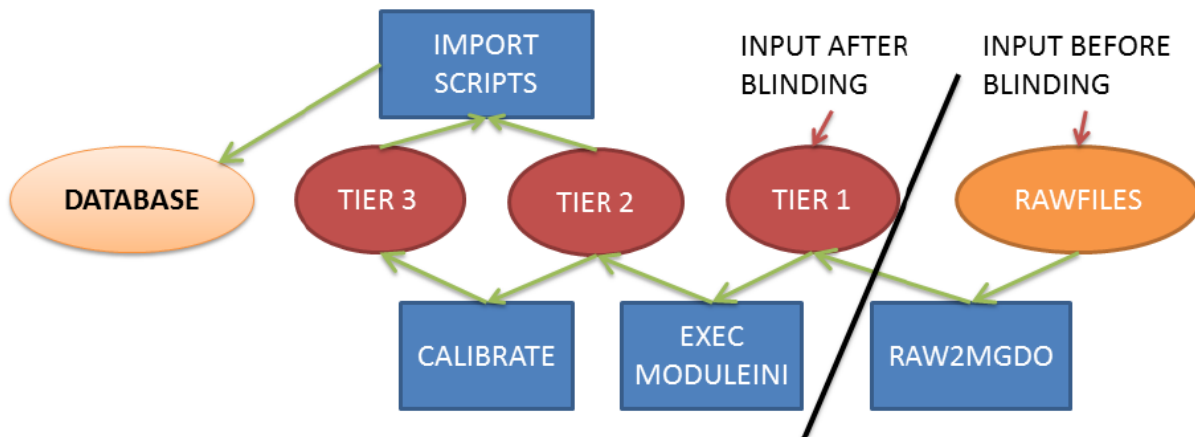
Figure 8.1: Sketch of the input pipeline: data processing flow. After the standard GELA-TIO pipeline, a few scripts import the data from Tier2 and Tier3 into the database. The black line represents the blinding: before the blinding, the application launched the full GELATIO pipeline, starting from the rawfiles; after the blinding, the application starts from the public Tier1 data.

8.2   The database application

The public signal data files are processed according to the standard GELATIO pipeline (Fig. 5.6). A set of scripts imports the results of the GELATIO pipeline in a MySQL database [3], as presented in 8.1. So there are multiple possibilities to look at the data:

- for people skilled in the ROOT framework, it is possible to look directly at the GELATIO output files

- for people having a good SQL knowledge, it is possible to send queries to the database by using the web interface

- for a fast check of the data, it is possible to ask for the pre-defined reports of the application.

Of special importance are the data quality reports, which are daily checked by a human shifter to ensure that everything is running in the proper way. It is an off-line monitoring of the data [4]. While the slow-control system of GERDA is able to provide on-line alarms for an abnormal behaviour of the main sub-components of the experiment (Cryostat, Clean Room, Water Tank, electronic crates and temperatures, High Voltage Systems, Radon Monitor and Source Insertion System), the off-line monitoring is related to e.g. noise levels in the data, event rates, analysis of test pulses. The database is updated once a day, in the night. The structure of the database application is sketched in Fig. 8.2.
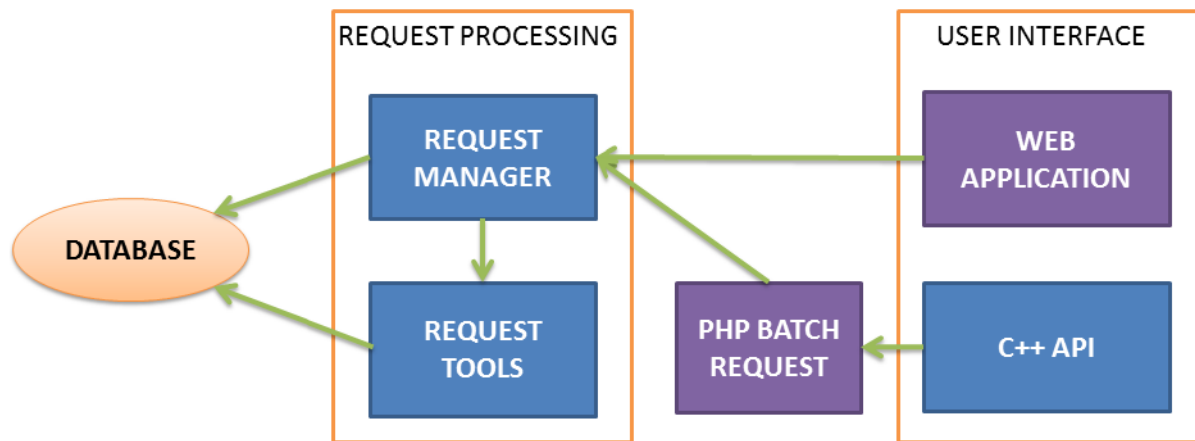
Figure 8.2: Sketch of the project: data request flow. In blue parts written in C++, in violet parts written in PHP. The central part of the system is the request manager. It is able to manage simultaneous requests from the web interface or from the Application Programming Interface (API), and manage them in a multithread way, with an advanced queue system for load balancing. Communications from/to the request manager are based on TCP/IP protocol.
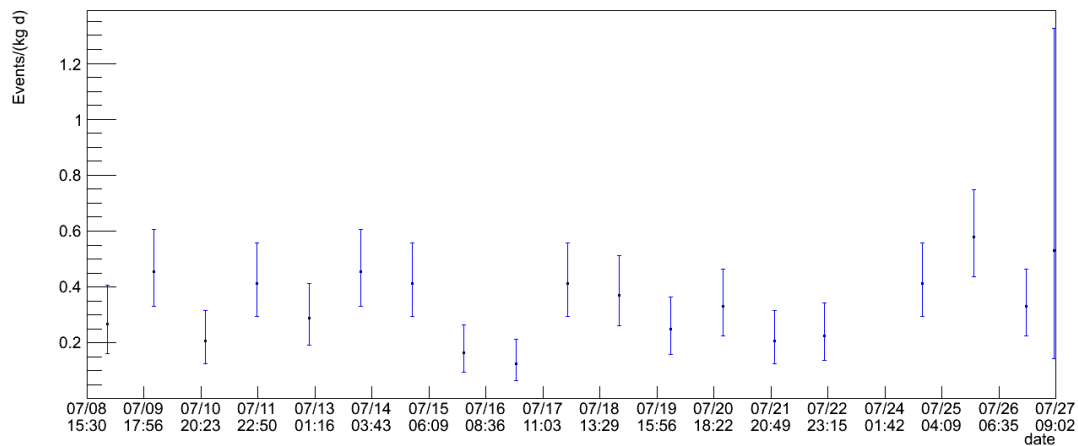
8.3   Rate monitoring

Important parameters to be monitored are the counting rates for different classes of events. The total event rate in the HPGe detectors is expected to be approximately constant in time. It is important to monitor the rate of muon-induced events, which are flagged by the muon veto (in Fig. 8.3, the upper plot shows the normal behaviour). An abnormal rate could relate to problems in the muon veto system. The possible occurrence of noise bursts which trigger the DAQ system can cause a substantial increase of the event rate with respect to the normal value (in Fig. 8.3, central plot, a few noise bursts are clearly visible). A change in the rate of single detector events could indicate problems with the thresholds or with the high voltage (in Fig. 8.3 the bottom plot shows the normal behaviour).

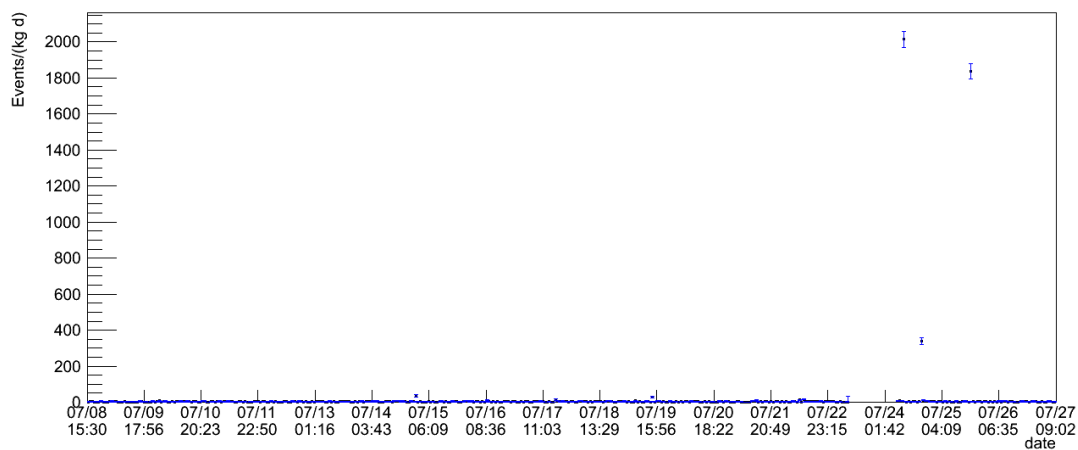## 8.4   Data quality monitoring

To monitor the read-out electronic chain and the DAQ system stability, the database application provides special reports like

- Amplitude of the baseline vs. time. Fluctuations or drifts in the position of the baseline may indicate changes in the leakage current of the HPGe detectors or in
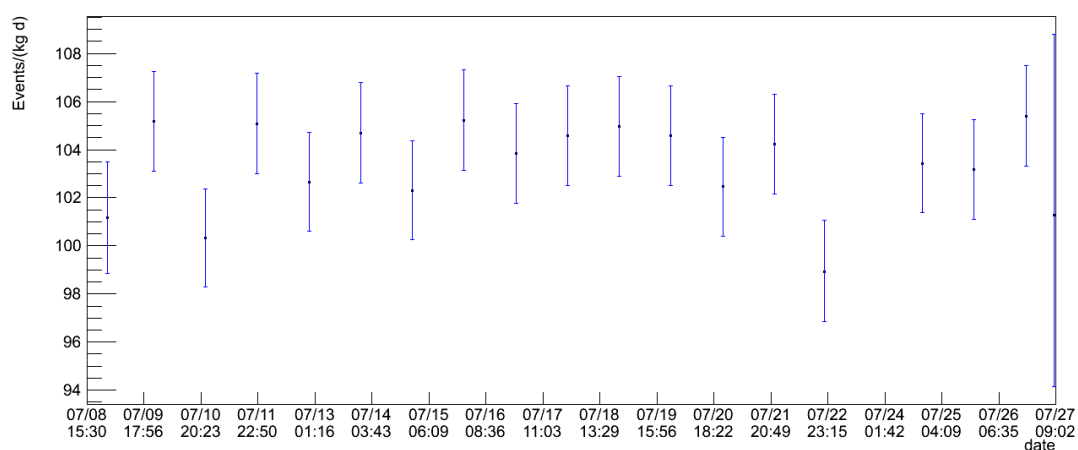
Figure 8.3: Examples of rate monitoring: at the top, the rate of muon-induced events (bin size=24h). In the middle, the rate of noise events (the acquisition has been triggered but the signal is not physical) (bin size=1h). At the bottom, the rate of single-detector events (bin size=24h).

the gain of the electronic chain. An example is given in Fig. 8.4, top plot. RG2 detector is working bad.

- Root-mean-square (rms) of the baseline vs. time. The fluctuations of the baseline position with respect to the average value are a direct measurement of the noise of the electronic chain. Variations or sudden shift of the baseline rms are symptoms of changes in the operation of the electronic chain.

- Test pulse amplitude vs. time. Since the signal injected in the electronic chain is constant, a time variation of its amplitude indicates a change in the global response of the electronic chain, e.g. gain drift, change in the system capacitance, etc. An example is given in Fig. 8.4, bottom plot. In this particular case, there were oscillations with a period of 1 day, which were also present in the input test pulse signal. These oscillations could be explained by temperature fluctuations in the electronics room.

8.5 Conclusions

A database application has been developed by me to import the output of the GELATIO processing into a MySQL database, so that it is possibile to use the power of SQL to extract information from the data. Moreover, the database application features a web-interface and a set of pre-defined reports, so that it is possible to follow the experiment by simply looking at the web, bypassing a knowledge of ROOT and of the filesystem structure of the GERDA data server. The reports are daily checked to ensure that everything is running in the proper way: it is an off-line monitoring of the data which is complementary to the slow-control system.

Bibliography

[1] ISO/IEC, *SQL - Structured Query Language - Standard ISO/IEC 9075*, available at `http://www.mysql.com`.

[2] M. Agostini, L. Pandola, P. Zavarise, and O. Volynets, *GELATIO: A General framework for modular digital analysis of high-purity Ge detector signals*, JINST **6** (2011), P08013, available at `arXiv:1106.1780[physics.data-an]`.

[3] Oracle, *MySQL*, available at `http://www.mysql.com`.

[4] P. Zavarise, M. Agostini, A.A. Machado, L. Pandola, and O. Volynets, *Off-line data quality monitoring for the GERDA experiment*, J.Phys.Conf.Ser. **375** (2012), 042028, available at `arXiv:1111.7200[physics.data-an]`.

RG2 channel - Baseline versus time
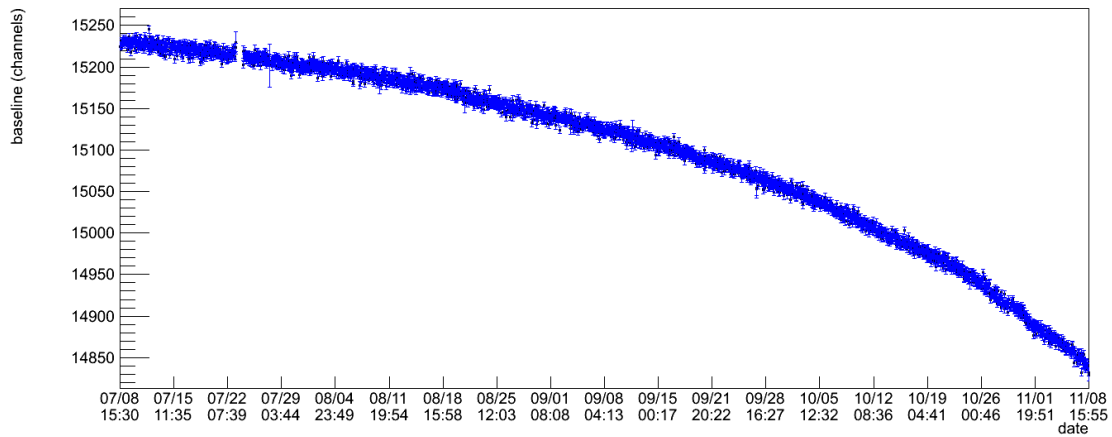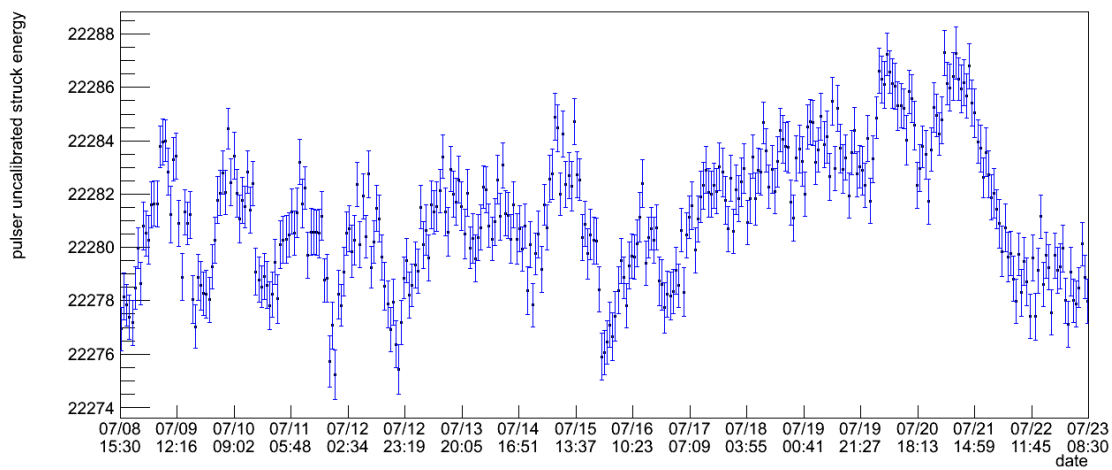

RG2 channel - Test pulses versus time

Figure 8.4: Monitoring plots: baseline and test pulses equivalent energy reconstruction as a function of time.

Chapter 9

GERDA Status

Introduction

In this chapter I will provide a quick summary of the Phase I status. I will focus on the duty cycle, on the acquired exposure, on the energy spectrum and on the background index around $Q_{\beta\beta}$.

9.1 Duty cycle and exposure

A key parameter for any experiment is the average duty cycle. Given a time period, it is the fraction of the livetime (when at least one detector is running in the proper way) over the total time.

Data acquisition is divided into many runs. During a run, the configurations of the geometry and of the electronics are kept unchanged. If everything is working properly, data acquisition during a run is interrupted only when a calibration of the system has to be performed. It is typically performed once per week and the procedure requires less than two hours in total. In Tab. 9.1 the list of the first Phase I runs is summarized. From the beginning of Run 25 to the end of Run 38, the time interval is 336.676 days. Without considering Run 31 and Run 33, which were quite unstable from the point of view of electronics, a very conservative estimate of the total livetime is 259.819 days, which corresponds to a duty cycle

$$\text{duty cycle} = \frac{259.819}{336.676} \simeq 77\%$$

which is not optimal. It is probably possible to recover some data from Run 31 and Run 33, and in this case the duty cycle will improve in a substantial way.

The exposure of the enriched detectors in the same period is about 11.2 kg·yr. Plots of the acquired exposure as a function of time are presented in Fig. 9.1. Two trend lines

```
Run |              Start |               Stop |  Time |  Live |Fraction|    Exp | Quality
    |                    |                    |  days |  days |      % |  kg y |
 25 | 2011-11-09 17:50:10 | 2011-12-02 10:51:40 | 22.709 | 20.510 | 90.316 |  0.821 |
 26 | 2011-12-02 14:13:43 | 2012-01-11 11:31:45 | 39.888 | 39.278 | 98.473 |  1.573 |
 27 | 2012-01-11 11:40:09 | 2012-01-16 16:04:28 |  5.184 |  5.179 | 99.906 |  0.207 |
 28 | 2012-01-16 17:26:37 | 2012-01-26 15:45:13 |  9.930 |  9.556 | 96.242 |  0.383 |
 29 | 2012-01-26 15:49:37 | 2012-02-16 08:23:57 | 20.691 | 20.363 | 98.418 |  0.815 |
 30 | 2012-02-17 12:30:49 | 2012-03-21 10:11:40 | 32.903 | 30.891 | 93.883 |  1.237 |
 31 | 2012-03-24 12:54:09 | 2012-04-23 14:52:06 | 30.040 | 28.425 | 94.622 |  1.138 | BAD
 32 | 2012-04-23 17:47:31 | 2012-05-22 09:44:09 | 28.664 | 26.559 | 92.655 |  1.064 |
 33 | 2012-06-02 12:07:51 | 2012-06-15 09:52:29 | 12.906 | 11.195 | 86.740 |  0.448 | BAD
 34 | 2012-06-15 12:08:35 | 2012-07-02 10:25:16 | 16.928 | 14.792 | 87.382 |  0.592 |
 35 | 2012-07-08 15:30:21 | 2012-07-27 09:02:20 | 18.731 | 17.739 | 94.706 |  0.856 |
 36 | 2012-07-27 09:02:56 | 2012-09-03 18:12:24 | 38.382 | 37.677 | 98.163 |  1.883 |
 37 | 2012-09-03 20:11:43 | 2012-09-27 10:44:26 | 23.606 | 23.421 | 99.215 |  1.125 |
 38 | 2012-09-27 12:18:59 | 2012-10-11 11:03:22 | 13.947 | 13.853 | 99.323 |  0.665 |
```

Table 9.1: List of the first Phase I runs. Columns are: run, start time, end time, total time in days, livetime in days, livetime fraction, exposure of enriched detectors, run quality.

have been computed to describe the curve and it seems that the Phase I goal (an exposure of 20 kg·y) will be reached in Spring 2013.

9.2   The energy spectrum

In Fig. 9.2, the sum energy spectrum obtained from the enriched detectors is presented. It refers to single-detector, not induced by muons events, and Runs 25-32 without Run 31, for an exposure of 6.10 kg·yr. Pulse shape discrimination techniques have not been applied.

The energy window could be divided into four parts:

- The ^{39}Ar region. The fraction of ^{39}Ar in natural Argon is described by an activity of (1.01±0.08) Bq/kg [1]. The electron emitted in the ^{39}Ar beta decay, could reach a kinetic energy of 565 keV. If the decay happens near to a detector, it could cause a signal. ^{39}Ar decays dominate the continuum between 0 and 565 keV. Our estimates of the ^{39}Ar activity are fully compatible with [1].

- The $2\nu\beta\beta$ region. Between 565 keV and $Q_{\beta\beta}$, the energy spectrum of enriched detectors clearly shows the typical shape of $2\nu\beta\beta$ decays inside the detectors, which I have presented in Fig. 2.2.

- The high-energy gamma continuum region.

- The α region. Alpha events are related to surface contaminations of the detectors.

The most prominent gamma lines have been identified. They are related to ^{40}K, ^{42}K, ^{214}Bi and ^{208}Tl decays.
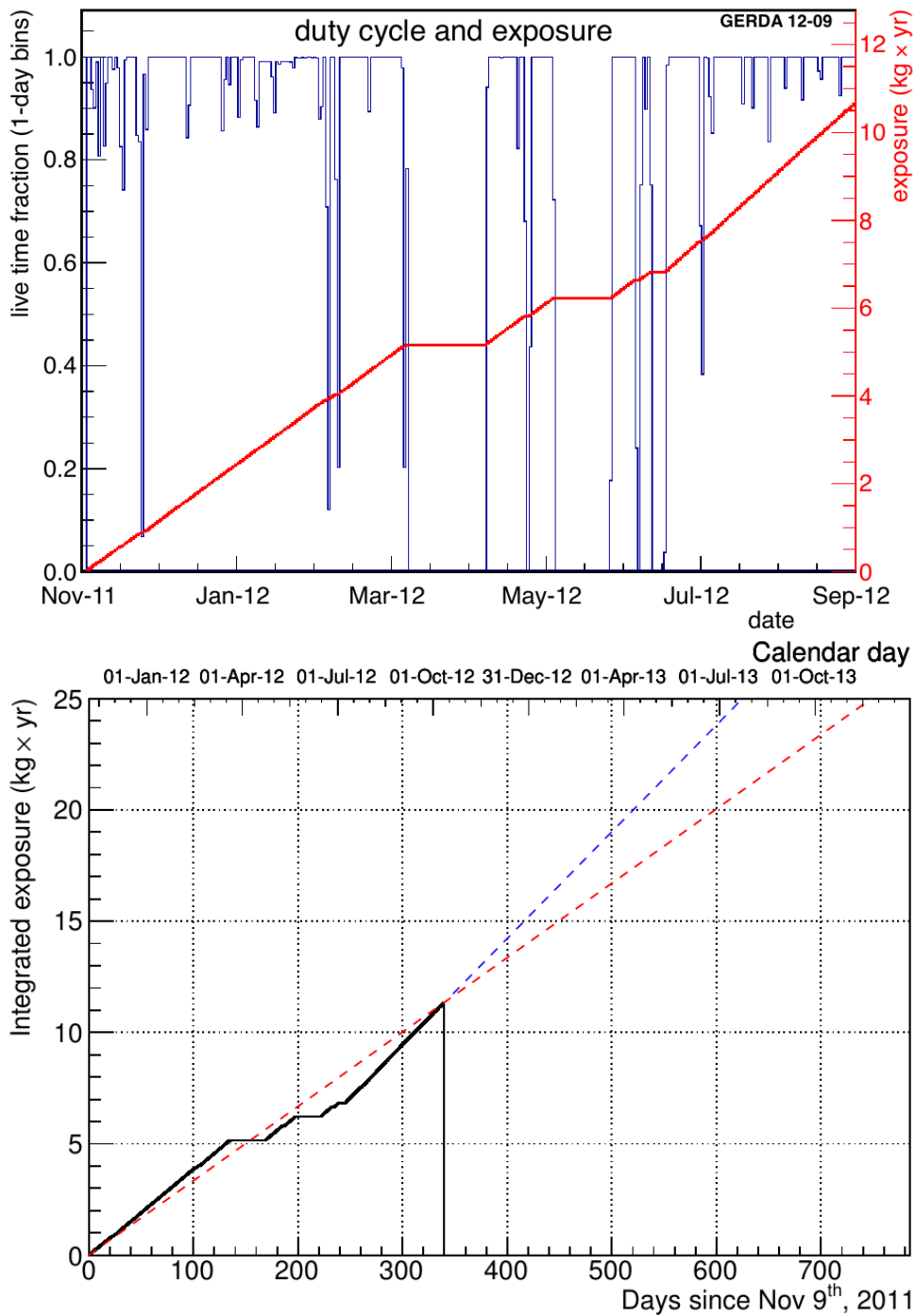
Figure 9.1: Duty cycle and exposure. In the upper plot, the livetime fraction is shown as a function of time. The bin size is 1 day. The red line describes the acquired exposure. In the lower plot, two trend lines of the exposure versus time curve are presented. Considering all the Phase I period, the result is described by the red dashed line. Considering only the last months, the result is described by the blue dashed line. Note that the blue line is steeper, due to the higher deployed mass. In any case, GERDA will probably reach an exposure of 20 kg·yr (the Phase I goal) in Spring 2013.
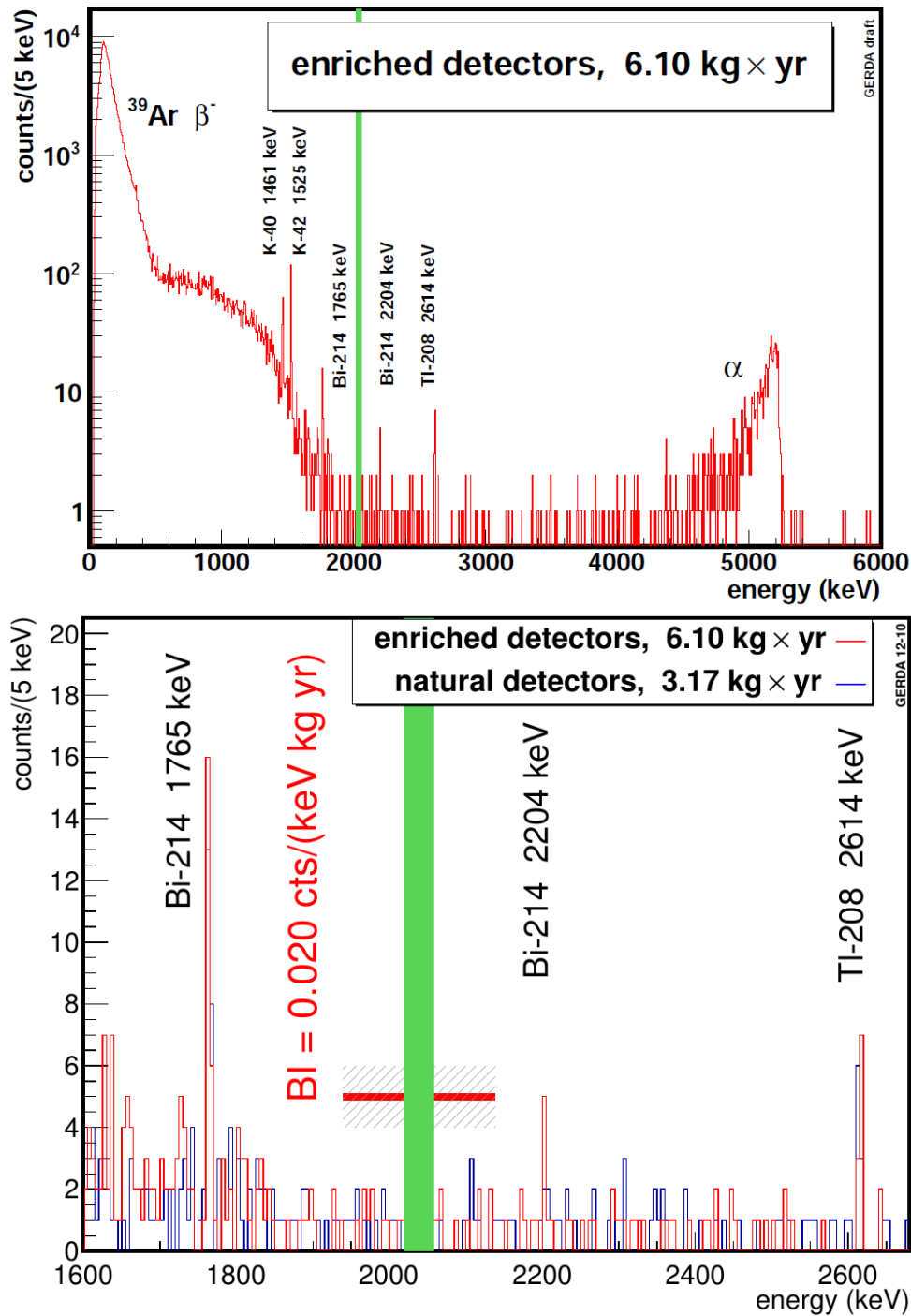
Figure 9.2: Sum energy spectrum (single-detector spectra are summed). Anticoincidence and muon veto cuts have been applied. Pulse shape discrimination techniques have not been applied. In the upper plot, the full sum energy spectrum of the enriched detectors, after an exposure of 6.10 kg·yr (Runs 25-32 without Run 31). In the lower plot, a zoom of the region 1600-2700 keV. In this plot, both enriched (red bars) and natural (blue bars) detectors are considered. The green bar describes the blinding window, $Q_{\beta\beta} \pm 20$ keV. The background index, considering a window of $Q_{\beta\beta} \pm 100$ keV (without the blinding window, so the window size is 160 keV), is 0.020 cts/(keV kg yr).
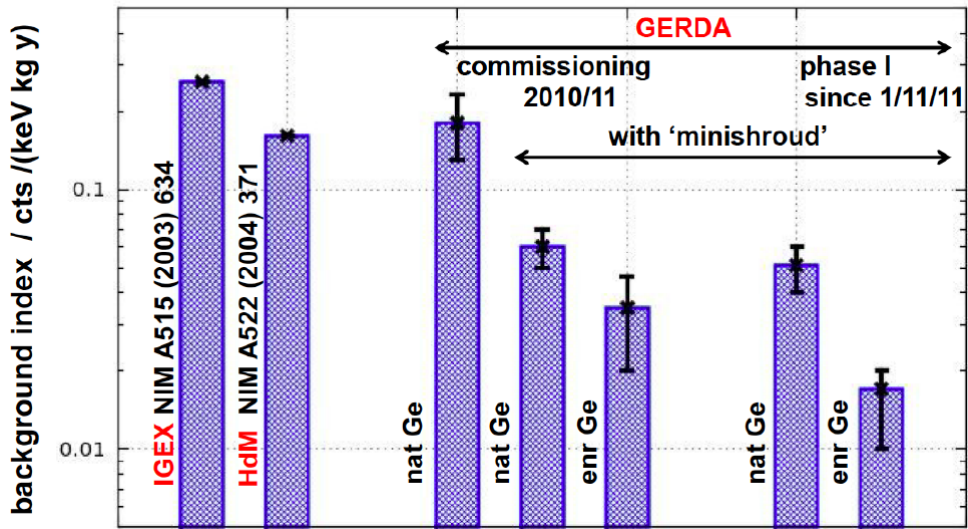
Figure 9.3: The GERDA background index compared to the background of IGEX and HdM.

9.3   Background index

In the lower plot of Fig. 9.2, the background index after an enriched exposure of 6.10 kg·yr is presented.

In the window $Q_{\beta\beta} \pm 100$ keV minus the blinding window, 20 single-detectors non-muon-induced events has been found. Thus the average background index is

$$\text{B.I.} = \frac{20 \text{ counts}}{160 \text{ keV } 6.10 \text{ kg} \cdot \text{yr}} = 0.020 \, \frac{\text{counts}}{\text{keV kg yr}}.$$

In Fig. 9.3, the background index for natural and enriched detectors, in the Commissioning and in the Phase I, is compared to the one of the Heidelberg-Moscow [2] and IGEX [3] experiments. GERDA shows the lowest background in ^{76}Ge experiments.

It is quite important to emphasize the improvement obtained by surrounding the detector strings with a thin copper shield (the mini-shroud, Fig. 4.4). The mini-shroud has been developed because it helps in creating a field-free enviroment inside the cryostat. It seems that, without the minishroud, the electric field could attract ions near the detectors, expecially ^{42}K ions which result from ^{42}Ar beta decay. The decays of ^{42}K ions can release a photon of 1524 keV, which is the most evident line that it is possible to see in the GERDA energy spectrum, and the β emitted could reach a kinetic energy of 3525 keV. If the decay takes place near the detector surface, it could release an energy around $Q_{\beta\beta}$ in the detector. The observed intensity of the 1524 keV line correspond to an ^{42}Ar activity in natural argon above two times the upper limit in literature [4]. I will return on the ^{42}Ar problem in chapter 11.

9.4   Conclusions

In this chapter I have given a quick summary of the present status of the GERDA experiment. In the first 336 days of Phase I, the duty cycle is about 77%, and the collected exposure is 11.2 kg·yr. It is probably possible to recover some data from two unstable runs. GERDA features the lowest background index obtained in ^{76}Ge experiments. An exposure of 20 kg·yr should be reached in Spring 2013, and, with the present level of background, will allow a strong statement about the validity of the Klapdor's analysis.

Bibliography

[1] P. Benetti et al., *Measurement of the specific activity of Ar-39 in natural argon*, Nucl.Instrum.Meth. **A574** (2007), 83-88, available at `arXiv:astro-ph/0603131`.

[2] Klapdor-Kleingrothaus H.V., A. Dietz, I.V. Krivosheina, and O. Chkvorets, *Data acquisition and analysis of the Ge-76 double beta experiment in Gran Sasso 1990-2003*, Nucl.Instrum.Meth. **A522** (2004), 371-406, available at `arXiv:hep-ph/0403018`.

[3] C.E. Aalseth et al., *The IGEX Ge-76 neutrinoless double beta decay experiment: Prospects for next generation experiments*, Phys.Rev. **D65** (2002), 092007, available at `arXiv:hep-ex/0202026`.

[4] V.D. Ashitkov, A.S. Barabash, S.G. Belogurov, G. Carugno, S.I. Konovalov, et al., *Liquid argon ionization detector for double beta decay studies* (2003), available at `arXiv:nucl-ex/0309001`.

Chapter 10

Muon-induced background

Introduction

In this chapter I will analyze the performance of the GERDA muon veto. The goal is to provide an estimate of the contribution of non-identified muon-induced events in the Germanium detectors to the background around $Q_{\beta\beta}$.

10.1   The muon veto

The Gran Sasso mean overburden of 3500 m.w.e. reduces the flux of cosmic muons to about $1.2/(\text{h} \cdot \text{m}^2)$ and shifts the mean energy to 270 GeV. Muons penetrating the detector will lose energy by both electromagnetic interactions and by inelastic reactions with nuclei in which high energy neutrons can be produced. These neutrons will cause inelastic interactions themselves and produce more isotopes and neutrons. Hence muons are both a direct and indirect background source.

GERDA features a muon veto which relies on two components: the water tank, which is equipped by photomultipliers and is able to detect the Cherenkov light, and an array of plastic scintillators on the roof of the clean room. Signals from both detector systems are combined and a logical signal is continuously sent to the Germanium DAQ.

10.2   Monte Carlo simulation

The observed rate and energy distribution of muon-induced events in the Germanium detector (events which are flagged by the muon-veto) have been compared to the results obtained from a Monte Carlo simulation.

The Monte Carlo simulation has been performed using the GEANT4-based [1] framework MaGe [2], which is being developed jointly by the GERDA and Majorana Collaborations.

The physics models, the generation of the initial state, and most of the basic settings of the simulation are identical to what was used in [3]. In particular, the muons that are used as the initial state are sampled according to the code MUSUN [4], which contains a description of the overburden profile of the Gran Sasso mountain, and is hence able to produce the appropriate energy-angular correlation. Primary muons are tracked through a 1 meter thick layer of rock and through the experimental set-up, along with the electromagnetic and hadronic showers originated by them. The Monte Carlo model of the GERDA experiment used in [3] was a preliminary version of the design, featuring a different cryostat and a different detector array. In the Monte Carlo work presented here, the actually-built GERDA set-up has been taken into account; the simulation contains the array of three natural HPGe detectors which had deployed in the first part of the GERDA commissioning. The delayed radiation following the muon interaction (i.e. decay of radioactive isotopes) is not taken into account, lacking the possibility to correlate these events with the parent muon event detected by the veto.

10.3   Data and Monte Carlo comparison

A period of about 100 days has been considered (Runs 10-13. Previously, pulser events were not tagged with a simultaneous logical signal, and the properties of muon-induced events can be similar of those of test pulses: high energy, high detector multiplicity).
The rate of muon-induced events flagged by the muon veto has been compared with the Monte Carlo prediction in Tab. 10.1. It is clear that there is a really good agreement between Monte Carlo and data, and this can be seen as an indication that the efficiency of the muon veto is quite close to 1. The distributions of energy releases in a detector superimposed with the Monte Carlo prediction, for all the muon events and for single-detector events, are presented in Fig. 10.1. Single detector events are clearly more interesting, because they are not cut by an anticoincidence analysis.

	Events rate events/day	Events rate after a.c. events/day	Ratio
Data	2.94 ± 0.17	2.04 ± 0.14	$(69.4 \pm 6.2)\%$
Monte Carlo	2.88 ± 0.43	2.02 ± 0.30	$(70.1 \pm 14.8)\%$

Table 10.1: Rate of muon-induced events in Ge detectors. Only events with at least one energy deposit above 100 keV in a single detector have been considered, because the sensitivity of the GELATIO energy reconstruction is not clear at lower energies. In the first column, the event rate of all the muon-induced events is given. In the second column, the event rate of muon-induced single-detector events is presented. The last column gives the ratio between the latter and the former.
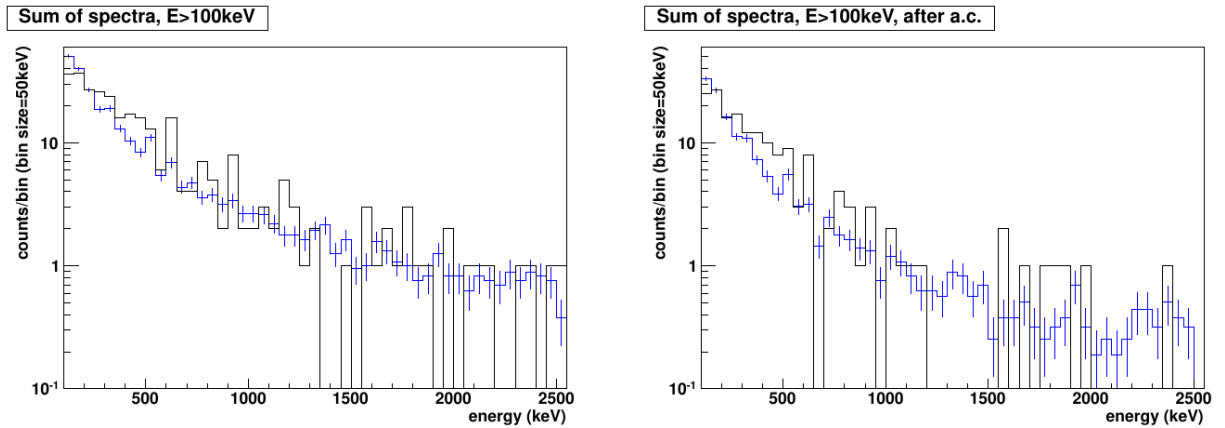

Figure 10.1: Energy spectrum of events in coincidence with the muon veto: sum of single-detector spectra before and after anti-coincidence cut. Black = experimental data. Blue = Monte Carlo prediction. Monte Carlo is scaled to the same exposure of the data.

In Fig. 10.1, the full energy spectrum above 100 keV has been considered. Now, I will focus on the $Q_{\beta\beta} \pm 200$ keV region, which is one of our reference windows for background estimates. A period of about 189.5 days has been considered (runs 1-13 except run 8, when muon veto was disconnected from the DAQ. In this case, pulser events are not a problem, because the equivalent energy is higher than $Q_{\beta\beta}$). Rates and Monte Carlo prediction are presented in Tab. 10.2. In Fig. 10.2, the distribution of energy releases in a detector superimposed with the Monte Carlo prediction. As in the previous case, the compatibility between data and Monte Carlo prediction is really good.

	Events	Events after a.c.	Ratio
Data	9 ± 3.0	3 ± 1.7	$(33.3 \pm 21.9)\%$
Monte Carlo	12.7 ± 1.9	5.0 ± 0.8	$(39.3 \pm 8.6)\%$

Table 10.2: Muon-induced events in Ge detectors, Runs 1-13 except Run 8, with and without the anti-coincidence cut. Monte Carlo is scaled to the same exposure of the data.
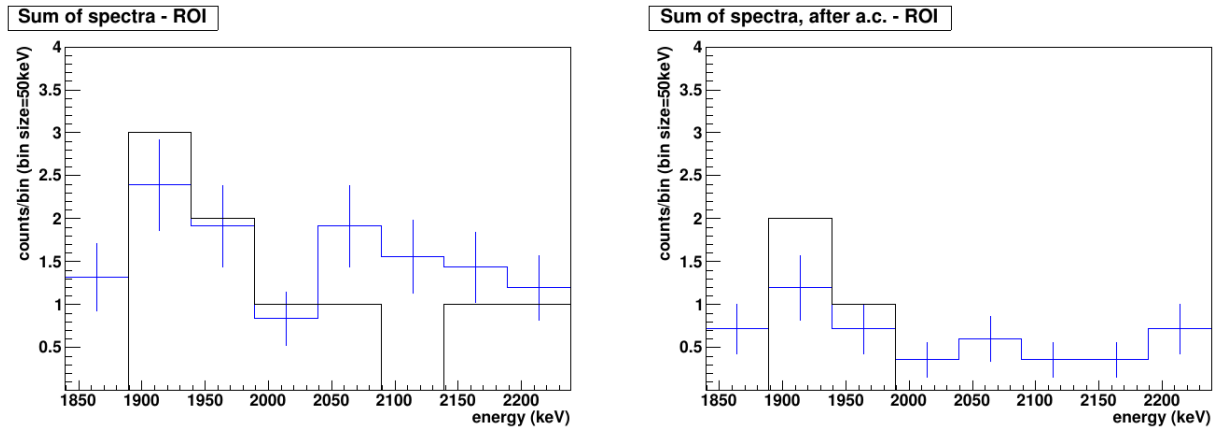

Figure 10.2: Energy spectrum in the region of interest (ROI: $Q_{\beta\beta} \pm 200$ keV): sum of single-detector spectra before and after anti-coincidence cut. Black = experimental data. Blue = Monte Carlo prediction. Monte Carlo is scaled to the same exposure of the data.

10.4   Muon veto efficiency

Now, we can move to the Phase I data. The goal is an estimate of the muon veto efficiency. In a rigorous sense, considering all the muons which traverse the veto, the muon veto efficiency is the number of flagged muons divided by the total number of muons. But only the information about the number of flagged muons is available.

How it is possible to estimate the "muon rejection efficiency"? The idea is to compare the number of muon-induced events in the germanium array which are flagged by the muon veto to the number of events which are not flagged by the muon veto, but which are probably induced by muons [6].

How to select these events? We can consider two classes of events:

- events with total energy above 4 MeV (namely above the Q-value of the ordinary β and γ-emitters) and at least two detectors fired. Notice that events due to α emitters could have more than 4 MeV of released energy (up to about 8 MeV) but this would be on a single detector

- events with more than 8.5 MeV deposited on a single detector. Being the energy above the Q-value of the natural α emitters, these events can be induced by cosmic ray muons only.

In my analysis, I have considered all the working detectors in GERDA runs 25-34, without runs 31, 33 (which were quite unstable).
The livetime is 167.129 days, and the total exposure is 10.57 kg yr (Tab. 10.3). I found six events of the first class, but it is not clear if two of them are really "physical". But, to have a conservative estimate, I decided to keep these events in the statistics.
I have not found events of the second class.
In the same period, 1193 events were flagged by the muon veto.
Given $N = 1193 + 6$ genuine muon events, the probability to have $n = 1193$ vetoed events out of N is given by the binomial distribution

$$f[n|N, \varepsilon] = \frac{N!}{(N-n)!n!} \varepsilon^n (1-\varepsilon)^{N-n}$$

being ε the muon-veto rejection efficiency. Assuming a flat prior probability between 0 and 1 for the efficiency, one can use the Bayes' theorem [5] to infer the posterior probability density function (PDF) of ε

$$f[\varepsilon|N, n] = \frac{(N+1)!}{n!(N-n)!} \varepsilon^n (1-\varepsilon)^{N-n}.$$

This continuous distribution has been plotted in Fig. 10.3. Then, my final result is

$$\varepsilon = 0.9950^{+0.0017}_{-0.0023} \qquad\qquad \varepsilon > 0.9900 \;\; 95\% \text{ lower limit.}$$

Detector	Exposure
	kg y
ANG1	0.2488
ANG2	1.2963
ANG3	1.0940
ANG4	1.0867
ANG5	1.2564
GTF112	1.3576
GTF32	0.9680
GTF45	0.9642
RG1	0.9668
RG2	0.9920
RG3	0.3416

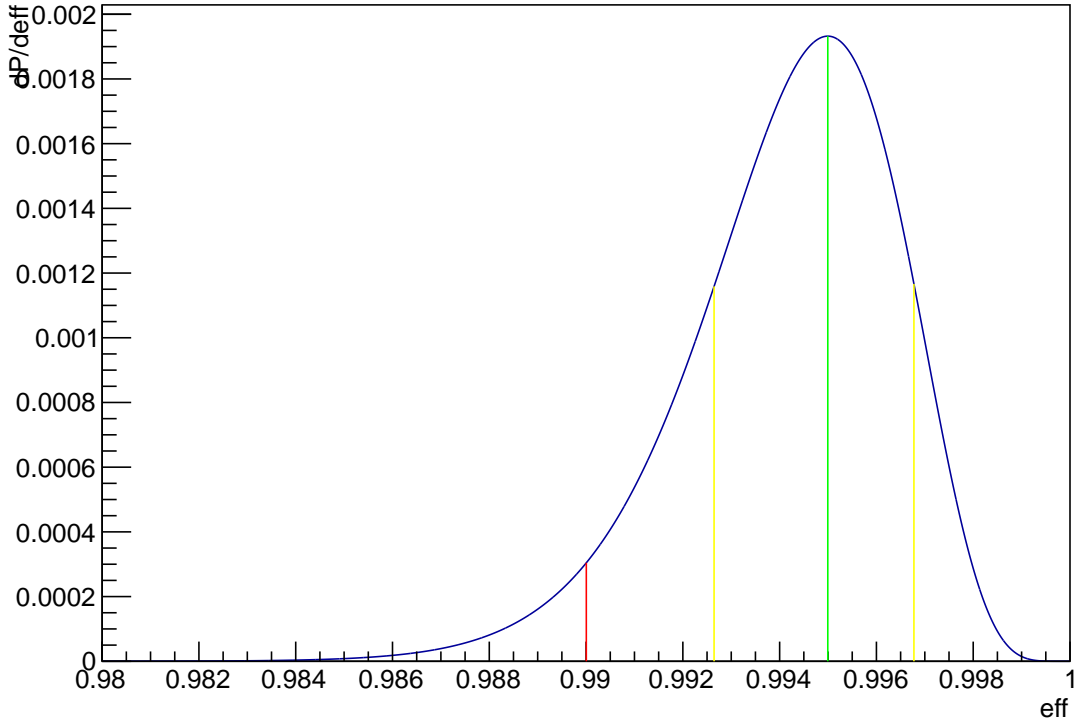Table 10.3: The considered statistics. Total exposure: 10.57 kg yr.

Figure 10.3: Muon veto efficiency - probability distribution. The green line indicates the best value, the yellow lines delimit the 68% minimal band, the red line is the 95% lower limit.

10.5   Background due to muons

From the previous result, it is possible to estimate the background induced by non-flagged muon events with a single-detector energy deposit between 1839 and 2239 keV ($Q_{\beta\beta} \pm 200$ keV.

During the considered period, I found 8 identified muon events with a single-detector energy release in the region of interest (ROI).

Inverting the Poisson distribution using a flat prior with the Bayes theorem, it is possible to obtain the probability distribution for the true rate of these events $\lambda_{id,1}$.

The idea is to obtain a probability distribution for the background index by using a sampling Monte Carlo approach.

From the PDF for the efficiency and the PDF for $\lambda_{id,1}$ one can extract samples $\hat{\epsilon}$ and $\hat{\lambda}_{id,1}$. In this way, using the definition of efficiency, in the hypothesis that the efficiency for single detector muon events is the same that the general one, it is possible to obtain a sample $\hat{\lambda}_{un,1}$ of the distribution of unidentified muon-induced single detector events with

energy in the ROI

$$\hat{\epsilon} = \frac{\hat{\lambda}_{id,1}}{\hat{\lambda}_{id,1} + \hat{\lambda}_{un,1}} \implies \hat{\lambda}_{un,1} = \hat{\lambda}_{id,1}\left(\frac{1}{\hat{\epsilon}} - 1\right).$$

By repeating this step many times, one can obtain the PDF for $\lambda_{un,1}$. It is easy to obtain the Background Index due to unindentified muons (B_μ) from the PDF for $\lambda_{un,1}$ because

$$B_\mu = \frac{\lambda_{un,1}}{\text{exposure} \cdot 360 \text{ keV}}.$$

where the correct window size has been used: 400 keV minus the 40 keV of the blinding window is equal to 360 keV. The plot of the final distribution is given in Fig. 10.4. Thus, my final result is

$$B_\mu = (1.0^{+0.7}_{-0.5}) \times 10^{-5} \; \frac{\text{counts}}{\text{keV kg yr}} \qquad\qquad B_\mu < 2.8 \times 10^{-5} \; \frac{\text{counts}}{\text{keV kg yr}} \; \; 95\% \text{ upper limit.}$$

10.6 Conclusions

Considering that the Phase I background goal is $10^{-2} \frac{\text{counts}}{\text{keV kg yr}}$, and the Phase II background goal is $10^{-3} \frac{\text{counts}}{\text{keV kg yr}}$, non-flagged single-detector events in the region of interest are for sure a very minor contribution to the total background: the muon veto is adequate for the GERDA Phases I and II.

Bibliography

[1] John Allison et al., *Geant4 developments and applications*, IEEE Trans.Nucl.Sci. **53** (2006), 270.

[2] M. Boswell et al., *MaGe-a Geant4-based Monte Carlo Application Framework for Low-background Germanium Experiments*, IEEE Trans.Nucl.Sci. **58** (2011), 1212-1220, available at `arXiv:1011.3827[nucl-ex]`.

[3] L. Pandola et al., *Monte Carlo evaluation of the muon-induced background in the GERDA double beta decay experiment*, Nucl.Instrum.Meth. **A570** (2007), 149-158.

[4] V.A. Kudryavtsev et al., *Simulations of muon induced neutron flux at large depths underground*, Nucl.Instrum.Meth. **A505** (2003), 688-698, available at `arXiv:hep-ex/0303007`.

[5] G. D'Agostini, *Bayesian reasoning in data analysis: A critical introduction*, 2003.

[6] D. Budjas, L. Pandola, and P. Zavarise, *Rejection efficiency of muon-induced events in the commissioning GERDA array*, Internal GERDA note, GSTR-11-002 (2011).
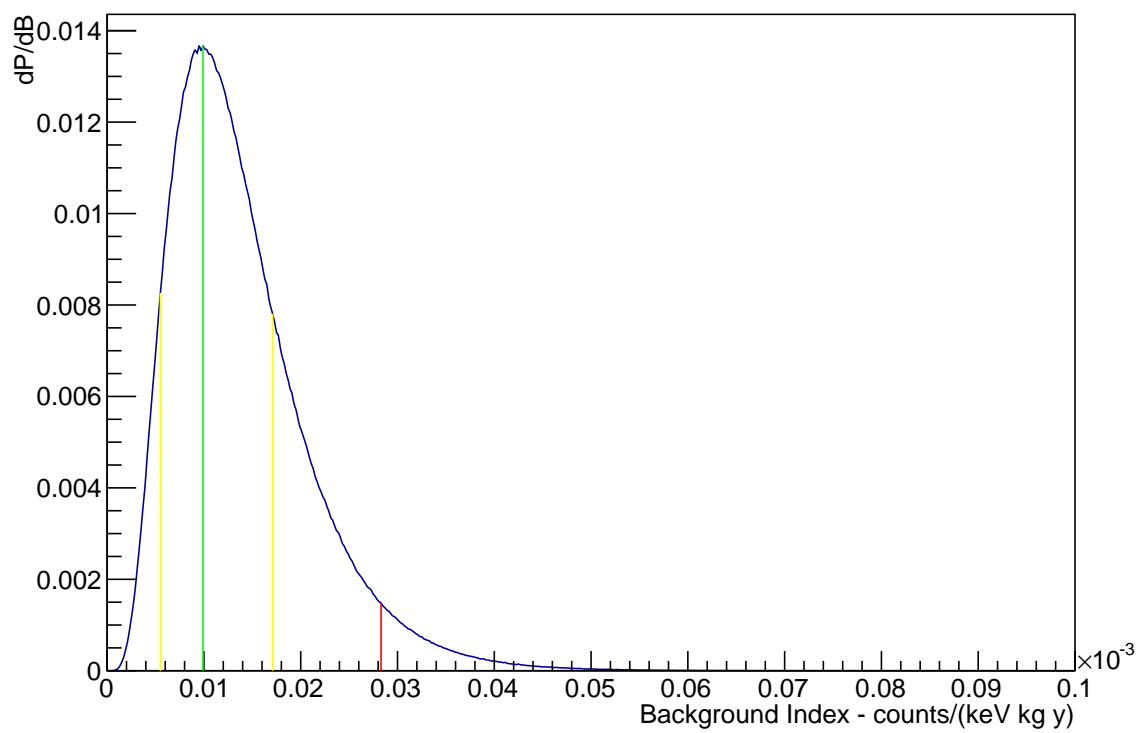
Figure 10.4: Background in the ROI - probability distribution. The green line indicates the best value, the yellow lines delimit the 68% minimal band, the red line is the 95% lower limit.

Chapter 11

Gamma background

Introduction

In this chapter I will describe an original approach to find gamma ray peaks in the energy spectrum, without any other input. It is a fully blind approach. Peaks are modeled with a gaussian shape, and the algorithm is able to provide their mean, standard deviation and area, which is proportional to the gamma rate. I will compare my results with the "official" GERDA results, and with the background of the Heidelberg-Moscow experiment. At the end of the chapter, I will discuss the anomalous ^{42}Ar related background.

11.1   Peak finder

It is important to find and identify gamma peaks in the energy spectrum, because they can drive the decomposition of the continuum.

There are only few "eye-visible" peaks in the GERDA energy spectra. This was expected, because GERDA is a low background experiment, and the exposure collected until now is too low to provide gaussian-shape evidence for low-rates photopeaks.

I have developed an algorithm to scan the sum energy spectrum (sum of the energy spectrum of each detector), to search for count excesses compared to a smooth model for the continuum. The key idea is to fit the spectrum by using an uniform spline. Uniform means that the distance between the connection points of the piecewise polynomial is a constant, then the region sizes are constant. The spline should be characterized by a region size very large compared to the typical peak size, which depends on detector resolutions. Typically, the peak scale is on the order of a few keV.

In this way, it is obvious that peaked structures characterized by the typical line-scale are fitted in a bad way by the spline. Thus, after the fit, it is possible to scan the spectrum for count excesses compared to the fit result. When a count excess is identified, the small

peak window is excluded from the next iteration of the algorithm. Then, in the next iteration, the spline is unconstrained in these windows. The iterations will stop when the scan converges: when no new count excesses are observed.

In my opinion, this approach is interesting especially for the modeling of the continuum. When the peak problem is managed in a "local" way, the standard approach is to model the background as a very simple polynomial (order 0 or 1) and to choose a window large enough to constrain the background in a good way. Thus, the background model is "local", and different result could be obtained for different window widths. In my approach the only scale involved is the region size, which is very large compared to the line size, and the fit is a function of the whole spectrum.

11.1.1   m-spline fit of the energy spectrum

The model

It is possible to try an unbinned or a binned fit of the spectrum. We can model the background index as

$$B[E] = \sum_{k=1}^{n} b_k B_k[E]$$

where the n functions $B_k[E]$ are the spline basis for the region configuration. I have chosen to work with cubic splines (three is usually the degree of choice, because it is a good compromise between quality and risk of polynomial oscillations), but the spline order is simply a parameter of the algorithm. $\{b_k\}$ should be non-negative, to ensure the positivity of the model in the whole energy range considered. The trick to restrict spline coefficients to positive values is called m-spline approach [1]. At a first glance, it seems to limit the spline space in an excessive way, but in practice a minor spline quality can be balanced by using more connection points (a lower region size).

Now it is time to provide expressions for the unbinned and binned likelihoods.

Unbinned fit

In an unbinned fit, the likelihood is given by

$$\mathcal{L}_{unbinned} = \Big(\prod_i \frac{\sum_{k=1}^{n} b_k B_k[E_i]}{\sum_{k=1}^{n} b_k Q_k} \Big) \Big(\frac{\exp\big[- \big(\sum_{k=1}^{n} b_k Q_k \mathcal{E} \big) \big] (\sum_{k=1}^{n} b_k Q_k \mathcal{E})^N}{N!} \Big)$$

where $\mathcal{E}$ is the exposure, N is the number of counts in the full fit region, i is an event index and

$$Q_k = \int B_k[E] dE$$

is the integral of the basis $B_k[E]$ in the full fit region. Thus we need to find n parameters: the b_k coefficients. Note that an expression like

$$\mathcal{L}_{unbinned,simplified} = \Big(\prod_i \frac{\sum_{k=1}^n b_k B_k[E_i]}{\sum_{k=1}^n b_k Q_k} \Big)$$

with a fixed value for one of the b_k seems equally interesting. The number of parameters decreases of 1. I have not preferred this expression, because it manages the coefficients in an asymmetric way during the minimization: one is fixed (and pay attention to its scale, a wrong choice could cause numerical problems), the others are free to move in the parameters space.

Binned fit

In a binned fit, the likelihood is instead

$$\mathcal{L}_{binned} = \Big(\prod_i \frac{\exp\Big[-\sum_{k=1}^n b_k M_{k,i}\mathcal{E}\Big] (\sum_{k=1}^n b_k M_{k,i}\mathcal{E})^{n_i}}{n_i!} \Big)$$

where i is the bin index, n_i the number of events in the bin and

$$M_{i,k} = \int_{i-bin} B_k[E]dE$$

is the integral of the basis $B_k[E]$ in the bin.

11.1.2   Automatic choice of the energy scale

What is a good energy scale (the size of the regions in the spline fit) for our purposes? We need an energy scale higher than the peak structure, but low enough to have a good fit of the continuum. The idea is to repeat a fit of the full energy spectrum for different energy scales, and then choose the best model according to the usual model selection indexes (the Bayesian Information Criteria (BIC) and the Akaike Information Criteria (AIC)) [2]. So, to have a first idea of the energy scale for the m-spline fit, I have fitted the energy spectrum between 300 and 4000 keV with a cubic m-spline varying the number of regions from 1 to 20.

From the left plot in Fig. 11.1, it is possible to understand that BIC and AIC indexes have the same behaviour. The main features of the spectrum are not fitted with a number of regions less than 11. Between 11 and 12, the indexes worse a little, and it means that main features have been detected, and now the fit is trying to describe second-order features. Eleven regions corresponds to a energy scale of 336 keV, twelve regions to a energy scale of 308 keV.

I finally decided to use a 300 keV region size, and to choose as fit region the range 250-3250 keV.
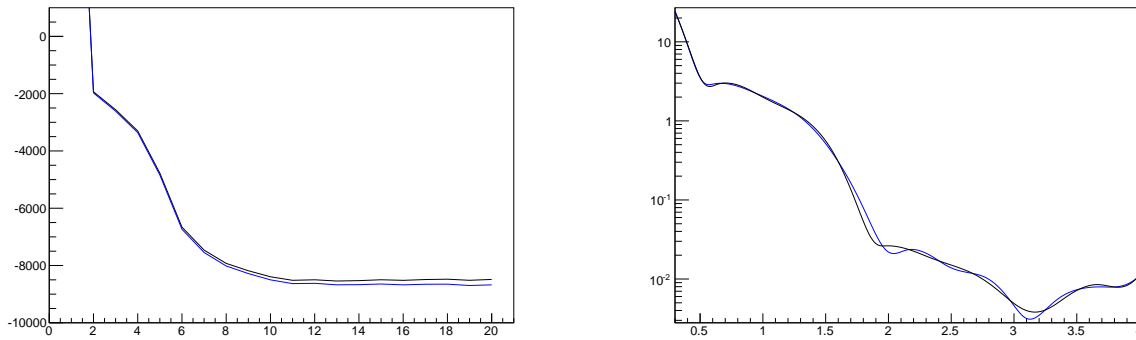
BIC index (black) and AIC index (blue) vs the number of regions.

Spectrum (Background Index) fit for 11 (blue) and 12 (black) regions.

Figure 11.1: Automatic choice of the energy scale.

11.1.3   Finding peaks in the energy spectrum

After the fit, the algorithm scans the full energy spectrum to search for rate excesses.

By default, the algorithm test window sizes between 2 and 10 keV, at steps of 0.25 keV. It moves the window over the energy spectrum, at steps of 0.25 keV.

Given a window, if the number of observed counts is "very high" compared to the fit expectation value, the window is excluded from the next iteration of the fit. Very high means a p-value below a predefined value (I choose 10^{-4}) in the window region. A gaussian fit is done to obtain the parameters which describe the peak on the background described by the m-spline model.

It is important to remind that, when fitting a wide energy range and examining small bins, a count excess could be simply a statistical effect.

It means: given a definition of what is a line (p-value below 10^{-4}) (note that this is a local estimate), the algorithm could be improved to estimate for each line the probability that it is a statistical effect (and this is a global estimate). Currently, the algorithm focus only on peaks detection, so it is important to keep into account that false positives are possible.

11.2   Peak finder results

The data set for this analysis is made of GERDA Runs 25-34, without 31 and 33. I have considered only stable enriched detectors: ANG2, ANG3, ANG4, ANG5, RG1, RG2. The livetime is 167.129 days, and the total exposure in the period is 6.6924 kg yr.

I have tested the line-finder algorithm using different region-size scales, from 75 keV to 300 keV. Despite the fits are cleary different, as it is possible to see in Fig. 11.2 the

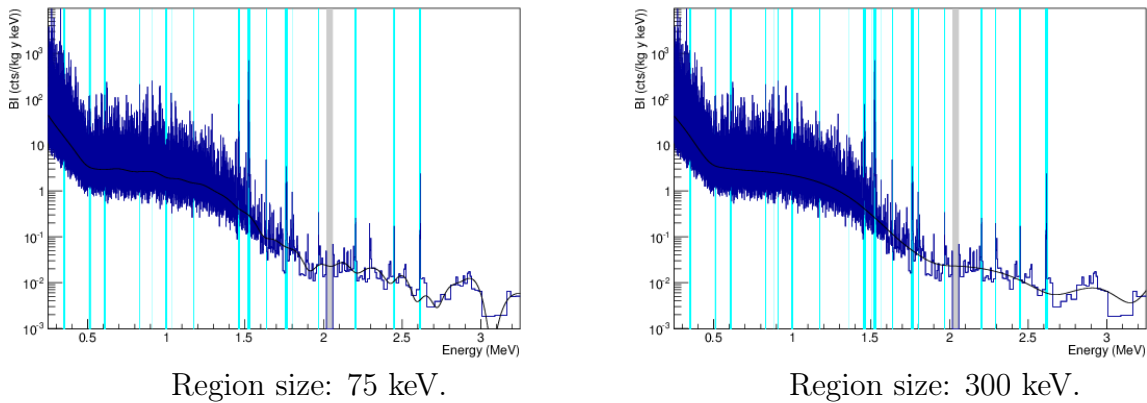Region size: 75 keV.   Region size: 300 keV.

Figure 11.2: Line finder results after ten iteration.

line selection agree in a stunning way between the most different scales. Few differences appear in the line widths, but the line centers are really compatible! In Tab. 11.1 the results obtained by using the suggested 300 keV window are presented, interpreted, and compared with the official ones and with the background estimates of the Heidelberg-Moscow experiment. The only clear difference between my results and the official ones is in the rate of 351 keV ^{214}Pb line. It is probably due to the fact that it is located on the ^{39}Ar region, which is very sloped. Note that there are three regions which require further investigation (around 828 keV, 884 keV, 999 keV) and that only one ^{60}Co peak is clearly visible.

Remember that I have summed all the detectors spectra, to manage the statistics in the simplest way. But, if a line appear only in few detectors, this line could be missed by the algorithm.

It is clear that improvements are possible. The most important is probably the ability to fit one detector at time, and sharing the information between the channels for the peaks identification.

11.2.1   GERDA and Heidelberg-Moscow background comparation

From Tab. 11.1 it is quite clear that our background is lower than the background of the HdM experiment, at least above the ^{39}Ar region.

This is a proof of the quality of our design: the GERDA concept is validated. The rates for most evident gamma lines are visually compared in Fig. 11.3.

```
   Mean  Sigma |    Rate (my algo) | Isotope        |  Rate (official) |     Rate (HdM) |
              |     counts/(kg yr) |                |   counts/(kg yr) |  counts/(kg yr) |
 351.80   2.50 | 23.5 - 5.2 +  5.3 | 214 Pb         | 12.5 - 7.7 + 9.5 |   138.7 +- 4.8 |
 513.69   1.67 |  6.7 - 2.1 +  2.2 | e^+ e^- 208 Tl |                  |                |
 609.46   1.79 |  7.5 - 2.1 +  2.2 | 214 Bi         |  6.8 - 4.1 + 3.7 |   105    +- 1  |
 828.68   0.62 |  4.2 - 1.3 +  1.4 | ????????????? |                  |                |
 884.95   0.47 |  3.5 - 1.1 +  1.2 | ????????????? |                  |                |
 912.63   0.35 |  3.1 - 1.0 +  1.1 | 228 Ac         | < 5.8            |    29.8 +- 1.6 |
 968.9         |                   | 228 Ac         |  2.7 - 2.5 + 2.8 |    17.6 +- 1.1 |
 999.79   0.65 |  3.8 - 1.2 +  1.3 | ????????????? |                  |                |
1172.54   0.47 |  2.5 - 0.9 +  1.0 | 60 Co          |  4.8 - 2.8 + 2.8 |    55    +- 1  |
1460.88   2.88 | 13.6 - 1.7 +  1.8 | 40 K           | 13.5 - 2.1 + 2.2 |   181    +- 2  |
1524.65   2.91 | 59.9 - 3.1 +  3.2 | 42 K           | Dedicated work   |                |
1764.20   3.08 |  3.9 - 0.8 +  0.9 | 214 Bi         |  3.6 - 0.8 + 0.9 |    30.7 +- 0.7 |
2203.50   1.52 |  0.8 - 0.3 +  0.4 | 214 Bi         |  0.4 - 0.4 + 0.4 |     8.1 +- 0.5 |
2293.37   0.68 |  0.5 - 0.2 +  0.4 | 214 Bi         |                  |                |
2449.38   0.79 |  0.4 - 0.2 +  0.3 | 214 Bi         |                  |                |
2614.54   2.50 |  1.6 - 0.5 +  0.6 | 208 Tl         |  1.5 - 0.5 + 2.6 |    16.5 +- 0.5 |
```

Table 11.1: Results of my line-search algorithm. The columns are: line position, resolution, rate, interpretation, official GERDA rate, HdM rate [3].
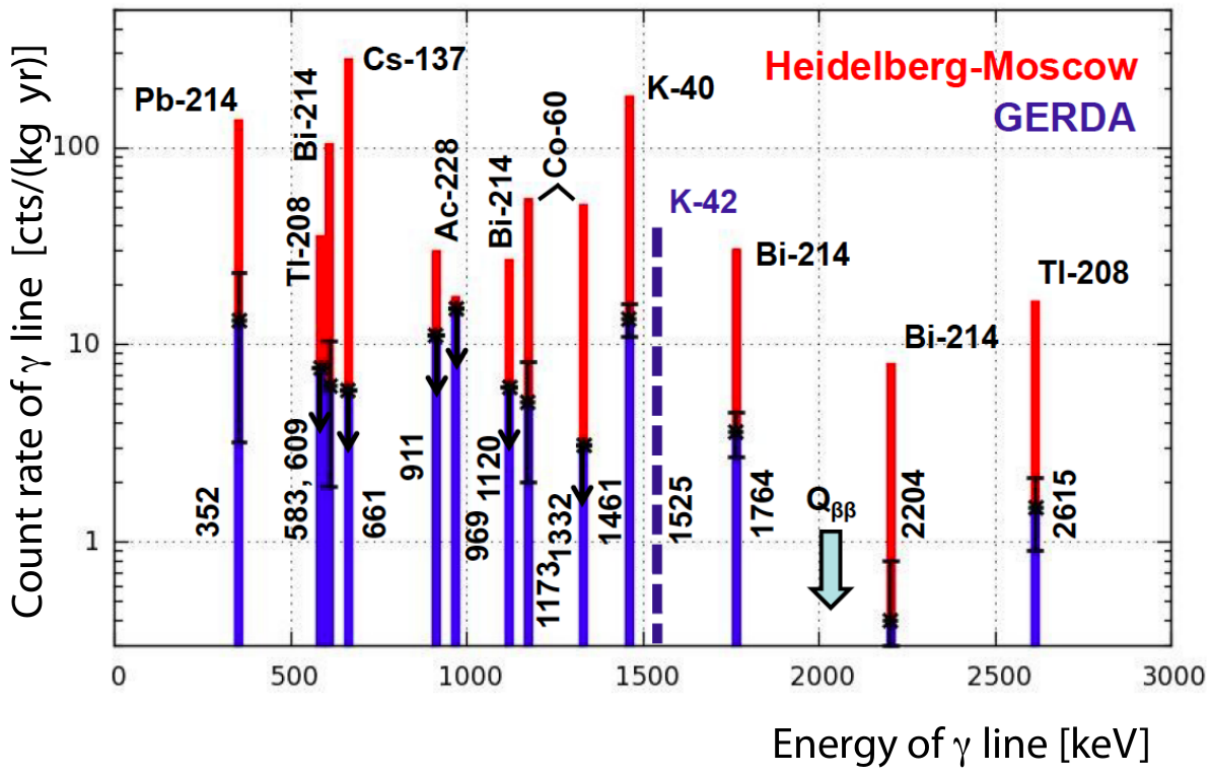

Figure 11.3: Rate of γ lines: comparison between GERDA and Heidelberg-Moscow.

11.3   The ^{42}Ar problem

As shown in Tab. 11.1, the most intense line that is observed in the GERDA background arises from ^{42}K β decay. A photon of 1524.7 keV is emitted with a branching ratio of 18.0%.

^{42}K nuclei originate from ^{42}Ar β decays. Like ^{39}Ar, ^{42}Ar is a radioactive component of the natural argon. Its decay scheme is shown in Fig. 11.4.

It is possible to estimate the ^{42}Ar activity in natural Argon required to obtain this line rate.

By using Monte Carlo simulation, the number of counts/day expected at 1524 keV for an ^{42}Ar activity of 1 μBq/kg (which has been named "efficiency", Tab. 11.2) in an electric field-free configuration has been computed for each detector.

10^9 decays of ^{42}K have been simulated in the Liquid Argon Volume surrounding the detectors. The initial states for the ^{42}K decay are sampled by generator Decay0 [4], which is able to produce the proper shape of the β decay spectrum, taking into account the fact that the β-decay is not Fermi-allowed.

The total efficiency is 22.832×10^{-3}(counts/day)/(μBq/kg). Considering the error on this number minor than the error in the rate, it is possible to obtain for the activity

$$A = \frac{59.9 \text{ counts}/(\text{kg} \cdot \text{yr}) \cdot 6.962 \text{ kg} \cdot \text{yr}}{22.832 \times 10^{-3} \frac{\text{counts/day}}{\mu\text{Bq/kg}} \cdot 167.129 \text{ days}} = 105.0^{+5.6}_{-5.4} \frac{\mu\text{Bq}}{\text{kg}}$$

The official result is at the limit of compatibility

$$A = 92.8^{+5.3}_{-5.1} \frac{\mu\text{Bq}}{\text{kg}}.$$

In any case, the key point is that our estimates are at least two times above an upper limit in literature: 41 μBq/kg (90% C.L) [5].

```
Detector | Efficiency (counts/day)/(uBq/kg)
    ANG2 |       (4.538 +- 0.061) x 10^(-3)
    ANG3 |       (3.735 +- 0.054) x 10^(-3)
    ANG4 |       (3.936 +- 0.057) x 10^(-3)
    ANG5 |       (4.083 +- 0.052) x 10^(-3)
     RG1 |       (3.129 +- 0.050) x 10^(-3)
     RG2 |       (3.411 +- 0.052) x 10^(-3)
```

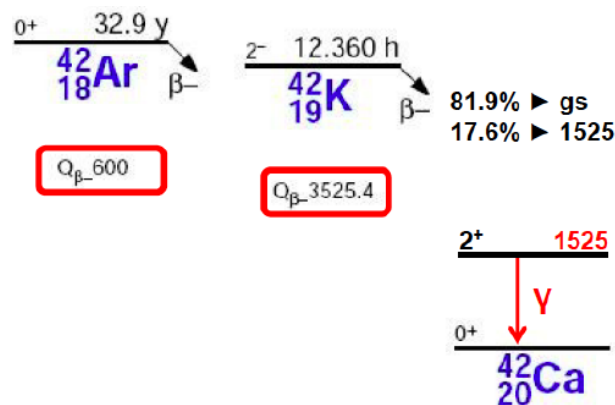Table 11.2: Detector efficiencies for ^{42}Ar decay.

Figure 11.4: ^{42}Ar decay scheme.

11.4 Conclusions

I have developed an algorithm to search for peaks in the energy spectrum in an automatic way. Result are consistent with the official ones.

The background in GERDA is lower than the background observed in the Heidelberg-Moscow experiment.

A very high rate of ^{42}K decays is observed. Their signature is a photon emitted at 1524.7 keV. ^{42}K originates from ^{42}Ar, and, to explain the line rate, it is required an ^{42}Ar activity in natural Argon more than two times above a 90% upper limit in literature [5].

Bibliography

[1] J.O. Ramsay, *Monotone Regression Splines in Action*, Statistical Science 3 (4): 425–441 (1998).

[2] Kenneth P. Burnham and David R. Anderson, *Model selection and multimodel inference*: *A pratical information - Theoretic approach*, 2002.

[3] O. Chkvorets, *PhD thesis, U. Heidelberg* (2008).

[4] O.A. Ponkratenko, V.I. Tretyak, and Yu.G. Zdesenko, *The Event generator DECAY4 for simulation of double beta processes and decay of radioactive nuclei*, Phys.Atom.Nucl. **63** (2000), 1282-1287, available at `arXiv:nucl-ex/0104018`.

[5] V.D. Ashitkov, A.S. Barabash, S.G. Belogurov, G. Carugno, S.I. Konovalov, et al., *Liquid argon ionization detector for double beta decay studies* (2003), available at `arXiv:nucl-ex/0309001`.

Chapter 12

Measurement of the half-life of the $2\nu\beta\beta$ decay

Introduction

Probably, the most important result obtained by the GERDA experiment up to now, is a new estimate of the half-life for the two-neutrino $\beta\beta$ decay ($2\nu\beta\beta$) of ^{76}Ge [1]

$$^{76}\text{Ge} \rightarrow \ ^{76}\text{Se} + 2e^- + 2\overline{\nu}_e.$$
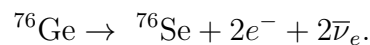
The $2\nu\beta\beta$ contribution is clearly visible in the sum energy spectrum of the enriched detectors, as shown in Fig. 12.1.

In this chapter I will describe my approach to the estimation of the half-life of the decay, which I have developed in a parallel way with the official one, to have a fundamental cross-check of the analysis. At the end of the chapter I will move to the official result, to discuss the systematics and to compare it with the previous experimental values.

12.1 The data set

My data set is made of GERDA runs 25-34, except Run 31 and Run 33 which were quite unstable. I have considered the most stable enriched detectors: ANG2, ANG3, ANG4, ANG5, RG1, RG2. Their exposures, degree of enrichment and active mass fraction are summarized in Tab. 12.1. The livetime is 167.129 days; the total exposure is 6.6922 kg·yr (my dataset is a bit wider compared to the 6.10 kg yr of the official analysis (Fig. 12.1)).
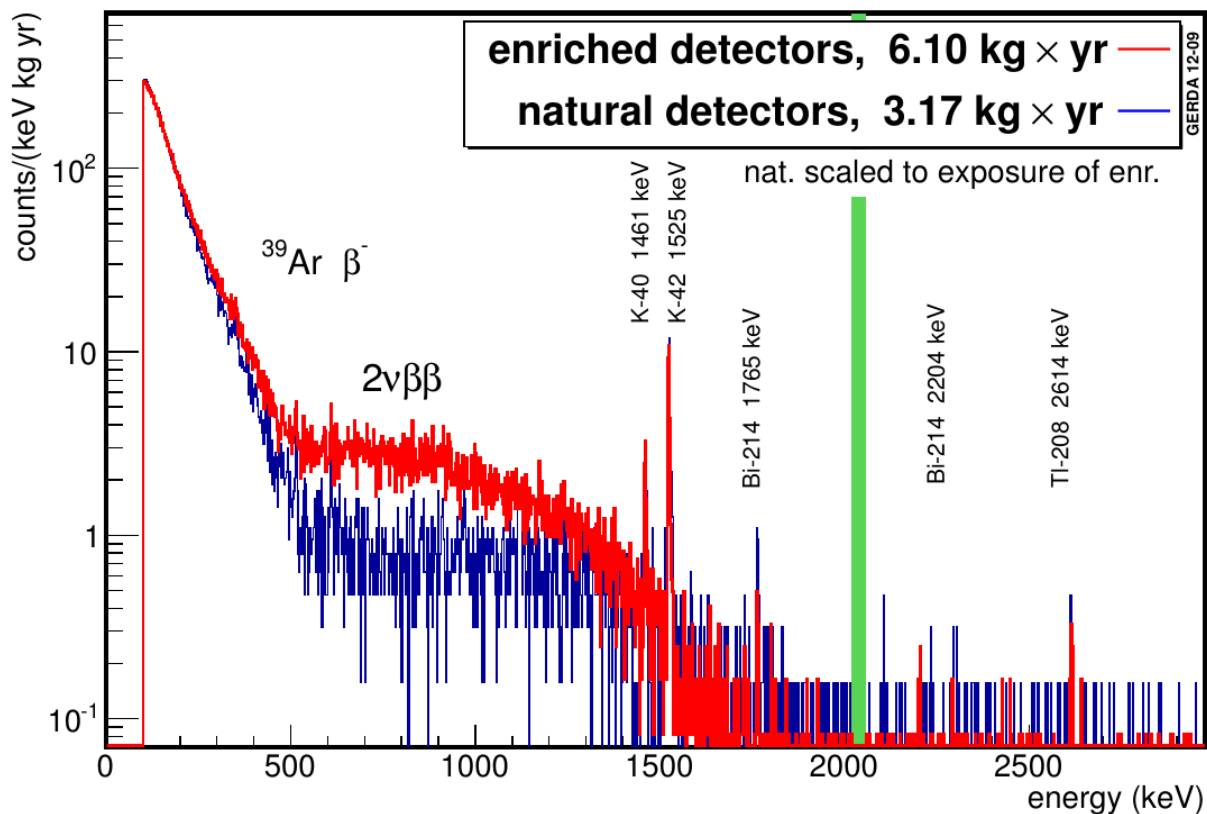
Figure 12.1: Comparison between the sum energy spectrum of natural and enriched detectors. The different weight of the $2\nu\beta\beta$ contribution is evident. This is an official GERDA plot. It refers to an exposure of 6.10 kg yr.

```
Detector | Exposure | Enrichment       | Active mass fraction
         |    kg yr |                  |
    ANG2 |   1.2963 | 0.866 +- 0.025   | 0.871 +- 0.042
    ANG3 |   1.0940 | 0.883 +- 0.026   | 0.866 +- 0.056
    ANG4 |   1.0867 | 0.863 +- 0.013   | 0.899 +- 0.049
    ANG5 |   1.2564 | 0.856 +- 0.013   | 0.831 +- 0.039
     RG1 |   0.9668 | 0.855 +- 0.001   | 0.876 +- 0.050
     RG2 |   0.9920 | 0.855 +- 0.001   | 0.865 +- 0.047
```

Table 12.1: Detectors summary table: the columns are: detector, exposure (kg·yr), degree of enrichment (values from [2]), active mass fraction (values from [3]).

12.2 The model

The idea is to obtain a decomposition of the energy spectrum for each detector. In my model, I have considered four components:

- $2\nu\beta\beta$

- ^{42}K (decays in liquid argon)

- ^{214}Bi (decays in the holders)

- ^{40}K (decays in the holders).

The $2\nu\beta\beta$ is the component of interest, and ^{42}K, ^{214}Bi and ^{40}K are evident in the energy spectra, because of the lines at 1525 keV, 1764 keV and 1460 keV.
^{214}Bi and ^{40}K have been considered "close sources" (near the detectors). The ratio of intensities of ^{214}Bi γ lines is consistent with this hypothesis.
For sure, other components provide minor contributions. The effect of the missing components is treated as a systematic error. I will discuss systematics in the following.
The energy spectrum of each component for each detector has been obtained from Monte Carlo simulations. Thus, we need to fit the simulated spectra to the data.

12.3 The fit configuration

My fit region is the energy range 600-1800 keV, as shown in Fig. 12.2. Namely, it is above the ^{39}Ar region and wide enough to include the ^{214}Bi line at 1764 keV, to better constrain the fit for this component. My approach is a maximum likelihood binned fit, the bin size is 30 keV.
My fits parameters for the ^{42}K, ^{214}Bi, ^{40}K components are the total number of counts expected in the fit region. One parameter is used for each component for each detector.
Considering the $2\nu\beta\beta$ component, the number of expected $2\nu\beta\beta$ counts in the fit energy region, for each detector, is given by (3.2)

$$N_{exp,2\nu\beta\beta,\text{det}} = \eta \frac{N_A}{A}(aMt)\frac{\ln[2]}{T_{1/2}^{2\nu\beta\beta}} f_{2\nu\beta\beta,\text{det}}$$

where $f_{2\nu\beta\beta,\text{det}}$ is the fraction of events in the fit energy region to the total number of $2\nu\beta\beta$ events in the full energy spectrum.
To describe this component, I have chosen the product of the degree of enrichment and the active mass fraction $a \cdot \eta$ for each detector, and the global parameter $T_{1/2}^{2\nu\beta\beta}$.
I have also chosen a flat priors for all the parameters, except for $\{(a \cdot \eta)_{\text{det}}\}$, for which I have provided gaussian priors using the values in Tab. 12.1.
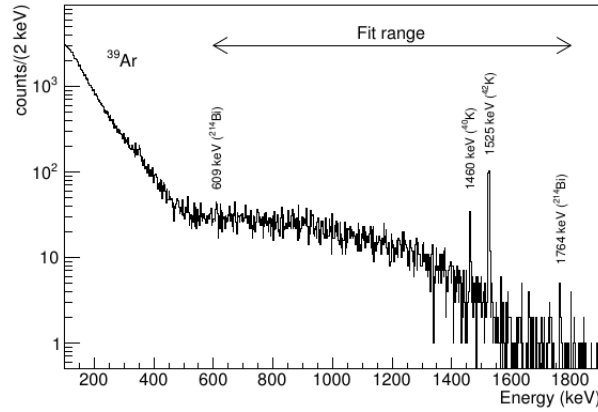
Figure 12.2: The fit region.

Thus, the total number of fit parameters is $6 \cdot 4 + 1 = 25$: 24 nuisance parameters and $T_{1/2}^{2\nu\beta\beta}$.

12.4   Bayesian approach

To lighten the notation we can define

$$e_{dbc} \equiv \text{expected counts[detector, bin, component]}$$

$$e_{db} \equiv \text{expected counts[detector, bin]} = \sum_c e_{dbc} \qquad o_{db} \equiv \text{observed counts[detector, bin]}.$$

From the Bayes theorem it is possible to write

$$\text{pr}[T_{1/2}^{2\nu\beta\beta}, \vec{v}] = \frac{\text{pr}[\vec{o_{db}}|T_{1/2}^{2\nu\beta\beta}, \vec{v}]\text{pr}[T_{1/2}^{2\nu\beta\beta}, \vec{v}]}{\text{pr}[\vec{o_{db}}]} \propto \text{pr}[\vec{o_{db}}||T_{1/2}^{2\nu\beta\beta}, \vec{v}]\text{pr}[T_{1/2}^{2\nu\beta\beta}, \vec{v}]$$

where pr refers to a probability density, $\vec{o_{db}}$ represents the data and $\vec{v}$ is the vector of the 24 nuisance fit parameters. $\text{pr}[\vec{o_{db}}|T_{1/2}^{2\nu\beta\beta}, \vec{v}]$ is the likelihood

$$\text{pr}[\vec{o_{db}}|T_{1/2}^{2\nu\beta\beta}, \vec{v}] = \prod_{\text{det}} \prod_{\text{bin}} \frac{\exp[e_{db}]e_{db}^{o_{db}}}{o_{db}!}$$

and $\text{pr}[T_{1/2}^{2\nu\beta\beta}, \vec{v}]$ is the global prior, which is the product of a gaussian prior for $a\eta$ for each detector. $\text{pr}[T_{1/2}^{2\nu\beta\beta}, \vec{v}]$ is the posterior probability, and a simple $T_{1/2}^{2\nu\beta\beta}$ estimate can be obtained by maximizing it. It is the maximum a posteriori (MAP) approach.

12.5 Maximum a posteriori results

The MAP results are summarized in Tab. 12.2. The decomposition of the sum energy spectrum is shown in Fig. 12.3. The obtained half-life is

$$T_{1/2}^{2\nu\beta\beta} = (1.866 \pm 0.073) \times 10^{21} \text{ yr.}$$

```
Detector | Counts |   2nuBB     42K     214BI     40K |   Total
    ANG2 |   2197 | 1766.41  337.14    64.44   39.43 | 2207.43
    ANG3 |   2055 | 1655.76  261.04   120.75    5.15 | 2042.70
    ANG4 |   1872 | 1565.60  213.88    60.77   33.94 | 1874.19
    ANG5 |   2250 | 1704.53  325.79   137.25   74.15 | 2241.72
     RG1 |   1760 | 1356.83  302.26    67.23   33.00 | 1759.31
     RG2 |   1715 | 1335.77  287.46    55.48   44.94 | 1723.65
```

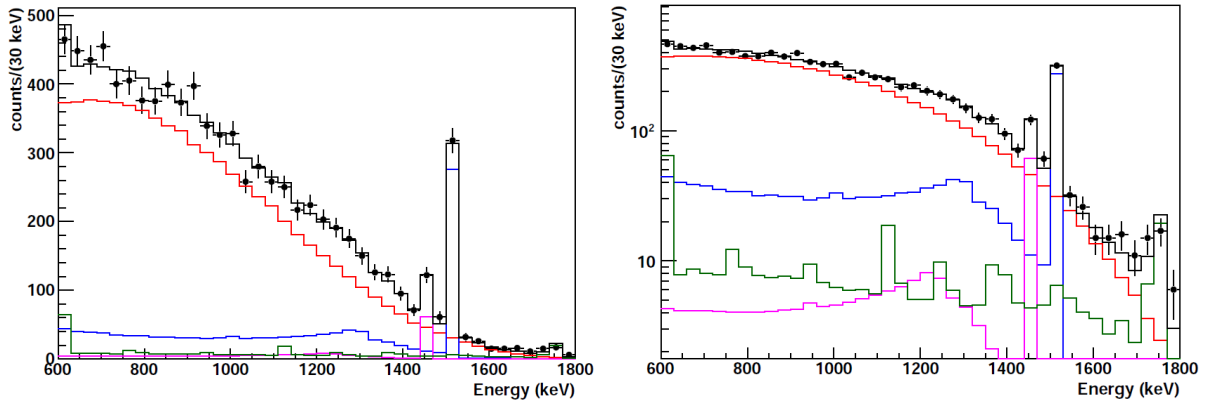Table 12.2: Maximum a posteriori results. The p-value of the fit is 0.415.

Figure 12.3: Experimental data (markers) superimposed with the best-fit model (black histogram). Individual contributions from $2\nu\beta\beta$ (red), ^{42}K (blue), ^{214}Bi (green) and ^{40}K (purple) are shown separately. Linear and log scale are shown.

12.6 Marginalization

To obtain a more precise estimate of $T_{1/2}^{2\nu\beta\beta}$ it is necessary to integrate the posterior over all the nuisance parameters.

$$\text{pr}[T_{1/2}^{2\nu\beta\beta}] = \int \text{pr}[T_{1/2}^{2\nu\beta\beta}, \vec{v}]d\vec{v}.$$

In the official analysis, this integral is evaluated by using a Markov Chain Monte Carlo (MCMC) approach, in particular a random walk Metropolis algorithm which is part of

the BAT toolkit [4]. MCMC approaches are very useful, but it is important to cross-check their results, because, for example, their convergence could be slow.

I tried to choose something different. Common numerical approaches fail because the number of parameters is too high.

Thus, I decided to solve the integral by using the Laplace approximation: the idea is to approximate the posterior distribution with a Multivariate Gaussian around its maximum. Given T_1 and T_2 (possible values for $T_{1/2}^{2\nu\beta\beta}$), defining

$$f \equiv -\log[\mathrm{pr}[T, \vec{v}]] \qquad \vec{v}_1 \equiv \min f[T_1, \vec{v}] \qquad \vec{v}_2 \equiv \min f[T_2, \vec{v}]$$

it is possible to write

$$\frac{\mathrm{pr}[T_1]}{\mathrm{pr}[T_2]} = \frac{\int \exp\left[-f[T_1, \vec{v}]\right] d\vec{v}}{\int \exp\left[-f[T_2, \vec{v}]\right] d\vec{v}} \simeq \frac{\exp\left[-f[T_1, \vec{v}_1]\right] \int \exp\left[-\frac{1}{2}(\vec{v} - \vec{v}_1)^T H[\vec{v}_1](\vec{v} - \vec{v}_1)\right] d\vec{v}}{\exp\left[-f[T_2, \vec{v}_2]\right] \int \exp\left[-\frac{1}{2}(\vec{v} - \vec{v}_2)^T H[\vec{v}_2](\vec{v} - \vec{v}_2)\right] d\vec{v}}$$

$$= \frac{\mathrm{pr}[T_1, \vec{v}_1](2\pi)^{n/2}|H[\vec{v}_1]|^{-1/2}}{\mathrm{pr}[T_2, \vec{v}_2](2\pi)^{n/2}|H[\vec{v}_2]|^{-1/2}} = \frac{\mathrm{pr}[T_1, \vec{v}_1]|H[\vec{v}_2]|^{1/2}}{\mathrm{pr}[T_2, \vec{v}_2]|H[\vec{v}_1]|^{1/2}}$$

where H is the Hessian Matrix of f respect to the parameters $\vec{v}$ and n is the number of nuisance parameters.

In this way it is possible to analyze a set of values $T_1...T_n$, and then construct the probability distribution which is presented in Fig. 12.4.

My final result is

$$T_{1/2}^{2\nu\beta\beta} = (1.881^{+0.053}_{-0.052}) \times 10^{21} \text{ yr.} \tag{12.1}$$

Using the official GERDA code and a similar fit configuration (using the parameters in Tab. 12.1), the obtained result is

$$T_{1/2}^{2\nu\beta\beta} = (1.877^{+0.057}_{-0.050}) \times 10^{21} \text{ yr}$$

so my result and the MCMC integration validate each other.

12.7   Single detector test

A final check: I have tried a separate fit for each detector. One detector at time. One $T_{1/2}^{2\nu\beta\beta}$ estimate for each detector. The results are presented in Tab. 12.3. Single-detector estimates are mutually compatible, and are also compatible with the global estimate (12.1).
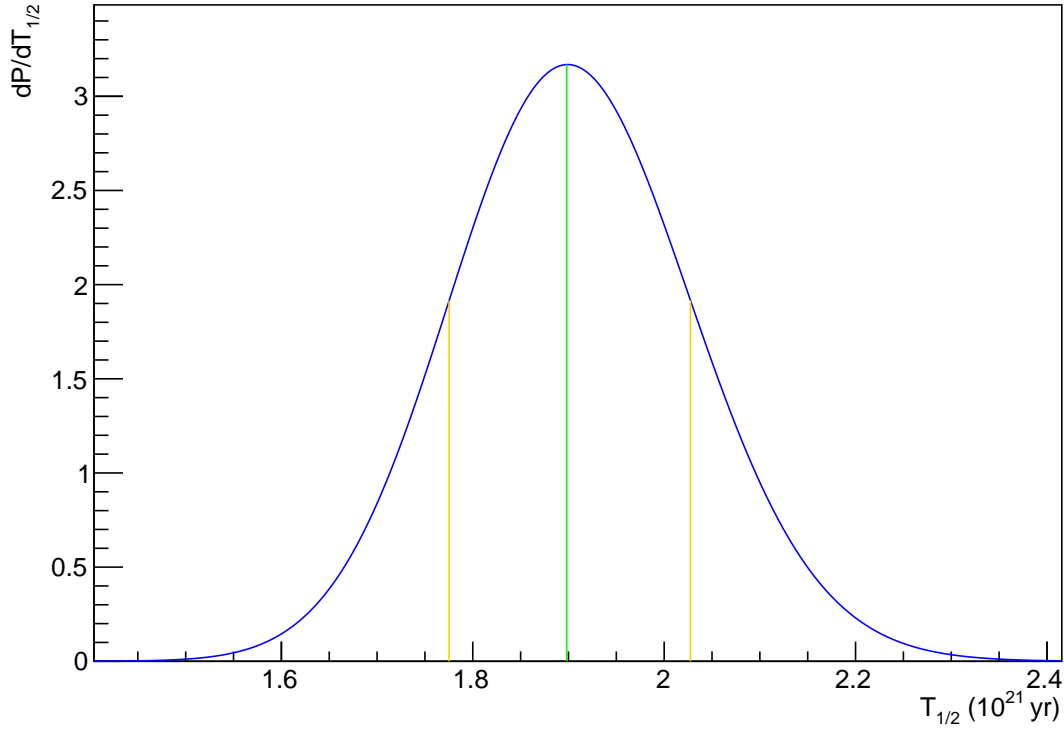
Figure 12.4: $T_{1/2}^{2\nu\beta\beta}$ - Final probability distribution. In green: the mode. The yellow lines are the boundaries of the 68% minimal band.

```
ANG2 |  1.955 +- 0.182  |  0.858  |  1.970 - 0.127 + 0.133
ANG3 |  1.736 +- 0.194  |  0.708  |  1.751 - 0.135 + 0.142
ANG4 |  1.884 +- 0.176  |  0.209  |  1.898 - 0.123 + 0.129
ANG5 |  1.810 +- 0.156  |  0.417  |  1.821 - 0.109 + 0.114
 RG1 |  1.860 +- 0.183  |  0.170  |  1.877 - 0.130 + 0.134
 RG2 |  1.944 +- 0.188  |  0.468  |  1.961 - 0.131 + 0.140
```

Table 12.3: Single detector fits: the columns are detector, MAP estimate, p-value of the MAP estimate and marginalization result ($T_{1/2}^{2\nu\beta\beta}$ estimates are written in units of 10^{21} yr).

12.8 GERDA official results

The present GERDA official result is

$$T_{1/2}^{2\nu\beta\beta} = (1.84^{+0.09}_{-0.08}\text{ fit }{}^{+0.11}_{-0.06}\text{ syst}) \times 10^{21} \text{ yr.}$$

The fit configuration in the GERDA official analysis is nearly the same of my approach. The marginalization is done by MCMC integration. The key difference is due to new

Missing components in the background model	+5.3%	
Energy spectra from ^{42}K, ^{40}K and ^{214}Bi	2.1%	
Shape of the $2\nu\beta\beta$ decay spectrum	1.0%	
Subtotal fit model		$+5.8\%$ -2.3%
Precision of the Monte Carlo geometry model	1%	
Accuracy of the Monte Carlo tracking	2%	
Subtotal Monte Carlo		2.2%
Data acquisition and selection		0.5%
Grand Total		$+6.2\%$ -3.3%

Table 12.4: Summary table of the systematic uncertainties on $T_{1/2}^{2\nu\beta\beta}$ which are taken into account for this work and which are not included in the fitting procedure.

estimates for the active mass fraction of the detectors. In these estimates, the error is splitted between the random and systematic components, and the code has been improved to implement this.

The systematic uncertainties are described in Tab. 12.4. The most important is due to the additional background components which are not accounted in the fit model. Due to the limited exposure these background components cannot be identified unambiguously. The uncertainty arising from such possible contributions is estimated to be 5.3%. Since any further background component would lead to a longer $T_{1/2}^{2\nu\beta\beta}$, this uncertainty is asymmetric. It has been estimated by performing a fit with the contributions from ^{60}Co, ^{228}Ac and a flat background added to the model.

In Fig. 12.5, the official result is compared with the estimates from previous experiments.

12.9   Conclusions

I have developed a procedure to estimate the $2\nu\beta\beta$ half-life of ^{76}Ge. The result is

$$T_{1/2}^{2\nu\beta\beta} = (1.881_{-0.052\ \text{fit}}^{+0.053}\ _{-0.06\ \text{syst}}^{+0.11}) \times 10^{21}\ \text{yr}.$$

The present GERDA official result is

$$T_{1/2}^{2\nu\beta\beta} = (1.84_{-0.08\ \text{fit}}^{+0.09}\ _{-0.06\ \text{syst}}^{+0.11}) \times 10^{21}\ \text{yr}.$$

The official analysis features a more advanced approach to the uncertainties in the active mass of the detectors.
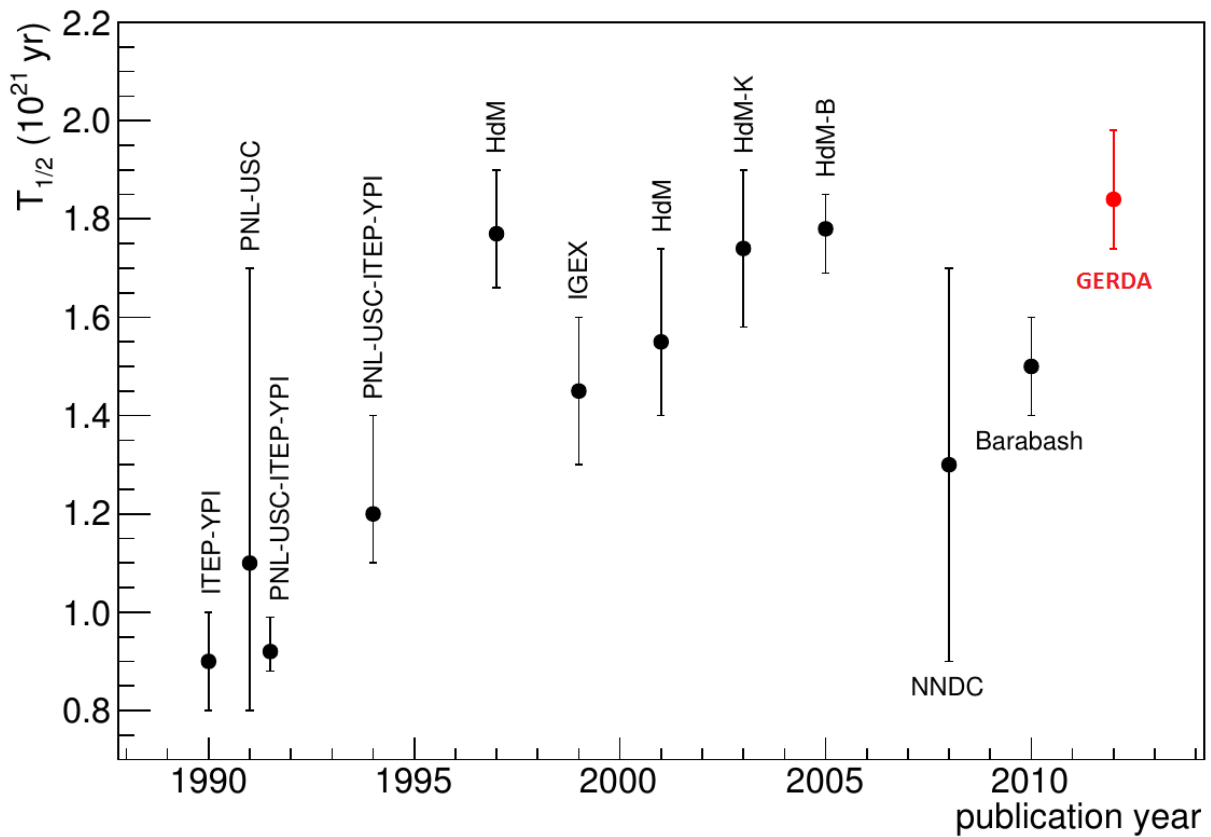
GERDA and Heidelberg-Moscow results are compatible.

Figure 12.5: Experimental results for $T_{1/2}^{2\nu\beta\beta}$ of ^{76}Ge vs. publication year. The plot includes results from the experiments ITEP-YPI [5], PNL-USC [6], PNL-USC-ITEP-YPI [7] [8], Heidelberg-Moscow (HdM) [9] [10] and IGEX [11], as well as the re-analysis of the HdM data by Klapdor-Kleingrothaus et al. [12] (HdM-K) and by Bakalyarow et al. [13] (HdM-B). The NNDC-recommended value [14] and the global weighted average evaluated by Barabash [15] are also shown.

Bibliography

[1] M. Agostini et al., *Measurement of the half-life of the two-neutrino double beta decay of Ge-76 with the Gerda experiment*, in press on J.Phys.G (2012), available at `arXiv:1212.3210[nucl-ex]`.

[2] P. Grabmayr, *Abundances of Germanium in Gerda and Neutron capture rates on detector with different isotopic composition*, GERDA Internal Note GSTR-11-008 (2011).

[3] M. Barnabé Heider, *Performance and stability tests of bare high purity germaniu detectors in liquid argon for the GERDA experiment*, PhD thesis, U. Heidelberg (2009).

[4] Allen Caldwell, Daniel Kollar, and Kevin Kroninger, *BAT: The Bayesian Analysis Toolkit*, Comput.Phys.Commun. **180** (2009), 2197-2209, available at `arXiv:0808.2552[physics.data-an]`.

[5] A.A. Vasenko, I.V. Kirpichnikov, V.A. Kuznetsov, A.S. Starostin, A.G. Dzhanian, et al., *New results in the ITEP / YEPI Double Beta Decay Experiment with enriched Germanium detector*, Mod.Phys.Lett. **A5** (1990), 1299-1306.

[6] H.S. Miley, R.L. Brodzinski, J.H. Reeves, F.T. Avignone, and J.I. Collar, *Suggestive evidence for the two neutrino double beta decay of Ge-76*, Phys.Rev.Lett. **65** (1990), 3092-309.

[7] F.T. Avignone, C.K. Guerard, R.L. Brodzinski, H.S. Miley, J.H. Reeves, et al., *Confirmation of the observation of 2 neutrino beta-beta decay of Ge-76*, Phys.Lett. **B256** (1991), 559-561.

[8] F.T. Avignone, *Double-beta decay: Some recent results and developments*, Prog.Part.Nucl.Phys. **32** (1994), 223-245.

[9] M. Gunther, J. Hellmig, G. Heusser, M. Hirsch, H.V. Klapdor-Kleingrothaus, et al., *Heidelberg - Moscow beta-beta experiment with Ge-76: Full setup with five detectors*, Phys.Rev. **D55** (1997), 54-67.

[10] H.V. Klapdor-Kleingrothaus, A. Dietz, L. Baudis, G. Heusser, I.V. Krivosheina, et al., *Latest results from the Heidelberg-Moscow double beta decay experiment*, Eur.Phys.J. **A12** (2001), 147-154, available at `arXiv:hep-ph/0103062`.

[11] C.E. Aalseth et al., *Neutrinoless double-beta decay of Ge-76: First results from the International Germanium Experiment (IGEX) with six isotopically enriched detectors*, Phys.Rev. **C59** (1999), 2108-2113.

[12] C. Dorr and H.V. Klapdor-Kleingrothaus, *New Monte-Carlo simulation of the Heidelberg-Moscow double beta decay experiment*, Nucl.Instrum.Meth. **A513** (2003), 596-621.

[13] A.M. Bakalyarov, A. Ya. Balysh, S.T. Belyaev, V.I. Lebedev, and S.V. Zhukov, *Results of the experiment on investigation of Germanium-76 double beta decay: Experimental data of Heidelberg-Moscow collaboration November 1995 - August 2001*, Phys.Part.Nucl.Lett. **2** (2005), 77-81, available at `arXiv:hep-ex/0309016`.

[14] B. Pritychenko, Nuclear Structure 2008, June 3-6 2008, East Lansing, MI, `http://www.hhdc.nbl.gov/bbdecay/`.

[15] A.S. Barabash, *Precise half-life values for two neutrino double beta decay*, Phys.Rev. **C81** (2010), 035501, available at `arXiv:1003.1005[nucl-ex]`.

Conclusions

In this thesis I have described my work in the GERDA Collaboration during my Ph.D. The GERDA experiment is searching for the Neutrinoless Double Beta Decay of ^{76}Ge [1] [2]. The most important features of the experiment have been presented in chapter 4. The data taking is ongoing. I cannot provide the first $0\nu\beta\beta$ results in this work, because presently we are not looking at the events around $Q_{\beta\beta}$. A small energy window is blinded: events are stored but not analyzed by the Collaboration. The idea is to provide a background model before the opening of the window. As I have explained in chapter 9, according to the duty cycle, an exposure of 20 kg·yr, which is the Phase I goal, is expected to be reached in spring 2013.

I have divided the description of my work in GERDA in many chapters.

• In chapter 5 I have presented GELATIO [3] [4], [5], the Digital Signal Processing software which has been developed for the experiment. It is able to extract the condensed parameters (e.g. energy and risetime) which describe the digitized signals. GELATIO is able to manage different input sources (e.g. Germanium data, Monte Carlo simulations, photomultipliers of the muon veto), because its modular approach is very versatile. GELATIO features a complex Graphical User Interface, designed by using the ROOT toolkit, which I have developed to provide an easy way to configure all the parameters of the modules.

• In chapter 6 I have described an original procedure to obtain parametrizations of the impulse response function of the electronic chain from the calibration data. Different models of the response function are supported. It is clear that an improved model for the response function is fundamental to obtain a perfect reconstruction of the input of the electronic chain, which is the current induced by the physical signals in the detectors. The fact that my analysis relies on the calibration data make it also interesting for monitoring purposes, because a calibration is a standard GERDA procedure which is done once per week. I have tested my approach to four different calibrations, and results are very consistent.

- In chapter 7 I have applied my best model of the impulse response function to the energy reconstruction and to the current reconstruction of the acquired signal. I have tested my procedure to three recent calibrations. About the energy reconstruction, I have obtained a similar quality of the official one. About the current reconstruction, it is one of the most advanced available in GERDA at the moment. I have also started a study of a parameter which could be interesting for the pulse shape discrimination: Q_{40}/Q, which is the maximum charge induced in the feedback capacitor of the preamplifier in a period of 40 ns compared to the total charge. The distribution of this parameter at the Double Escape Peak of the 2614 keV ^{208}Tl line in BEGe detectors is characterized by a ratio between the standard deviation and the mean value of about 1.3%. This resolution is enough to mark as multi-site all the three events observed in the window $Q_{\beta\beta} \pm 200$ keV in Bege detectors in the examined period.

- In chapter 8 I have presented the database application which I have developed for the data management of the experiment [6]. It is able to generate a wide set of reports, which are very useful for the off-line data quality monitoring. The off-line monitoring provided a measure of the quality acquisition (e.g. noise levels, leakage current and rate monitoring) and it is complementary to the slow control system, to ensure that everything is running in the proper way.

- In chapter 10 I have described an approach to estimate the efficiency of the muon veto. The muon veto efficiency has been estimated in

$$\varepsilon > 0.99 \qquad 95\% \text{ lower limit.}$$

It is important to estimate the muon veto efficiency to obtain an estimate of muon-induced single-detector background due to non-identified events with an energy release around $Q_{\beta\beta}$. My final result is

$$B_\mu < 2.8 \times 10^{-5} \, \frac{\text{counts}}{\text{keV kg yr}} \qquad 95\% \text{ upper limit.}$$

The Phase I background goal is $10^{-2} \frac{\text{counts}}{\text{keV kg yr}}$ and the Phase II background goal is $10^{-3} \frac{\text{counts}}{\text{keV kg yr}}$, so the muon veto is able to satisfate the GERDA needs.

- In chapter 11 I have presented an original algorithm which I have developed to search for gamma ray peaks in the energy spectrum without any other input. It is a full blind approach. The key idea is to model the background using a positive-definite continuous function (a positive definite spline), which is characterized by a wider scale (the distance between the knots) compared to the typical peak scale (a few keV). The scale can be automatically estimated minimizing the AIC model index. Small structures are not well

fitted, so it is easy to scan the spectrum for them. The advantages of this approach are non-biased results, which are useful for example to detect calibration problems (a the peak center different than real value) or to search for unexpected lines. I have compared my result with the official ones, and they are fully compatible. The gamma background in GERDA is really lower than the one of Heidelberg-Moscow. From the rate of the 1524.7 keV line of the ^{42}K decay, I have provided an estimate of the ^{42}Ar activity in natural argon

$$A = 105.0^{+5.6}_{-5.4} \; \frac{\mu \mathrm{Bq}}{\mathrm{kg}}.$$

The result is an activity two times above a 90% upper limit provided by V.D. Ashitkov

$$A < 41 \; \frac{\mu \mathrm{Bq}}{\mathrm{kg}}$$

(arXiv:nucl-ex/0309001).

- In chapter 12, the last one, I have described my procedure for the measurement of the half-live of the $2\nu\beta\beta$ decay of ^{76}Ge [7]. My bayesian analysis is characterized by a different approach to the posterior marginalization compared to the GERDA official one. I have used a gaussian approximation at the point of maximum of the posterior, while the official analysis relies on a Markov Chain Monte Carlo approach. Having different procedures is clearly fundamental for a cross-check of the results. My final result is

$$T^{2\nu\beta\beta}_{1/2} = (1.881^{+0.053}_{-0.052} \; {}^{+0.11}_{-0.06 \; \mathrm{syst}}) \times 10^{21} \; \mathrm{yr.}$$

Recently, new estimates of the active masses of the detectors have been done, so the official GERDA result is a little different

$$T^{2\nu\beta\beta}_{1/2} = (1.84^{+0.09}_{-0.08 \; \mathrm{fit}} \; {}^{+0.11}_{-0.06 \; \mathrm{syst}}) \times 10^{21} \; \mathrm{yr.}$$

The GERDA and Heidelberg-Moscow results are fully compatible.

Publication list

[1] K. H. Ackermann et al., *The GERDA experiment for the search of* $0\nu\beta\beta$ *decay in* ^{76}Ge (2012), available at `arXiv:1212.4067[physics.ins-det]`.

[2] P. Zavarise, *The GERDA experiment: status and future plan*, Acta Polytechnica Vol. 53 N. 1 (2013), Vulcano Workshop 2012.

[3] M. Agostini, L. Pandola, P. Zavarise, and O. Volynets, *GELATIO: A General framework for modular digital analysis of high-purity Ge detector signals*, JINST **6** (2011), P08013, available at `arXiv:1106.1780[physics.data-an]`.

[4] M. Agostini, J.A. Detwiler, P. Finnerty, K. Kroninger, D. Lenz, et al., *The MGDO software library for data analysis in Ge neutrinoless double-beta decay experiments*, J.Phys.Conf.Ser. **375** (2012), 042027, available at `arXiv:1111.7260[physics.data-an]`.

[5] M. Agostini, L. Pandola, and P. Zavarise, *Off-line data processing and analysis for the GERDA experiment*, J.Phys.Conf.Ser. **368** (2012), 012047, available at `arXiv:1111.3582[physics.data-an]`.

[6] P. Zavarise, M. Agostini, A.A. Machado, L. Pandola, and O. Volynets, *Off-line data quality monitoring for the GERDA experiment*, J.Phys.Conf.Ser. **375** (2012), 042028, available at `arXiv:1111.7200[physics.data-an]`.

[7] M. Agostini et al., *Measurement of the half-life of the two-neutrino double beta decay of Ge-76 with the Gerda experiment*, in press on J.Phys.G (2012), available at `arXiv:1212.3210[nucl-ex]`.